SINGLE MOLECULE INTERACTION AND CONFORMATION STUDY BASED ON ATOMIC FORCE MICROSCOPY

by

GUOJUN CHEN

(Under the Direction of Bingqian Xu)

ABSTRACT

Single molecule study, where science and engineering met, applies the tools and measurement techniques of nanoscale physics and chemistry to generate remarkable new insights into how physical, chemical, and biological systems function. Among these single molecule manipulation techniques widely applied, optical tweezers (OT), magnetic tweezers (MT) and atomic force microscopy (AFM), AFM provides both ultrahigh resolution imaging and dynamic force measurements. In this study, we developed and used a comprehensive AFM-based technology to study single molecule recognitions, interactions and biomolecular processes in real time under near natural conditions.

For single molecule recognitions and interactions studies, we first immobilized the targets on modified Au(1,1,1) surface via gold-thiol affinities and functionalized magnetically coated AFM tips with molecules specific to the targets, hanging at the end of heterofunctional polyethylene glycol (PEG) string. Then both AFM single molecule recognition imaging based on TopMAC mode and dynamic force spectroscopy (DFS) measurements were performed for the molecule interaction systems of ricin and its antibody, EphA2 and its peptide ligands, and specially designed dibenzocyclooctyne and azide on micelle surface by “click” reactions. This

way, single molecular interactions and reactions were visualized with a spatial resolution of about 1nm. In addition, the pN force resolution DFS measurements revealed the kinetics and dynamics of the interactions by fitting the experimental data with theoretical Bell model and Jarzynski equality, which were used to translate the results in physical force unit, pN, into kinetic and equilibrium parameters, such as dissociation rate constant (k_{off}), association rate constant (k_{on}), dissociation constant (K_D), and the unbinding free energy.

For real-time imaging of biomolecular processes under near natural conditions, we visualized the conformation differences of fibrinogen (fg) on various surfaces, e.g., mica, HOPG and gold surface. It was found that fg can self-assembly on gold surface in longitude and transverse direction without any addition of clotting factors, such as thrombin, which is essentially distinct with fg adsorption on mica and HOPG. In addition, fg clot can be induced by gold nanoparticle (GNP). The underlying mechanisms were proposed as the disulfide bridges in the E domain and flank parts at C-terminal and N-terminal, and extra stabilizers including 'αC-domain' 'D:D' and 'γ_{XL}' intermolecular interactions.

This study enables direct observation of molecular behavior that can be obscured by ensemble averaging and the study of important problems ranging from the fundamental biophysics of single molecule interactions, such as the energy landscape of biomolecular reactions, associated lifetimes, and free energy, to the study and design of high‐affinity, anti‐cancer drugs.

INDEX WORDS: Scanning probe microscope (SPM), Atomic force microscope (AFM), Single molecule force spectroscopy (SMFS), Topographical and recognition image (TREC), Self-assembly monolayer (SAM), Organo-silicon, Polyethylene glycol (PEG), Organosulfur, Ricin, Organomicell, EphA, Ephrin, Fibrinogen, Gold nanoparticle, Bell's model, Jarzynski equality.

SINGLE MOLECULE INTERACTION AND CONFORMATION STUDY BASED ON ATOMIC FORCE MICROSCOPY

by

GUOJUN CHEN

BE, Nanjing University of Technology, China, 2001

ME, Nanjing University of Technology, China, 2004

A Dissertation Submitted to the Graduate Faculty of The University of Georgia in Partial Fulfillment of the Requirements for the Degree

DOCTOR OF PHILOSOPHY

ATHENS, GEORGIA

2011

SINGLE MOLECULE INTERACTION AND CONFORMATION STUDY BASED ON ATOMIC FORCE MICROSCOPY

by

GUOJUN CHEN

Major Professor:	Bingqian Xu
Committee:	Geert-Jan Boons
	Jason Locklin
	Bosoon Park

Electronic Version Approved:

Maureen Grasso
Dean of the Graduate School
The University of Georgia
May 2011

DEDICATION

I dedicate this dissertation to my wonderful and happy family, particularly to my understanding and supportive wife, Nanting Ni, and to our precious daughter, Nicole Zhuonv Chen, who is the joy of our lives. I also thank my loving father, mother, younger sister and my terrific in-laws who have helped so much with baby-sitting and given me their fullest unconditional support.

ACKNOWLEDGEMENTS

The four year study in UGA is close to the end. Although this short period didn't get me be fully familiar with UGA campus yet, I met with lots of terrific people whose contributions make all my achievements possible. I owe my gratitude to all those people. Because of them my graduate experience has been one that I will cherish forever.

My deepest gratitude is to my advisor, Dr. Bingqian Xu, who not only offered me the opportunity and full support to my Ph.D study in UGA, but also gave me the freedom to explore my own interests. His everlasting encouragement, guidance and support enabled me to successfully complete my Ph.D study. In addition, his kind advices, care, friendship and help in personal life made me pass through much of the hard time.

My thanks also go to my fully supportive and knowledgeable committee members, Dr. Geert-Jan Boons, Dr. Jason Locklin, and Dr. Bosoon Park. I am grateful to Dr. Geert-Jan Boons, who kindly granted me the access to his lab to perform organic synthesis work and triggered my interests in finding out the beauty and power of 'click-chemistry'. I owe my gratitude to Dr. Jason Locklin, who not only provided lots of constructive suggestions in surface chemistry and polymer, but also offered me free solvent and chemicals multiple times. I sincerely appreciate Dr. Bosoon Park for his advices in our collaborative ricin detection project. I also benefited a great deal from many other Professors. First I would like to thank Dr. Zhengwei Pan and Dr. Leidong Mao for their wonderful classes. I would also like to acknowledge the generosity and help of Dr. Binghe Wang and Dr. Zheng Huang at Georgia State University in our collaborated researches, which expanded my knowledge in some new fields, such as boronic acid and DNA synthesis.

I can't thank many nice and brilliant folks more for their unselfish help and support. Firstly, I would like to express my appreciation to all of the Xu group members: Dr. Fan Chen and Dr. Jianfeng Zhou helped me tremendously in learning and understanding AFM operations. Dr. Fan Chen also helped in developing many wonderful computer control and data processing Labview programs. It was great working with the other lab members, Dr. Anna Jagielska, Dr. Cunlan Guo, Bin Wang, Mengmeng Zhang, Dr. Samantha Hawkins, Cong Feng, Laing Lu and Paimun Jared (PJ) Amini who were always available and ready to help whenever I need them. Secondly, without the precious suggestions in chemical synthesis and functionalization from Dr. Jun Guo, Dr. Xiuru Li and Dr. Xinghai Ning in CCRC, my research included in this thesis won't be possible. Further, I would like to extend my thanks to Dr. Jia sheng, Dr. Lina Wang, Dr. Xiaoling Yang, Dr. Satyabrata Samanta, Dr. Feng Liu, Dr. Zhanjun Gu, Xufan Li, Kaiyuan Li, Yenjun Chuang, Taotao Zhu, Kristen Fries, Nicholas Marshall, Gareth Sheppard and Sara Orski. With you around, the monotonous research life became joyful and unforgettable here at UGA.

Most importantly, none of this would have been possible without the unconditional love and support of my family. Although my father and mother are still working hard to make a living, they never ask something from me and always give me support and care, whatsoever. My warmest gratitude is reserved to my wife and daughter. Their support, encouragement, quiet patience and unwavering love keep me stay sane, overcome setbacks and stay focused on my graduate study through these difficult years and my daughter always be my motivation to advance! Their smiles cheer me up every day!

Finally, I would like to beg for your forgiveness if I forget to add you to my thank-you list. My deepest appreciations to you all!

TABLE OF CONTENTS

Page

ACKNOWLEDGEMENTS v

LIST OF TABLES x

LIST OF FIGURES xi

CHAPTER

1 INTRODUCTION AND LITERATURE REVIEW 1

1.1 Techniques for single molecule study 1

1.2 Evolution of AFM image capability 5

1.3 Dynamic force spectroscopy 13

1.4 Molecule attachment 23

1.5 Objectives and organization of this thesis 27

2 SURFACE FUNCTIONALIZATION 30

2.1 Introduction 30

2.2 Instruments and Materials 30

2.3 Gold surface 32

2.4 Silicon related surface 40

2.5 Conclusions 47

3 RICIN DETECTION AND INTERACTION STUDY 48

3.1 Abstract 49

3.1 Introduction and literature review 49

3.2 Experiments 51

3.3 Results and discussions 54

3.4 Conclusions 61

4 SINGLE MOLEULE INTERACTION STUDY BETWEEN CANCER TARGET EphA2 AND ITS LIGANDS 63

4.1 Introduction 63

4.2 Experiments 64

4.3 Results and discussions 76

4.4 Conclusions 84

5 VISUALIZING SURFACE FUNCTIONAL GROUPS OF MULTIFUNCTIONAL MACROMOLECULAR ASSEMBLIES 87

5.1 Introduction 87

5.2 Experiments 88

5.3 Results and discussions 91

5.4 Conclusions 100

6 FIBRINOGEN ASSEMBLY ON GOLD AND ITS CLOTTING INDUCED BY GOLD NANOPARTICLE 102

6.1 Fibrinogen assembly on gold 103

6.2 Fibrinogen clot induced by gold-nanoparticle 113

7 SUMMARY AND OUTLOOK 127

7.1 Summary 127

7.2 Outlook 130

REFERENCES 132

APPENDICES

A SUPPLEMENTS TO CHAPTER 2 152

B SUPPLEMENTS TO CHAPTER 5 166

LIST OF TABLES

Page

Table 1.1: Comparison of single-molecule manipulation techniques.....2

Table 1.2: Comparative summary of calibration method for cantilever sprint constant 15

Table 4.1: Kinetic and thermodynamic data. 74

Table 4.2: Experimental data used for the calculation of association binding constant 75

Table 5.1: Copolymer Composition of Organo-micelles.....92

Table B.1: Estimation of available functional groups on AFM tips with different sizes 169

Table B.2: The size, polydispersity index and CMC of micelles 171

LIST OF FIGURES

Page

Figure 1.1: The schematic configuration of single molecule techniques.....4

Figure 1.2: The cantilever oscillation signal is split into minima Umin and maxima Umax for generating topography and recognition image respectively 11

Figure 1.3: Conceptual energy landscape with one-barrier 18

Figure 2.1: The structure of compounds for gold surface modification 32

Figure 2.2: The synthetic scheme for Compound 1.....34

Figure 2.3: The synthetic scheme for Compound 2.....35

Figure 2.4: The synthetic scheme for Compound 3 and 4 35

Figure 2.5: ^{1}H-NMR spectrum of Compound 4 in Deuterochloroform ($CDCl_3$) 38

Figure 2.6: ^{13}C-NMR spectrum of Compound 4 in Deuterochloroform ($CDCl_3$) 39

Figure 2.7: The scheme for tip functionalization.....40

Figure 2.8: The structure of cross-linker for silicon related surface modification 40

Figure 2.9: The synthesis route for Compound 8 42

Figure 2.10: ^{1}H-NMR spectrum of Compound 11 in Deuterochloroform ($CDCl_3$) 45

Figure 2.11: ^{13}C-NMR spectrum of Compound 11 in Deuterochloroform ($CDCl_3$) 46

Figure 3.1: Schematic representation of AFM tip modification 50

Figure 3.2: Schematic representation of ricin immobilization on the gold surface 53

Figure 3.3: AFM topography and recognition of ricin molecules immobilized on Au (111) surface. 55

Figure 3.4: The blocking experiment....57

Figure 3.5: The dynamic force measurement....59

Figure 3.6: Free energy calculation....61

Figure 4.1: Optimized attachment of His-tagged Epha2....65

Figure 4.2: The profile of several functionalized surface....67

Figure 4.3: The tip modification procedure and its proof....68

Figure 4.4: The AFM recognition imaging of the YSA-EphA2 interaction....69

Figure 4.5: Histograms of rupture forces (left) and corresponding apparent loading rates (right) for EphA2-ligand complexes....71

Figure 4.6: Results of dynamic force spectroscopy for EphA2-ligand complexes....72

Figure 4.7: Results of EphA2 blocking with ligands....76

Figure 4.8: The AFM demonstration of the competitive binding of the YSA and ephrinA1 ligands to EphA2....78

Figure 5.1: Schematic illustration of the functionalized tip and its use in AFM recognition imaging and force microscopy for the micelles....89

Figure 5.2: Components for the assembly of multi-functional organomicelle....92

Figure 5.3: The topographical (a), phase (b) and amplitude (c) images of micelles **A** using Magnetic AC mode *(*MAC mode*)* AFM imaging....93

Figure 5.4: Topographic (top) and recognition (bottom) images....95

Figure 5.5: Time-laps recognition imaging of micelles A by the tip modified with 4-dibenzocyclooctynol containing linkers....97

Figure 5.6: Confocal images of tips labeled with Alexa Fluor® 488 azide and Rhodamine B TAG-loaded micelles **C**....97

Figure 5.7: Relationship between the contact time and number of polymers removed.....98

Figure 6.1: The stereo depiction of disulfide bonds (yellow colored ball) in the central E domain of fibrinogen.....105

Figure 6.2: The topographical image of fibrinogen on three different surface.....106

Figure 6.3: UV 405nm absorption of different concentration fibrinogen solution.....107

Figure 6.4: The fibrinogen growing process on gold surface 109

Figure 6.5: The high resolution image of fibrinogen.....110

Figure 6.6: The adsorption curve of fibrinogen on the bare gold surface 111

Figure 6.7: TEM images and statistical size analysis of gold nanoparticles 116

Figure 6.8: UV absorbance spectrum of the mixture solutions and the dependence of its related SPR shift on the fg concentration 117

Figure 6.9: Mean diameters from DLS measurement.....120

Figure 6.10: The AFM topographical images of the fg and GNP complexes 122

Figure 6.11: The topographical image of GNP on MICA surface.....123

Figure 6.12: The time-line images of the complexes formation.....123

Figure 6.13: The configuration of the complexes formation of the GNP and fg.....124

Figure A.1: ^{1}H-NMR spectrum of Compound 1 in Deuterochloroform ($CDCl_3$) 152

Figure A.2: ^{13}C-NMR spectrum of Compound 1 in Deuterochloroform ($CDCl_3$) 153

Figure A.3: ^{1}H-NMR spectrum of Compound 2 in Deuteromethanol (CD_3OD) 154

Figure A.4: ^{13}C-NMR spectrum of Compound 2 in Deuteromethanol (CD_3OD) 155

Figure A.5: ^{1}H-NMR spectrum of 2-(2-(2-mercaptoethoxy)ethoxy)ethanol in Deuterochloroform ($CDCl_3$) 156

Figure A.6: ^{13}C-NMR spectrum of 2-(2-(2-mercaptoethoxy)ethoxy)ethanol in Deuterochloroform ($CDCl_3$) 157

Figure A.7: ^{1}H-NMR spectrum of **Compound 3** in Deuterochloroform ($CDCl_3$) 158

Figure A.8: ^{13}C-NMR spectrum of **Compound 3** in Deuterochloroform ($CDCl_3$) 159

Figure A.9: ^{1}H-NMR spectrum of **Compound 9** in Deuterochloroform ($CDCl_3$) 160

Figure A.10: ^{13}C-NMR spectrum of **Compound 9** in Deuterochloroform ($CDCl_3$) 161

Figure A.11: ^{1}H-NMR spectrum of **Compound 10** in Deuterochloroform ($CDCl_3$) 162

Figure A.12: ^{13}C-NMR spectrum of **Compound 10** in Deuterochloroform ($CDCl_3$) 163

Figure A.13: ^{1}H-NMR spectrum of **Compound 12** in Deuterochloroform ($CDCl_3$) 164

Figure A.14: ^{13}C-NMR spectrum of **Compound 12** in Deuterochloroform ($CDCl_3$) 165

Figure B.1: The topographical, phase and amplitude images of micelles 166

Figure B.2: The schematics used to estimate the available functional groups 167

Figure B.3: Force loading rate, stretch distance, and 'Pull out' force histograms for micelle-A, micelle-B and micelle-C. 170

CHAPTER 1

INTRODUCTION AND LITERATURE REVIEW

1.1 Techniques for single molecule study

The diversity and dynamical fluctuation of molecules cannot be observed by conventional ensemble experimental techniques due to their averaging processes. In contrast, single molecule techniques measure properties of one molecule at a time so that usually hidden information can be uncovered. Due to their powerful capabilities, single molecule studies have contributed a lot to different disciplines, such as: physics, chemistry, and biology.[1] The development of single molecule studies is highly dependent on the technological advances.[2] Over the last 20 years, multiple single molecule techniques were developed. Briefly, they can be categorized into two big classes: fluorescence and manipulation methods.[1] Here, the manipulation methods will be the focus of our discussion.

Currently single molecule manipulation techniques include optical tweezers[3], magnetic tweezers[4], atomic force microscopy (AFM)[5], micro-needle manipulation[6], bio-membrane force probe[7] and flow-induced stretching[8,9]. Basically, all these manipulation techniques share a common geometry. One part of the molecule complex of interest is attached to the substrate surface with the other fixed on force probe (beads or AFM tip). By recording the dependence between the extension and force induced deflection, the mechanical properties of the molecule complex are determined. In each technique, the force probe is considered as a spring except for certain configuration of magnetic tweezers. The applied force is not measured directly but is typically determined via Hooke's law from probe stiffness and deflection of probe from its

equilibrium position.[10] Among these techniques, the first three are the most widely used and will be discussed in detail (***Table 1.1***). The unique features and limitations of each technique are highlighted by the wide variety of measurements. Here we will illustrate them with examples one by one.

Table 1.1 Comparison of single-molecule manipulation techniques. Typical values of bandwidth, stiffness, position resolution, force range, advantages, and limitations.[10,11]

	Optical Tweezers	**Magnetic Tweezers**	**AFM**
Bandwidth (Hz)	50-5000	10-1000	1000
Stiffness (pN.nm^{-1})	0.005-1	10^{-6}	1-10^{5}
Resolution (nm)	0.1-5	2-10	0.1-1
Force range (pN)	0.1-100	10^{-3}-10^{4}	5-10^{3}
Advantages	Low noise Low drift	Bead rotation	High-resolution imaging
Limitations	Photo-damage Sample heating Nonspecific	Force hysteresis Nonspecific	High-stiffness probe Nonspecific

1.1.1 Optical Tweezers (OT)

Optical tweezers (***Figure 1.1a***) can act as a displacement or force transducer. This capability is typified by the force and displacement measurement of optically trapped kinesin-coated beads moving along fixed microtubules.[12-14] In other applications, translocation and force generation of individual RNA polymerase molecule were studied as they transcribe DNA,[15] revealing the details of transcription including the stall force[16] (~30 pN), transcriptional pausing[17,18], and backtracking of the polymerase along the DNA template[19]. In addition to applied 'force', torque also can be imposed on the studied subject, which is typified by the study of birefringent particles.[20-22] Although all these applications embody the versatility and precision

afforded by optical tweezers, there are several limitations and drawbacks associated with the mechanism of OT:

1. Optical perturbations could result in ghost traps, spurious position signal, and other artifacts;

2. The high intensity of trapping laser could result in local heating;

3. The possible optical damage could be induced by the laser.

1.1.2 Magnetic Tweezers (MT)

Magneti Tweezers (***Figure 1.1b***) can also do the displacement as well as force measurement. Koster and co-workers applied MT to measure the relaxation of super-coiled DNA by topoisomerase IB as a function of load.[23,24] It avoids the problems of sample heating and photo-damage as OT. In addition to normal functions as force and displacement transducer, MT offers their unique feature, noninvasive measurement in complex and heterogeneous environments, including the interior of cells[25] and biopolymer networks[26]. Despite unique features of MT, the bandwidth and sensitivity of displacement are greatly limited by the video-based feedback system. The continuing technological and theoretical developments are needed to improve the performance.

1.1.3 Atomic Force Microscope (AFM)

AFM (***Figure 1.1 c***) was primarily an imaging tool with the resolution of sub 10 nm, which was initially developed as a complement to the limitation of scanning tunneling microscope (STM) in imaging non-conductive samples.[27,28] It can characterize soft materials in their natural condition, such as: polymer, cell membranes and bio-molecule. Distinct image modes of AFM can give out different information, for example: topography image shows the

surface structure[29] and phase image tells the composition difference[30,31]. Recently, a new imaging technique, called 'simultaneous topography and recognition imaging', was developed by Hinterdorfer and his coworkers[32]. This technique greatly extends AFM imaging capability, which can detect and locate the specific interaction sites between ligands and their cognate receptors by using a functionalized AFM probe to scan the molecule of interest on the surface. There are tons of works published, including antibody-antigen recognition[33-36], aptamer-protein interaction[37] and so on.

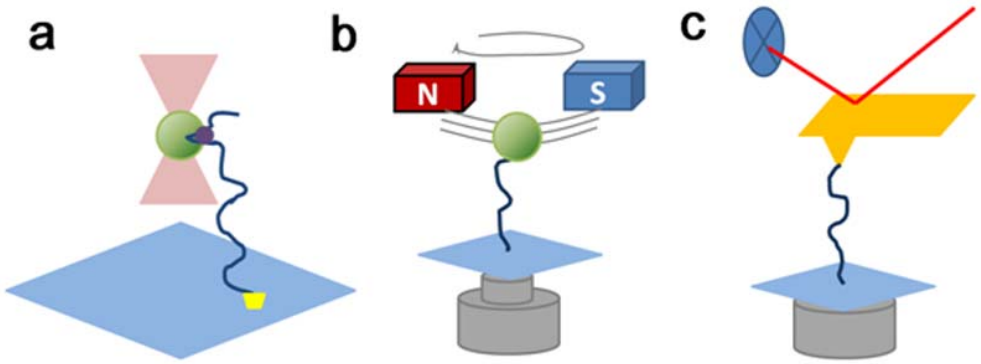

Figure 1.1 The schematic configuration of single molecule techniques. a) optical tweezers; b) magnetic tweezers and c) atomic force microscope.

In addition to imaging capability, it also allows measurement of inter- and intra-molecular interaction forces with piconewton resolution. It has been applied to study the rupture of molecule bonds, ranging from covalent bonds[38] to the unfolding of proteins[39] and nucleic acids[40]. It allows the discovery of unfolding intermediates[41], different unfolding pathway[42], and effects of force on protein function[43]. Although there are some limitations in AFM detectable force stemming from the size and high stiffness of cantilever, the force resolution is enough for most of biological processes. The major concern associated with AFM force spectroscopy is to discriminate interaction of the molecule of interest from nonspecific interactions.

Generally speaking, atomic force microscope is the most comprehensive method among these single manipulation techniques. It provides not only the force measurement with enough resolution, but also the image information. Due to these advantages, it will be adopted in my future study.

1.2 Evolution of AFM image capability

As mentioned above, the principle of AFM imaging process features that a sharp tip does raser-scan over the sample. AFM enables the non-destructive imaging of soft bio-materials in their close-to-natural environment with high resolution (~nm), offering a way to observe single molecule without the need for fixation and staining. The collected imaging signal can be split to distinct components to delineate special characteristics of sample, such as: topography, phase[31] and recognition image[32]. In the following, AFM image technique will be discussed in detail.

1.2.1 Technical Considerations

The acquisition time and resolution are two paramount factors for AFM imaging. They are coupled rather than independent. The acquisition time is determined by the scan size, setting pixels amount in one lateral direction, and scan speed, i.e., acquisition time is equal to (the scan size *pixel amount)/ scan rate. Commonly, one image needs couple of minutes. The scan speed of AFM is limited by the speed of the feedback loop.[44] Under this threshold, it is determined by the spring constant of the cantilever $\boldsymbol{k}$, its effective mass $\boldsymbol{m}$, the damping constant $\boldsymbol{D}$ of the cantilever in the surrounding medium and the stiffness of the sample. For soft biological materials, the scan speed should not exceed 2 μm/s when imaged in water at a desired resolution of 1 nm.[45] The longer the acquisition time, the larger the possibility of influence on image resolution by external noises, such as mechanical vibration or acoustic wave;[46] nevertheless, the

good vibration insulation system can minimize external noise very well. In addition to external noises, the intrinsic noises are inevitable, which also could corrupt the image resolution. There are two major sources for intrinsic noises[47]: the thermal noise (about $\frac{\sqrt{4k_BT}}{3k}$)[48] and noise from the cantilever deflection sensor[49]. As known, these noises are all related to basic characteristics of AFM probe. A careful probe selection will be much helpful to suppress these noises.

On the other hand, the quality of AFM probe also directly influences the image resolution.[50,51] The AFM probe can be described by several parameters including spring constant, tip radius and half cone angle. The typical values for these parameters range from 0.01 $N.m^{-1}$ to 100 $N.m^{-1}$, 2~10 nm, and 10~35º. Theoretically, the smaller the values of these parameters, the better the resolution of AFM image can be obtained for soft biological sample.[52] The blunt tip with large radius and half cone angle can introduce 'profile broadening' effect. Further, if the spring constant of selected AFM probe is too large, the elastic deformation of studied objects by AFM probe can introduce 'height lowering' effect into AFM image.[52] Both of these effects are common artifacts in AFM image. In general, the lateral resolution in AFM image is dependent on the characteristics of tip and the resolution in normal direction Z. The vertical resolution in Z direction is related to the feedback control system. Normally, it falls in the ranges of several angstroms and is better than that in later direction.[41]

To obtain an AFM image with high resolution, the chosen of a suitable probe is the first and also most important step. However, image resolution is not only a matter with AFM probe. For example, the accurate control of the interaction between the tip and sample through electrostatically balancing the contribution of attractive and repulsive forces can improve image resolution either.[53,54]

1.2.2 High resolution image of protein

As a general rule, the harder and flatter the sample, the higher the spatial resolution achievable.[50] For isolated protein on surface in aqueous solution, the best resolution is a few nanometers to tens of nanometer. In comparison, the real high resolution image at sub-nanometer resolution can only be acquired on 2D-crystallized[55-57] or densely packed protein,[58,59] and native membranes.[60] All these images were obtained in contact mode under the aqueous condition by using soft probe with spring constant of 0.1~0.2 N/m.

In one pioneering study,[57] streptavidin two-dimensional (2D) crystal formed on biotin-containing planar lipid layer can be imaged by AFM with sub-nanometer resolution, and its high-affinity binding capability and good flatness make it suitable as a platform for bio-molecule attachment in AFM studies.[56,61] This platform provides an optimal attachment strategy with controlled orientation of immobilized molecule and less perturbation to the biological function of the sample.

The high-resolution topography images of native photosynthetic membranes from several purple bacteria species[60,62] are also the milestone studies in AFM high-resolution imaging. They provided detailed views and rationales of membrane protein assembly adaptation in response to environmental factors, such as light intensity. It was found that photosynthetic complexes in native membrane of *Rsp. Photometricum* can rearrange in response to different light intensities. For example, the assembly of LH2 and core complexes showed up in high-light-adapted membrane and LH2-only antenna domains in low-light-adapted membranes.[60,63]

1.2.3 Phase image

The topography image offers the evidences about conformation information of bio-materials. However, it is impossible to differentiate the heterogeneous compositions of bio-materials. Amplitude-modulation atomic force microscopy (AM-AFM), that is, one kind of tapping mode, is widely applied in composition mapping.

Briefly, the mechanically or magnetically driven tip oscillation is used to probe and follow the variations of sample surface through the interaction between tip and sample surface. With the fixed excitation frequency, the amplitude and phase lag of oscillation reflect tip-surface conservative (elastic) and dissipative interaction (inelastic), respectively. While coupling between amplitude and the phase lag of the tip can be separated through operating the instrument at constant amplitude, they can further be applied to construct the topography and phase image. The correlation between phase-shift measurement and energy dissipation values can correspond the phase-lag to materials properties, such as stiffness, elasticity, viscosity or surface-adhesion energy qualitatively[30,31] or quantitatively.[64-66] Therefore, the 'phase imaging' empowers AFM to map out the compositional variations of the specimen's surface through the phase lag of the probe in response to the force between tip and sample surface.[29]

Tons of applications in biological field illustrate the promising potential of phase imaging in nano-scale characterization. In one of these interesting applications, the phase image was applied to *in-situ* observe the temperature induced phase transition of lipid bilayer. The solid supported dipalmitoylphosphatidylcholine (DPPC) bilayer shows a broad L_β-L_α transition.[67] In contrast to a free-standing bilayer (FSB), whose main transition is sharp and occurs at 23.7°C[68], the transition in the supported bi-layer of 1,2-dimyristoyl-sn-glycero-3-phosphocholine (DMPC) is much broader (8°C) and shifted to ~28°C.[69-71] Besides, phase images were applied to uncover

the detailed structures of the bacterial surface, including the flagella encapsulated inside the capsular extracellular polymeric substance (EPS).[72]

1.2.4 Chemical force microscope (CFM)

Although the phase image can distinguish the distinct compositions with different mechanical properties on sample surface, phase image lacks the capability to differentiate the compositions with similar mechanical properties but variant chemical components, such as self assembly mono-layer of mixture components (SAM). Chemical force microscope is the technique to achieve this aim, which extends AFM imaging with specific chemical sensitivity through hydrophobic effect or hydrogen bond.

To take advantage of the specific chemical interaction for imaging, AFM tip needs to be functionalized with SAM either by physically absorption[73,74] or covalent chemical bonding. The physical adsorption is not very robust. Therefore, its application is limited.[75] Comparatively, the chemical modification is widely used. Several mature procedures are already developed including SAM formed by organo-thiol compound on gold coated tip surface[76-78] and decoration of Si/Si_3N_4 tip surface by reactive organo-silanes.[79] Thus far, it was already demonstrated that chemical modified tip can sensitively map out the spatial distribution of specific function group through friction image.[75,78,80,81]

In these studies, the SAM in center square region terminates with COOH groups and the SAM surrounding the square terminates with CH_3 groups. Topography image failed to reveal this pattern since the regions of the two SAM have similar flatness. The tips with different chemical groups exhibit the chemical information about the surface. Friction image collected by COOH tips displays high friction on the COOH region and low friction on the CH_3 regions. In the opposite way, image recorded with CH_3 tips shows a reversal in friction contrast.[80] In addition,

chemical force microscopy was also accomplished to obtain chemically-sensitive image in tapping mode through relationship between phase lag and adhesion.[82]

1.2.5 Recognition image

To some degree chemical force microscope offers AFM the capability to map the distribution of specific function group on sample surface. However, its resolution, sensitivity and specificity are still on the way to be perfect.[75] The normal resolution is around 100~200 nm and extra efforts are required to improve its chemical sensitivity by altering the solvent characteristics, such as composition[83] or pH.[84] In addition, the intrinsic imaging mechanism based on hydrophobic effect or hydrogen bond hinder the CFM from doing well in specificity.[80] Hence, most of studies by CFM focused on simple model system and stayed in the stage of concept proof.

Recognition imaging technique can be taken as an advanced version of CFM, which features the specific interaction between probe and target molecule as imaging mechanism.[85] It offers much higher resolution (usually several nanometers) and better specificity.[86] Since this technique is based on magnetic driven AM-AFM, the gentle intermittent contact between tip and sample makes it suitable for imaging the soft biological sample, such as DNA complex[32,87] and protein.[32,85,88] In detail, the probe molecule is attached on tip surface through a polymer cross-linker. The introduction of extra long polymer cross-linker in tip surface is helpful to improve the flexibility and specificity of interaction. When the decorated tip scans over the sample surface, the damp of oscillation wave in both top and bottom part can be decoupled through special designed electronics, as shown in ***Figure 1.2***. The variation in top and bottom part of oscillation generates the topography image and recognition image accordingly. This technique has potency

for nanometer-scale epitope mapping of bio-molecules and localizing receptor sites during biological processes.

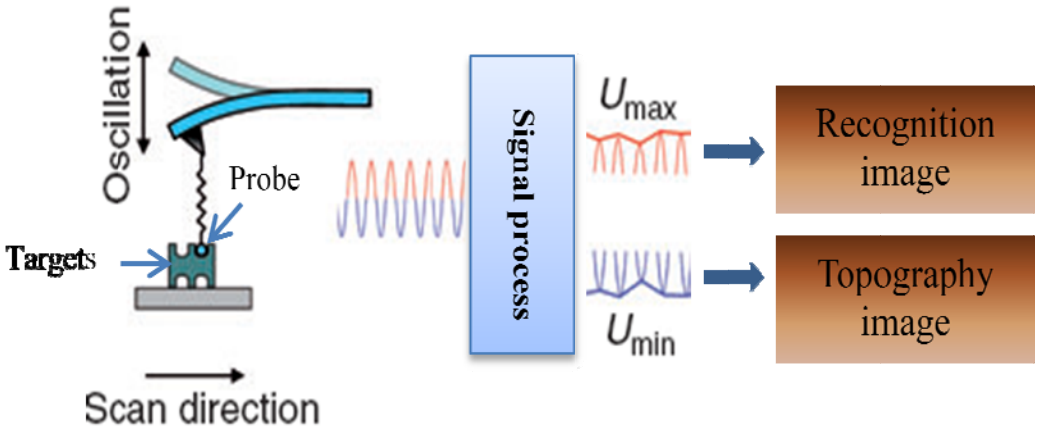

Figure 1.2 The cantilever oscillation signal is split into minima Umin and maxima Umax for generating topography and recognition image respectively.

After H.E. Gaub proved the concept that the specific interaction force can be applied to map the distribution of binding partners on samples in streptavidin pattern study by biotinylated tip,[89] the seminal work with formal nomenclature of 'recognition image' was performed by Peter.Hinterdorfer.[33] In this work, Lysozyme molecules fixed on the surface were recognized by the antibody on the scanning tip with a few nanometers lateral resolution. Later, this chromatin on substrate was imaged by its antibody on tip surface, and series of control experiments by BSA and ATP addition confirmed that the recognition events shown in image are specific.[32] In the follow-up work, an *in-vitro* selected DNA aptamer specific for histone H4 protein acetylated at lysine 16 was used to image synthetic nucleosomal arrays with precisely controlled acetylation by AFM recognition technique. The effect of acetylation on chromatin structure was investigated in nanometer-scale through the precise location of these posttranslational modifications by recognition image.[32,87]

1.2.6 High speed imaging

In addition to the imaging techniques mentioned above, which derived from interaction force manipulation and signal processing, lots of efforts were taken to decrease the normal image acquisition time in minute scale.[90,91] Benefiting from the understanding of the source of noise in the optical detection system and its effects on the probe motion,[92,93] currently the fast data acquisition time is already closed to video rate with the improved signal-to-noise ratio *via* minimizing tip-surface forces.[94,95] Those developments, in turn, enable the study of a wide variety of dynamical processes with unprecedented temporal and spatial resolution, in which the concomitant assessment of structure and dynamics is unfeasible before.[29] Its maximum imaging rate of 33 frames per second enables direct observing of bio-molecular processes in real time.[56,96]

In the recent publication in nature,[97] myosin V molecules translocating along actin filaments was directly visualized through high-speed atomic force microscopy. The area with size of around $90 \times 90\,\mathrm{nm}^2$ can be imaged with 100 × 100 pixel image in 80 ms. Previously speculated or demonstrated molecular behaviors, including lever-arm swing, was unambiguously proved by corroborative 'visual evidence'. Additionally, it reveals more detailed behaviors of the molecules, shedding light to a comprehensive understanding of the motor mechanism.

1.2.7 Summary

The high quality AFM probe ensures more chance to obtain the image with good resolution, contrast and fidelity. Small cantilever-tip systems with sharp tip radius, high Q value and chemical stability are greatly desirable. Small size of probe will enable high resonance frequency and small force, while reducing hydrodynamic damping in liquid. The high resonance frequency allows fast scanning rate[52] and small forces can decrease perturbations or deformation

of sample[86] when observing dynamic processes or the structure of nano-scale molecules. Besides, the consistence in tip quality is an important factor to ensure the reproducibility of data for quantitative measurement.

Additionally, the resolution and contrast in AFM images is determined by the interaction forces between the probe tip and sample surface, either specifically or nonspecifically. These interaction forces depend on surface chemistry, morphology, mechanical properties, and the nature of the surrounding medium.[52,75] In order to improve the imaging sensitivity and specificity, the wanted force for imaging process should be dominant over other forces, i.e., enhancing the wanted one as far as possible while suppressing the others. To achieve this aim, enough carefulness should be initiated from the sample preparation including sample immobilization and its surrounding environment. Later, the fine-tuning process of imaging parameter also plays a pivotal role in image resolution and contrast. This process is very delicate and requires strong expertise.[86]

1.3 Dynamic force spectroscopy (DFS)

DFS is another powerful capability of AFM for probing unfolding force in protein/DNA or the interaction forces between receptor and its cognate ligand. It can probe the force with the range from 10 to 10^4 pN,[11] further providing insight into the dynamics and kinetics of interaction process. To probe the specific interaction, the first pivotal thing is to decorate the probe and substrate with paired molecules either physically or chemically. In most cases, the molecule of interest is immobilized on the surface through a soft spacer, usually polyethylene glycol.[98] The measurement of rupture force is dependent on the bond formation between the molecule on probe surface and its cognate receptor on substrate, or vice versa, during contact. Once the bond formed, usually single bond, the probe or substrate is stretched from each other under constant

retracting speed. The bond rupture is signaled by the deflection of transducer to its rest position. The relation between deflection and time-dependent retracting distance is called 'force-distance curve' and the maximum deflection yields the rupture force. After abundant contacts, the rupture forces or unfolding forces are cumulated into a histogram. The peak in this histogram is the most probable force for breakage or unfolding and builds a statistical definition for bond strength. A well-defined peak in the force distribution reflects the limited period of survival of a bond under loading either. Moreover, the breakage or unfolding force is reliant on how fast force is applied to the bonds.[99]

1.3.1 Technical consideration

Since many reliable procedures are available for anchoring bio-molecules on AFM tips or supporting surface,[100] they will be addressed in the next section. Herein, some physical considerations in force probing and measuring process will be discussed.

Selection of AFM probe with optimized spring constant can offer good force sensitivity and low noise level as well as less perturbations or deformation of bio-molecules. The typical value of cantilever falls in the range of 0.01~1 N/m. As known, the magnitude of most interaction force between bio-molecules falls in the range from tens of pN to hundreds of pN.[11] To detect the force with enough sensitivity, normally the spring constant should not exceed 0.1 N/m.[86] However, it cannot be too soft since the position noise is reversely proportional to the spring constant of AFM probe. Hence, there is a compromise for probe stiffness considering from force sensitivity and spatial resolution.

Table 1.2 Comparative summary of calibration method for cantilever sprint constant[101]

Class of method	Method	Accuracy(%)	Accessbility	Demerit
Dynamic Response Methods	Resonance frequency with added mass	~10	Poor	Positioning and calibration of load difficult; potentially destructive
	Thermal fluctuations	10-20	Good	Temperature control essential; only for low K
	Simple scaling from resonace frequency	5-10	Poor	Depends on dimensional accuracy and determination of effective mass
Theoretical Methods	Finite difference calculation	>10	Poor	Depends on dimensional accuracy and Young's modulus
	Parallel beam approximation	>10	Poor	Depends on dimensional accuracy and Young's modulus
Static Response Methods	Static deflection with added mass	15	Poor	Positioning and determination of load difficult; potentially destruction
	Response to pendulum force	30-40	Poor	Complex and time-consuming procedure
	Static deflection with external standard	15-40	Poor	Require accurate external standard

Furthermore, interaction force is generally calculated from the deflection of cantilever with certain spring constant. If cross-linkers are included in the probing system, it is also necessary to take the stiffness of cross-linkers into consideration. In either case with or without cross-linker, the calibration of AFM probe is requisite to obtain precise force data. Currently, there are plenty of calibration methods available.[102,103] The widely used methods can be

categorized into four principal groups: 1) comparison with a reference cantilever of known stiffness; 2) calibration by thermal vibration; 3) addition of particle masses; 4) combining measurements of resonant frequency with physical dimensions and materials properties. ***Table 1.2*** provides an overview of these methods in term of accuracy, user-friendliness and demerit.

Additionally, the acquirement of dynamics and kinetic information needs to vary the loading rate over orders of magnitude. Since the loading rate is the product of retracting speed and system effective stiffness, this aim is achieved by altering the retracting speed between a few nm/s and a few μm/s.[104] However, the retracting speed is limited by the force sensitivity and the hydrodynamic effect. When AFM probe is retracted fast, the hydrodynamic effect has considerable contribution on the measured force. The force increasement Δf is determined by the probe damping coefficient ζ and retract speed v, i.e., $\Delta f = \zeta v$.[99,105] In general, the probe damping coefficient is proportional to the viscosity of the liquid environment and hydrodynamic profile length. Hence, normally the upper limit of retracting speed should be lower than 5 μm/s.[86] Although theoretically the lower limit is determined by free dissociation time, practically it cannot be too small since the external and internal noise will deteriorate the signal from interaction force due to longer durations.

1.3.3 Tip movement in DFS

Up to date, in most of force spectroscopy measurements AFM probe was retracted from the surface continuously. Under such circumstance, the contact time between probe molecule on AFM probe and its receptor on substrate was so limited that the probability to form the complex was very low, usually less than 20%. Additionally, nonspecific interaction shown in force curve was the main drawback in the continuous retracting mode. The complexity in the interaction between probe and support made these unwanted nonspecific interactions hard to be completely

avoided. Various ways were taken to relief this problem, such as surface passivation by non-ionic surfactant and double-tether method; however none of them successfully overcame it yet. The modulated retraction is another possible solution to this difficulty. It was currently widely used in molecule electronics study. It was first introduced by Xu in 2003 in electronics study of octanedithiol.[106] The applied small modulation in STM retraction introduced around 20% out-phase conductance variation of the measurement without modulation. Later, this modulation technique was extensively systematized and advanced by Chen and his coworkers.[107] In addition to the original saw-like modulation, several new modulation modes and even user-defined mode can be imposed on the retraction course. In the following up work, it was successfully applied in the conductance measurement by STM, used to increase the lifetime of molecular junction, screen out the complexity in contact part of the junction, and apply a voltage sweeping.[108] It is expected that this new retraction technique can contribute to AFM based force spectroscopy either.

1.3.4 Kinetic and Thermodynamic Theory for Single Molecule Force Spectroscopy

Bell model

In 1978, Bell pointed out that bond rupture is a statistical process and that the lifetime of a bond depends on the mechanical load. He also postulated that rate of unbinding increases exponentially with force.[109] Afterwards, Evans and his colleagues refined this theory from the underlined physics of bond strength.[110] In the following, the theory of one-barrier bond rupture was presented in detail.

A force-selected reaction path is featured by a single energy barrier, as shown in ***Figure 1.3***. The energy landscape $E(x)$ is mapped on a scalar coordinate x and external force is applied with some orientation θ relative to the molecular coordination. Starting from equilibrium, the

kinetic of dissociation are treated as a stationary flux of probability density along this preferential path from deep energy minimum outward past the barrier via a saddle point because of huge gap between thermal impulses (10^{-12}) and experimental force measurement (10^{-4}). In overdamped liquid environment, this transport is described by Kramers-Smoluchowski theory[99,111]. With consideration of force induced deformed energy landscape in the theory, the dissociation rate or frequency is given as (***Equation 1.1***):

$$v \approx \left(\frac{D}{L_c L_{ts}}\right) exp\left[-\frac{E_b(f)}{k_B T}\right] \qquad \textbf{\textit{Equation 1.1}}$$

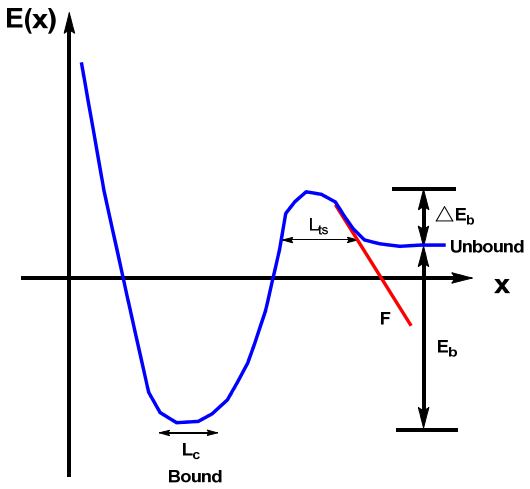

Figure 1.3 Conceptual energy landscape with one-barrier

The diffusive nature of overdamped kinetics is embodied in the term $\frac{D}{L_c L_{ts}}$, in which L_c is the thermal spread in the bound state and L_{ts} is the energy-weighted width of the barrier. L_c is defined as the gradient in density of states that drives dissociation, which could be derived from curvature of the energy landscape local to the minimum. L_{ts} is also calculated from curvature of energy landscape at the transition state x=x_{ts}. The shapes, levels, and location of intervening minima are altered with the force applied; however they have little impact on rate of dissociation provided that there is no switch in location of the primary minimum. On the other hand, shifts in

location and changes in width of barrier by external force merely introduce weak prefactor $g(f)$ dependent on applied force, which is insignificant for highly curved barriers because of the approximate constant location of transition state. The major impact of force on the frequency is from lowered barrier magnitude. It is proportional to a fixed distance x_β, i.e., $E_b(f) = E_b - f \cdot x_\beta$, which is thermal averaged projection $x_\beta = \langle x_{ts} \cos\theta \rangle$ of the transition state along the direction of force. Thus, the characteristic thermal force can be attained, i.e., $f_\beta = {k_B T}/{x_\beta}$, which is in the range from 40 pN to 4 pN. Hence, the kinetic rate has the following expression (***Equation 1.2***):

$$v(f) \approx \left(\frac{1}{t_0}\right) g(f/f_\beta) \exp\,(f/f_\beta) \qquad \textbf{\textit{Equation 1.2}}$$

where $\frac{1}{t_0} = (1/t_D) exp\,(-E_b/k_B T)$, inverse diffusion time $t_D = L_c L_{ts}(\gamma/k_B T)$, $g(f) = 1/L_{ts}$, and γ is viscous damping. As illustrated earlier, in normal probe test the force load rises at a constant rate ${\Delta f}/{\Delta t} = k_s v_t$ as determined by the speed of separation v_t and stiffness k_s of system including probe (k_f) and linkage (k_m). When force rises above the thermal force scale, the reassociation (on rate) by diffusion is negligible. Therefore, the probability density (***Equation 1.3***) is given as the product of dissociation rate and the likelihood of bond survival up to time *t* ($\exp\left\{-\int_0^t \mathrm{v[f(t')]} \cdot \mathrm{dt'}\right\}$):

$$p(t) = v[f(t)] \cdot exp\left\{-\int_0^t v[f(t')] \cdot dt'\right\} \qquad \textbf{\textit{Equation 1.3}}$$

For constant speed separation and elastic linkage, force and time become equivalent statistical variables correlated through the dynamic transformation $df = k_s v_t dt$. So the new expression based on force is given as ***Equation 1.4***:

$$p(t) = v(f) \cdot \left[\left(\frac{1}{v_t}\right)\left(\frac{\partial x}{\partial f}\right)\right] \cdot exp\left\{-\int_0^f v(f') \cdot \left[\left(\frac{1}{v_t}\right)\left(\frac{\partial x}{\partial f}\right)\right] df'\right\} \qquad \textbf{\textit{Equation 1.4}}$$

where $(\partial x/\partial f) = \frac{1}{k_f} + (\partial x_p/\partial f)$ is the total elastic compliance defined by transducer $\frac{1}{k_f}$ and polymer $\partial x_p/\partial f$ compliances.

Since the probability density for bond breakage is the product of an off rate that increases with time multiplied by the likelihood of bond survival that decreases with time, a maximum can occur in the distribution at specific time. Analytically, the most likely breakage force f^* or bond strength is derived from a maximum in the distribution, i.e., $\partial p/\partial f = 0$. (***Equation 1.5***)

$$f^* = \ln(r_f) + ln\left\{\left[\frac{\partial \ln(c)}{\partial f} + \frac{\partial \ln(g)}{\partial f} + 1\right]/c(f)\cdot g(f)\right\}_{f=f^*} \qquad \textbf{\textit{Equation 1.5}}$$

Where the dimensionless loading rate $r_f = k_f v_t/(f_\beta/t_o)$, the dimensionless total compliance $c(f) = \left[1 + k_f\left(\frac{\partial x_p}{\partial f}\right)\right]$. In the case that the cross-linker does not have any extension ($C \equiv 1$), the formula will turn into the form of Bell's postulation and it is clear that the bond strength depend logarithmically on the loading rate.

Jarzynski equality

In 1997, Jarzynski derived an equality which was used to attain the equilibrium free energy difference from the irreversible work[112,113]. Its application in analyzing single molecule pulling experiments was first done by Hummer and Szabo.[114] Later, Liphardt and his colleagues[115] compared Jarzynski's equality with the other two estimates, the average work and fluctuation-dissipation estimate, by carrying out RNA stretching reversibly and irreversibly. It showed that Jarzynski's equality can yield better results in the far-from-equilibrium regime. Further, the Jarzynski's equality was expressed in two more practical ways and their corresponding free energy reconstruction procedures were detailed illustrated.[116] One was called 'histogram based analysis', which has a prerequisite condition that a sufficient number of properly sampled pulling traces are available. For most of dynamic force stuides on interaction

between ligand and its cognate receptor, it was a big hurdle hampering its application in that the unbinding length showed a big discrepancy. The other one was moment-based analysis which practically requires less pulling traces. Thus, it was much convenient but with a larger error comparing to the former. It was proved that the overall free energy did not change significantly for N>40 and was independent on the pulling rate.[117]

Therefore, the momentum-based approach was adopted in our future work. In detailed, the accumulated work can be calculated by $W_t = \int_c F dq + V[q(t),t] - V[q(0),0]$. In that, $F = k(z(t) - q(t))$ is the restoring force, where k is the cantilever spring constant, q is the molecule extension, $z(t) = vt$ denotes the piezo movement in AFM experiment, which is the product of pulling rate v and time. $V[q(t),t]$ is the harmonic biasing potential of the cantilever at the time t and $V[q(0),0]$ is the initial potential. If the cantilever is relatively stiff than the cross-linker, most trajectories will be around $z(t)$, the position of the piezo actuator.[115] In this way, the form of weighted distribution of molecular extension by a Gaussian with mean is given as $\bar{q}_t = \frac{\langle q(t) e^{-\beta W_t} \rangle}{\langle e^{-\beta W_t} \rangle}$ and its corresponding variance $\sigma_t^2 = \overline{q_t^2} - \bar{q}_t^2$, Where, $\beta^{-1} = K_B T$. The first derivation of the potential of mean force can be calculated by taking the same approximation, that is, $G'(\overline{q_t}) = \overline{F_t} = \frac{\langle F(t) e^{-\beta W_t} \rangle}{\langle e^{-\beta W_t} \rangle}$. Finally, $G(q)$ can be obtained by the cumulative integration of the last formula.[116,117]

1.3.5 Summary

Although AFM based DFS has widely applications in biological field, its limitations were also exposed. The main drawbacks stem from the large size and relatively high stiffness of AFM probe.[11] The large size of AFM probe leads to high hydrodynamic effect in force measurement, which imposes a higher bound in retracting speed and augmentation in force measurement. Besides, the large stiffness brings about possible deformation of soft bio-molecule and low force sensitivity.

Specificity is a second major concern in many AFM based studies. Distinguishing between specific and nonspecific binding can be challenging.[11] The interactions shown in the force distance curve can be categorized into three classes: A) nonspecific tip-substrate interaction, B) nonspecific tip-ligand interaction, C) specific protein-ligand interactions.[118] The first class is easy to be excluded by the control experiment and existing theory; however, there is no good way to distinguish the second category from the third one.

Finally, the inaccurate measurement of probe stiffness and complexity of microscopic environment make force measurement hard to be consistent from independent studies. Even for the most studied system, streptavidin-biotin interaction, there is a very wide range of force value under the similar loading rate, which is from tens of pN to hundreds of pN.[119,120]

Continuous theoretical support and ultra-small AFM probe with small stiffness, good uniformity, reliability and chemical stability are expected to relief these dilemmas. Besides, the advancement of instrument may be helpful to current circumstance either, including lower detection system noise and faster piezoelectric response.

1.4 Molecule attachment

For AFM imaging and force spectroscopy at single molecule level, the flatness of the substrate is critical. Ultraflat substrates are necessary to ensure the success of experiment. There are several choices available, including highly oriented pyrolytic graphite (HOPG), mica, single crystal p (111) silicon wafer, and ultraflat gold. HOPG and mica are two natural materials, which are cleavable to generate 2D-crystalline surfaces with sub-nm flatness and perfect cleanness. The other two are artificial materials with comparable flatness. Although HOPG provides perfect physical characteristics, it is relative hard to be chemically modified for molecule attachment since the high toxic or corrosive agents, such as: HF, H_2SO_4 and HNO_3, are needed. So its application as substrate for AFM based single bio-molecule study is rarely reported.[121] Comparatively, mica and silicon wafer can be easily functionalized for immobilization of bio-molecules through silanization. However, the drawback of silanization is the difficulty to control surface properties. For example, usually derivatiation through silanization deteriorates the surface flatness very much, from original several angstoms to nanometers or even worse. The problem can be easily solved when ultraflat gold is used as support. The gold surface offers not only great flexibility to be functionalized in various ways without compromise in flatness, but also its chemical stability.[122] It is an excellent candidate for AFM based single molecule imaging and force study except for the relative high expense. On the other hand, the AFM probe is usually made of silicon or silicon nitride. It shares the similar chemical functionalization strategies as mica and silicon wafer. Sometimes, it can also be coated with a thin layer of gold. Although gold coated AFM probe also have great functionalization versatility, tip radius is possibly enlarged as a consequence of coating, resulting in the loss of image resolution.

After the appropriate substrate with expected characteristics is chosen, the molecule of interest and/or its cognate receptor should be attached to one or two solid surfaces, either substrate or probe surface. Ideally, the molecule attachment should be performed through the specific sites of the molecule, minimize the nonspecific adsorption, support infinite loads and not affect the mechanical or biological properties of the attached molecule.[11] These expectations are approximated by a variety of immobilization schemes ranging from physical adsorption to chemical covalent bonding. The physical adsorption is limited to certain specific molecules such as BSA, avidin, and lysozyme and also triggers the complications in surface functionalization scheme and force data interpretation. It is not a general method worth to be mentioned again. As for the chemical immobilization schemes, they can be exemplified as two categories according to the surface chemical characteristic including gold surface and silicon related surface.

1.4.1 Gold surface

Gold is the most useful one for single molecule study since it is a chemically inert surface with ultra-flatness and easy-functionalization capability.[121] The basic mechanism of decoration methods is the affinity between thiol related group and gold surface. The covalent bond between sulfur and gold is very strong so that its rupture force was shown to be >1nN, i.e., an order of magnitude higher than the non-covalent interaction between the bio-molecules. Moreover, the sulfur containing molecules can form a uniform assembly monolayer on gold without interfering much on the flatness of the surface. All these advantages make this type of weak covalent bond a good candidate for molecule attachment in AFM based single molecule measurement.

There were already a large number of applications in the related fields. First, many molecules have been directly chemisorbed to bare gold surface via their endogenous thiol or disulfide groups. Fab fragments of antibodies[123], azurin[124] and fibronectin[125] all bear a disulfide

bond in their structure, which is accessible to gold surface. Besides, in these cases the way of attachment keeps the bioactivity of these molecules. Comparatively, some manual synthetic peptide, such as Cys-Gly-His_6 peptides were chemisorbed onto gold surface via their carried thiols.[126] For some sample lacking accessible disulfide or thiols can be derivatized with thiol or disulfide containing tag for chemisorption to gold surface.[127,128] On the other hand, the molecules have also been immobilized stepwise on formed SAM through amide or thiolester bond as well as NTA chelating. The protein with endogenous surface lysine residues can be anchored on SAM surface with active ester ending group through amide coupling reaction.[129] For the molecule with available thiol group, maleimide group was applied to immobilize molecules through maleimide-thiol coupling.[130] The well-known specific interaction of hex-histidine peptides or His_6-tagged proteins with NTA-Ni^{2+} provided a strong and lasting attachment of proteins to surface.[85,131]

1.4.2 Silicon related surface

Several procedures for modification of silicon related surfaces have been well established. They can be summarized into three main categories, each one has its own pros and cons, and a mechanistic insight is essential for selecting appropriate one for specific application.

In term of the method based on organo-silanes, it is the most versatile one, which bears easy operation but high requirement on reagent quality. Various functional groups can be introduced including NH_2, CH_3, SH, alkene, and halogen.[118,119,132-134] Different operation conditions were used for silanization. Some relied on vapor deposition, others operated in solution, either under rigorously dry condition or in neat water as solvent, giving rise to the misleading impression that ‘anything goes’. The sight of behind mechanism can be helpful for understanding these differences. The silanol groups on surface is the key to organosilane based decoration. In the quartz, each Si atom carries one silanol group. Less regular surfaces contain

germinal silanols (two OH groups per Si atom), such as glass and silica gel. There is a layer of silicon dioxide covered on slilicon nitride and silicon surface. For mica, water plasma is essential to introduce silanol groups on its surface by removing the K^+ ion. Once there is silanol groups available on surface, the organosilane can form the covalent siloxane bridge with silanol groups through hydrolysis and condensation.[121] The base catalysis is the initiator for hydrolysis of the methoxy/ethoxy groups in organo-silane. It was found that the organosilane with monomethoxy/ethoxy was not active enough to perform the surface modification.[135,136] and the di-[137,138] and tri-methoxy/ethoxy[139,140] forms were eligible for this task. The dimethoxy/ethoxy form was the best choice to give a defined monolayer on silicon.[138] Comparatively, the trimethoxy/ethoxy can form monolayer or multilayer on surface, which was dependent on the relative humidity. For example, at 7% relative humidity the amount of adsorbed water was sufficient to form a stable monolayer of APTE (aminopropyl triethoxysilane) from the gas phase, whereas above 25% relative humidity a phase transition yielded ad double layer of APTE.[135] In conclusion, the surface silanol groups, trace of adsorbed water, base catalysis and specific organosilane (tri- or di-) were requisites for success and quality of surface modification.

The ethanolamine based method was developed in 1994[141] since it was found that 100 nm long tentacles were formed on the AFM tip when it was modified by widely used organosilane based method[142]. It also makes use of the silanol groups on surface and gives much convenient and efficient operation, but it has two distinct drawbacks. The first one is that its chemical mechanism is still vague. The other one is the discrepancy between expected and observed unbinding length was observed in force-distance curve, that is, unbinding length was always 10-30 nm longer than the sum of cross-linker length plus the length of paired interaction parties. Therefore, the organosilane based method is preferred for accurate measurement of unbinding

length and TREC imaging where the effective crosslinker length should not exceed 6 nm for optimal imaging conditions[143].

The silicon treated by 2% HF in water resulted in hydrogen terminated group on surface, which can be covalently coated by refluxing under nitrogen in α,ω-oligo(ethylene glycol) alkene solution in mesitylene.[144] Further, eletrooxidation was applied to selectively oxidize the chain termini into carboxyl group. The carboxyl group can be activated with EDC/NHS to immobilize the bio-molecule with amine group.

1.5 Objectives and Organization of this thesis

1.5.1 Objectives of this thesis

The objective of our researches is to apply both AFM based dynamic force spectroscopy and/or its imaging capability including topography and recognition image to study interaction and/or conformation of various biological or chemical systems at single molecule level.

Based on the discussion above, it is already known that AFM is the most comprehensive single molecule study technique, which not only has the imaging capability, but also offers the capability of force measurement with enough resolution. It was widely used in conformation study through imaging[145] and molecular interaction study by force spectroscope[146]. The conformation of bio-molecules has directly correlation with their function, such as: protein and nucleic acid. The investigation in single-molecular level would be helpful to understand the correlation.[147] On the other hand, the formation and dissociation of noncovalent interactions between varieties of macromolecules play a crucial role in biological system, colloidal system and polymeric materials.[148,149]

Due to its versatility, the applications range from DNA image in water[150] and single molecule topographical and recognition image (TREC)[32] to protein folding and unfolding,[151] RNA folding and unfolding[152] and protein/protein or ligand receptor interaction[153]. However, the current methodology for AFM force spectroscopy and imaging is suffering several drawbacks, including specificity of interaction and operation accessibility. To improve such circumstance, a comprehensive methodology is greatly needed, ranging from surface functionalization to measurement strategies, to increase the specificity of measurement and operation accessibility. An overall methodology aims to simultaneously characterize the conformation and interaction of interesting objects with more specificity and accessibility (***Figure 1.2***). The method includes several related aspects as below:

a) To achieve the purpose of imaging and force measurement, several surface functionalization strategies for molecule immobilization will be developed. By delicately designing the method of molecule immobilization on solid surface, the surface density and orientation of interested molecule can be controlled in some way, which is helpful to increase the probability of force measurement and passivate some of negative unspecific interactions;

b) The topography and recognition images of interested bio-molecule are collected simultaneously through AFM based TREC technique, which provide evidences of molecular structure and shed light onto the discovery of binding sites;

c) By locating AFM probe referring to the image, controlling and measuring the movement and deflection of AFM probe will provide more specific interaction force between the ligand and receptor, that is, the bond strength of the complex;

d) The interaction forces from the AFM measurement are further translated into the terms of macroscopic parameters, which are interested by biologists or chemists, such as: dissociation rate, binding rate, and free energy.

1.5.2 Organization of this thesis

In the following chapters, several interested objects will be studied, including ricin, EphA2, organomicelle and fibrinogen. In Chapter 2, the involved surface functionalization methods will be listed out. Chapter 3 shows that TREC and DFS techniques can be applied to perform ultra-sensitive detection work and investigate the fundamental interaction between ricin and its antibody. In Chapter 4, the drug screen process based on these techniques was demonstrated through comparing the interaction force of EphA2/Ephrin and EphA2/YSA. In the subsequent Chapter 5, we took advantage of TREC technique to map out the distribution of surface functional group on micelle and DFS to measure the stability of micelle with or without loading. The following Chapter 6 will introduce the different assemble characteristics of fibrinogen on various surfaces and fibrinogen coagulation process induced by gold nanoparticles. The final Chapter 7 will be the summary and outlook of the overall studies.

CHAPTER 2

SURFACE FUNCTIONALIZATION

2.1 Introduction

As mentioned previously, the functionalized AFM probe and firmly anchored molecules on support are essential for single molecule force spectroscopy and imaging, especially the recognition imaging. The qualities of these chemical modifications directly determine the performance of the study, such as the lifetime of AFM probe, the resolution of image and the accuracy of measured rupture force. The inadequate work can lead to artifacts in image and force data, in some instance can prevent the collection of any meaningful data.

In my studies, both silicon based surfaces (MICA, silicon wafer) and metal surface (gold surface) were adopted since all these surfaces are flat enough to sustain single molecule study. In the following sections, their surface functionalization methods will be introduced accordingly.

2.2 Instruments and Materials

Instruments. Negative Ion Matrix Assisted Laser Desorption Ionization - Time of Flight (MALDI-TOF) measurements were obtained on VOYAGER-DE Applied Bio-systems using α-cyano-4-hydroxycinnamic acid for PEG derivative or 2,5-dihydroxyl-benzoic acid for others as a matrix. ^{1}H-NMR spectra were recorded in $CDCl_3$ or D_2O on a Varian Merc-300 or Varian Inova-500 spectrometers equipped with Sun workstations at 300K. TMS (δ_H=0.00) or D_2O (δ_H=4.67) was used as the internal reference. ^{13}C-NMR spectra were recorded in $CDCl_3$ or D_2O at 75MHz on Varian Merc-300 spectrometer, respectively using the central resonance of $CDCl_3$ (δ_C=77.0)

as the internal reference. COSY, HSQC, HMBC and TOCSY experiments were used to assist assignment of the products. Size exclusion chromatography (SEC) was performed in Sephadex LH-20 filled column (40mm by 150 mm, maximum 100 mg loading per run) in serial connection with fraction collector (Frac-920 Fraction Collector, GE).

Materials. 3-Triethoxysilylpropylamine (APTE, Sigma-Aldrich Inc.), 3-Triethoxysilyl-1-propanethiol (MPTE, 80%, Sigma-Aldrich Inc.), *N*,*N*-diisopropylethylamine (DIPA, 99%, redistilled, Sigma–Aldrich Inc.), (±)-α-Lipoic acid (99%, Sigma-Aldrich Inc.), N-Hydroxysuccinimide (98%, Sigma-Aldrich Inc.), N,N′-Dicyclohexylcarbodiimide (puriss., 99.0%, Fluka), Dithiobis-succinimidylpropionate (DTSP, Fluka), Amino-nitrilotriacetic Acid (ANTA, Fluka), Triethylamine (99.5%, Sigma-Aldrich), 2-[2-(2-Chloroethoxy)ethoxy]ethanol (96%, Sigma-Aldrich Inc.), Thiourea (ACS reagent, 99.0%, Sigma-Aldrich Inc.), Iodine (99.99%, Sigma-Aldrich Inc.), Potassium iodide (99.5%, Sigma-Aldrich Inc.), Biotin (99%, lyophilized powder, Sigma-Aldrich Inc.), 4-(Dimethylamino) pyridine (DMAP, 99%, Sigma-Aldrich Inc.), Poly(ethylene glycol) (MW=1000, Fluka), p-Toluenesulfonyl chloride (TsCl, 99%, Sigma–Aldrich Inc.), Sodium azide (99.99%, Sigma–Aldrich Inc.), Triphenylphosphine (puriss., 98.5%, Fluka), (+)-Biotin N-hydroxysuccinimide ester (Biotin-NHS, 98%, Sigma-Aldrich Inc.), Bromoacetyl bromide (98%, Sigma–Aldrich Inc.), Pyridine (anhydrous, 99.8%, Sigma-Aldrich Inc.), hexane (97%, Sigma-Aldrich), All Chemicals were used without further purification. DCM was distilled from calcium hydride; THF from sodium; CH_3OH from magnesium and iodine. Aqueous solutions are saturated unless otherwise specified. All the reactions were performed under anhydrous conditions under argon and monitored by TLC on Kieselgel 60 F254 (Merck). Detection was by examination under UV light (254 nm) or by iodine vapor staining or by charring with 10 % sulfuric acid in methanol. Silica gel (Merck, 70-230 mesh) and Iatrobeads

6RS-8060 (Bioscan) were used for chromatographies. CS-10 silicon AFM probes were purchased from Nanoscience Instruments.

2.3 Gold Surface

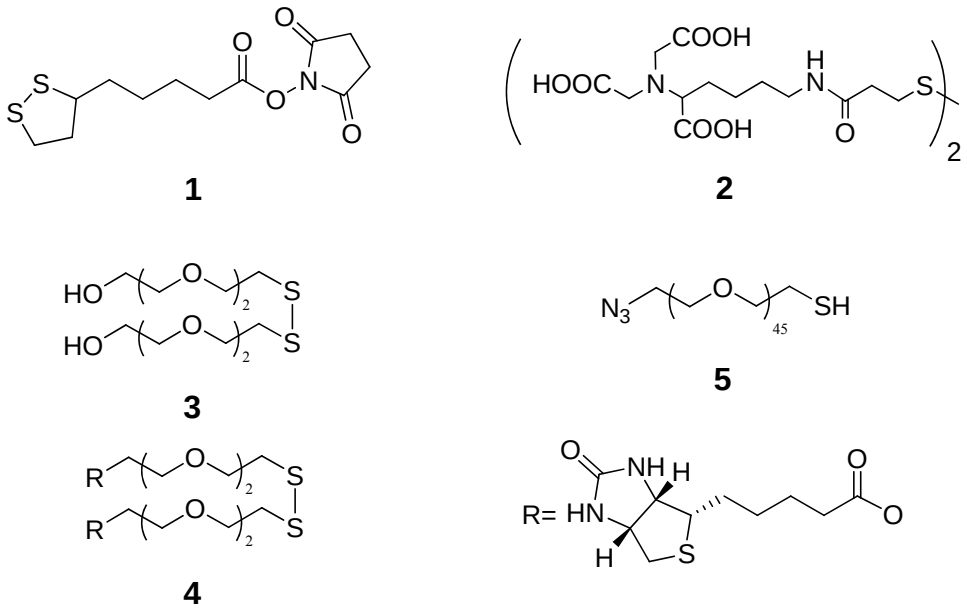

Figure 2.1 The structure of compounds for gold surface modification

The chemical modification on gold surface is based on the Au-S bond, both substrate and AFM tip functionalization can be achieved through this method. Because of its supreme flatness, the thermal deposited gold surface on mica is mainly used as substrate in my future studies. After it is annealed by hydrogen flame, it can provide sub-nanometer flatness in the area of several μm^2. For AFM tip derivatization, the tip can be simply coated with thin layer of gold to facilitate the subsequent modification work. To achieve the various requirements of samples, several compounds were synthesized, as shown in ***Figure 2.1***, and their corresponding immobilization methods will be introduced either.

Lipoic acid is activated into a more reactive form, **Compound 1**, which can not only form SAM on gold surface through the disulfide moiety, but also amide bond with the surface lysine residue on bio-molecule through the succinimide moiety. This method is pretty straightforward and efficient. However, it doesn't have too much control in the orientation of bio-molecule, which will disturb the bio-activity of bio-molecule and as a result introduce complexity in the force spectroscopy data. **Compound 2** bears disulfide moiety and triacetic acid moiety. The disulfide moiety can attach to gold surface. The resulted SAM exposes the triacetic acid moiety outside which can chelate with Ni^{2+} ion and further be used to immobilize the bio-molecule with histidine tag. The chelation is strong enough to provide firmly attachment and specific orientation of bio-molecule.[85,131] As a result, the binding site will not be perturbed by the immobilization. Besides, the one-step SAM formation will maintain the surface flatness comparing to previous multiple surface modification[85,131]. **Compound 3 and 4** are two derivatives of polyethylene glycol (PEG). They also carry with disulfide moiety for attachment on gold surface. The outward biotin moiety has strong affinity with strepavidin or avidin, which acts as a transition layer to attach biotin carried bio-moleules. Through regulating the molar ratio of these two compounds, the surface density of biotin moiety can be controlled and in turn the bio-molecule of interest. Except that, **Compound 3** is also helpful to prevent the nonspecific protein adhesion. In this way, the fidelity of force spectroscopy and recognition image will be improved. **Compound 5** has molecular weight of 2000, which carries with thiol moiety in one end and azide moiety in the other end. It was used to functionalize the gold coated AFM tip with azide moiety through forming self-assembly monolayer.

2.3.1 Synthesis of Compound 1

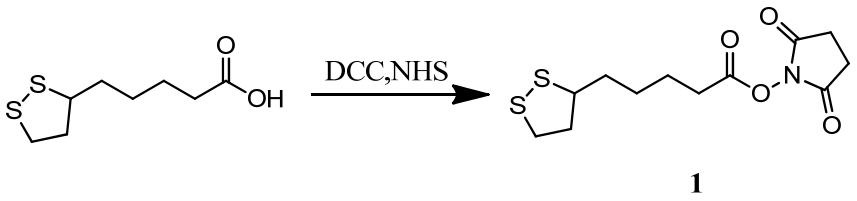

1

Figure 2.2 The synthetic scheme for **Compound 1**.

To a solution of D,L-thioctic acid (TA, 1.00 g, 5 mmol) and *N*-hydroxysuccinimide (NHS, 0.67 g, 6 mmol) in tetrahydrofuran (THF) (20 mL) at 4°C was added slowly a solution of *N,N'*-dicyclohexylcarbodiimide (1.2 g, 6 mmol) in THF (5 mL). (***Figure 2.2***) The mixture was allowed to warm to room temperature and stirring was continued for 5 h. The precipitate was removed by filtration and the filtrate concentrated in *vacuo*. The residue was dissolved in ethyl acetate (20 mL) and then filtered to remove insoluble material. The product was crystallized from a solution of hot ethyl acetate/hexane (1:1 v/v) to give, after drying *in vacuo*, D,L-thioctic acid-NHS ester a pale-yellow solid (1.0 g, 69%). ^{1}H NMR (300 MHz, $CDCl_3$, 298 K): δ=3.57 (1H, m, S-S-C*H*), 3.16 (2H, m, *S-S-CH*$_2$), 2.83 (4H, s, *CO-CH*$_2$-C*H*$_2$-*CO*), 2.62 (2H, t, *J* = 6 Hz, C*H*$_2$*CO*), 2.45 (1H, m), 1.93 (1H, m), 1.83-1.67 (4H, m), 1.62-1.53 (2H, m). ^{13}C NMR (75 MHz, $CDCl_3$, 298 K): δ= 169.4, 168.6, 56.3, 40.4, 38.7, 34.6, 31.0, 28.5, 25.8, 24.6. (***Figure A.1*** and ***2*** in APPENDIX A)

2.3.2 Synthesis of Compound 2

ANTA (78.4 mg, 0.3 mmol) was dissolved in 1 ml of water. DTSP (40.3 mg, 0.1 mmol) was dissolved in 1 ml dimethylformamide (DMF) and added into ANTA solution in water dropwise, following by addition of trimethylamine (80 µl, 0.4 mM). (***Figure 2.3***) The reaction

proceeded overnight at room temperature, the solvent was evaporated and the residue was purified by HPLC (water : acetonitrile), with 70% yield. ^{1}H NMR (300 MHz, CD_3OD, 298 K): δ=3.73(8H, m, *CH_2COOH*), 3.54(2H, t, *CHCOOH*), 3.20(4H, t, *$NHCH_2$*), 2.94(4H, t, *SCH_2*), 2.59(4H, t,CH_2CO), 1.76(2H, m), 1.52(4H, m). ^{13}C NMR (CD_3OD): δ=173.97, 173.82, 172.57, 65.66, 54.09,53.97, 38.89, 35.36, 34.00, 29.11, 28.72, 23.53. (***Figure A.3*** and ***4*** in APPENDIX A)

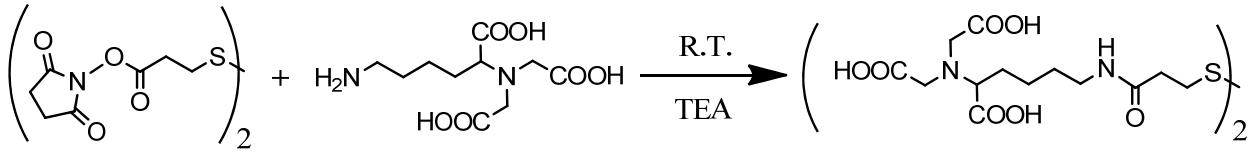

2

Figure 2.3 The synthetic scheme for **Compound 2**.

2.3.3 Synthesis of Compound 3 and 4

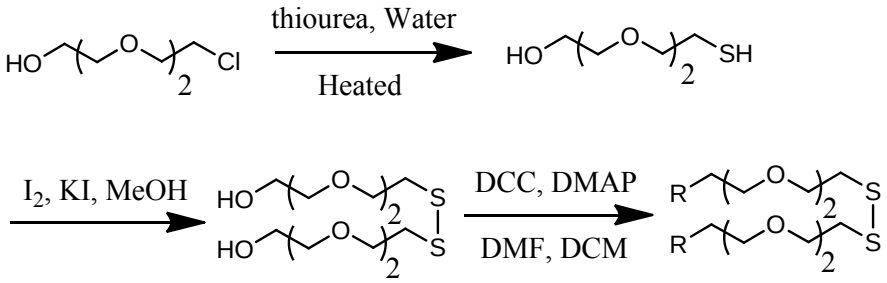

3 **4**

Figure 2.4 The synthetic scheme for **Compound 3** and **4**.

Synthesis of 2-(2-(2-mercaptoethoxy)ethoxy)ethanol A solution of 2-[2-(2-Chloroethoxy)ethoxy]ethanol (1.45 g, 8.6 mmol) and thiourea (2.7 g, 35mmol) in 23 mL of water was heated under reflux for 4h. After the addition of 30 mL of 2.5 M NaOH, the heating was resumed for an additional period of 4 h. (***Figure 2.4***) After the mixture was cooled at room

temperature, the PH was adjusted to 1 with concentrated HCl. The resulting solution was extracted seven times with 20 mL of $CHCl_3$. The combined extractions were dried on $MgSO_4$ and evaporated in *vacuo*. The oil-like crude was further purified through silica gel column with Hexane/Ethyl acetate (1:1). The compound was obtained as colorless oil (1 g, 70% yield). ^{1}H NMR (300 MHz, $CDCl_3$, 298 K): δ=3.55(10H, m), 2.62(2H, m, SCH_2), 1.53(1H, t, *HS*). ^{13}C NMR (CD_3Cl_3): δ=73.02, 72.74, 70.47, 70.38, 61.81, 24.36. (***Figure A.5*** and ***6*** in APPENDIX A)

Compound 3 was obtained through oxidation of 2-(2-(2-mercaptoethoxy)ethoxy)ethanol. In detail, potassium iodide (14 mg, 0.084 mmol) and iodine (353 mg, 1.39 mmol) were added to a solution of mono-thiol (461mg, 2.78 mmol) in methanol (20 mL) and the solution was kept stirred for 30 min.(***Figure 2.4***) The brown reaction mixture was decolored by sodium thiosulfate and the reactant was filtered. The filtrate was concentrated under reduced pressure. The remaining oil was re-dissolved in DCM and filtered again. The filtrated was concentrated again and dried in *vacuo*. The crude was purified by silica gel column. The product was eluted with DCM/MeOH (20: 1). **Compound 3** was obtained as yellow oil (300 mg, 85 % yield). ^{1}H NMR (300 MHz, $CDCl_3$, 298 K): δ=3.65(8H, m), 3.58(8H, s), 3.52(4H, t), 2.84(4H, t, CH_2SSCH_2). ^{13}C NMR (CD_3OD): δ=72.74, 70.55, 70.48, 69.74, 61.81, 38.57. (***Figure A.7*** and ***8*** APPENDIX A)

Compound 4 was obtained through condensation between **Compound 3** and biotin. First, biotin (458 mg, 1.876 mmol) was fully resolved in anhydrous dimethylformamide (DMF, 5 mL) with a little heating. Biotin in DMF, N,N'-Dicyclohexylcarbodiimide (DCC, 387 mg, 1.876 mmol) and 4-Dimethylaminopyridine (DMAP, 26 mg, 0.203 mmol) were added into a solution of **Compound 3** (155 mg, 0.469 mmol) in anhydrous dichloromethane (DCM, 5 mL).(***Figure 2.4***) The reactant was stirred under r.t. overnight. The cloudy reactant was filtered and filtrate was dried in *vacuo*. The remaining oil was re-dissolved in DCM and filtered again. The filtrated

was concentrated again and dried in *vacuo*. The crude was purified by silica gel column. The product was eluted with DCM/MeOH (20: 1). The Compound 4 was obtained as yellow oil (200 mg, 55% yield) ^{1}H NMR (300 MHz, $CDCl_3$, 298 K): δ=6.34(2H, br, *NH*), 5.77(2H, br, *NH*), 4.47(2H, m, *CH*), 4.28(2H, m, *CH*), 4.20(4H, m, OCH_2), 3.73-3.60(8H, m), 3.10(2H, m, *CH*), 2.87(4H, m, CH_2CO), 2.69(2H, d), 2.32(4H, m, CH_2S), 1.66(8H, m), 1.44(4H, m). ^{13}C NMR ($CDCl_3$): δ=173.91, 164.21, 70.68, 70.57, 69.80, 63.61, 62.19, 60.36, 55.84, 53.69, 40.80, 38.69, 34.04, 28.56, 28.44, 24.99. (***Figure 2.5*** and ***2.6***)

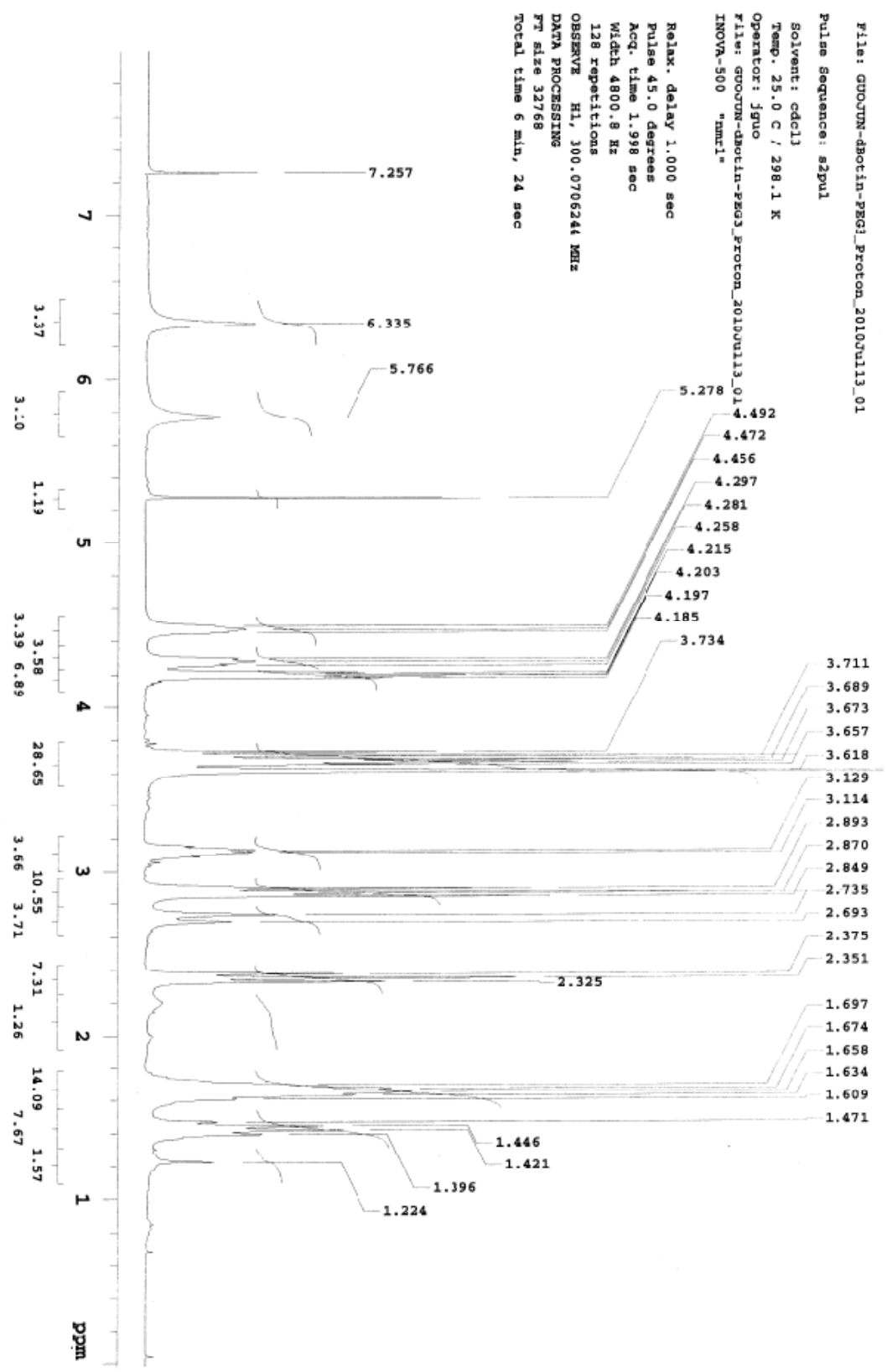

Figure 2.5 ^{1}H-NMR spectrum of **Compound 4** in Deuterochloroform ($CDCl_3$)

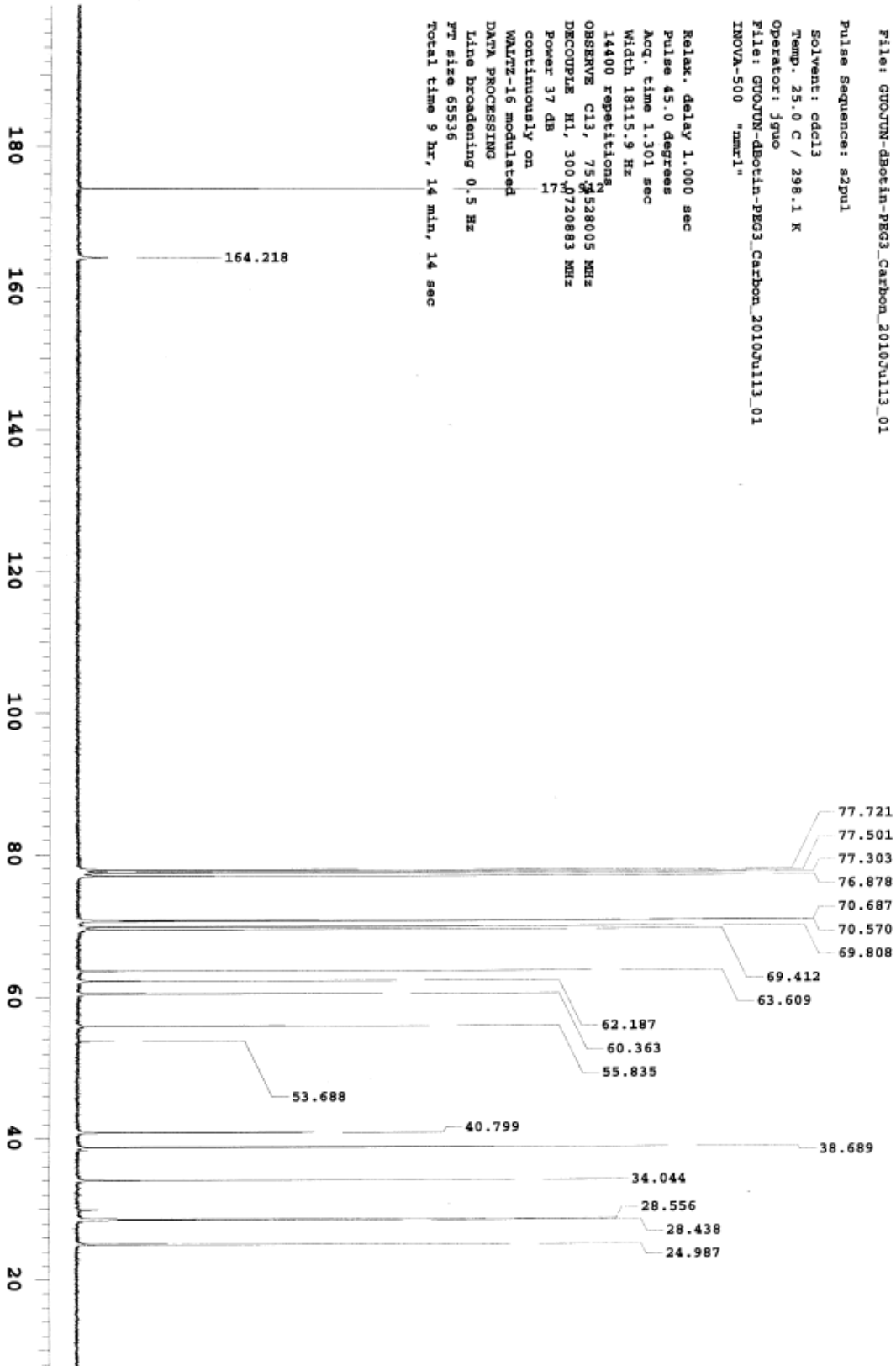

Figure 2.6 ^{13}C-NMR spectrum of **Compound 4** in Deuterochloroform ($CDCl_3$)

2.4 Silicon related surface

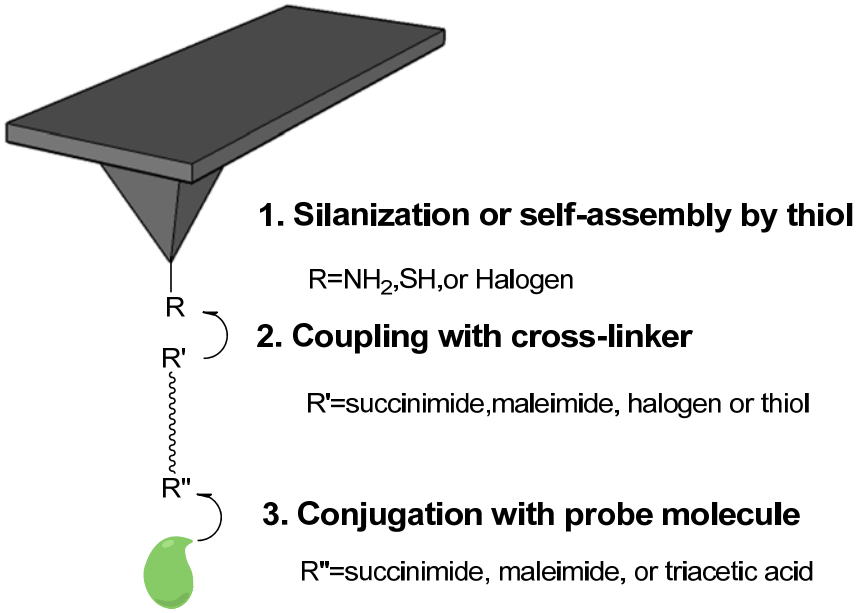

Figure 2.7 The scheme for tip functionalization.

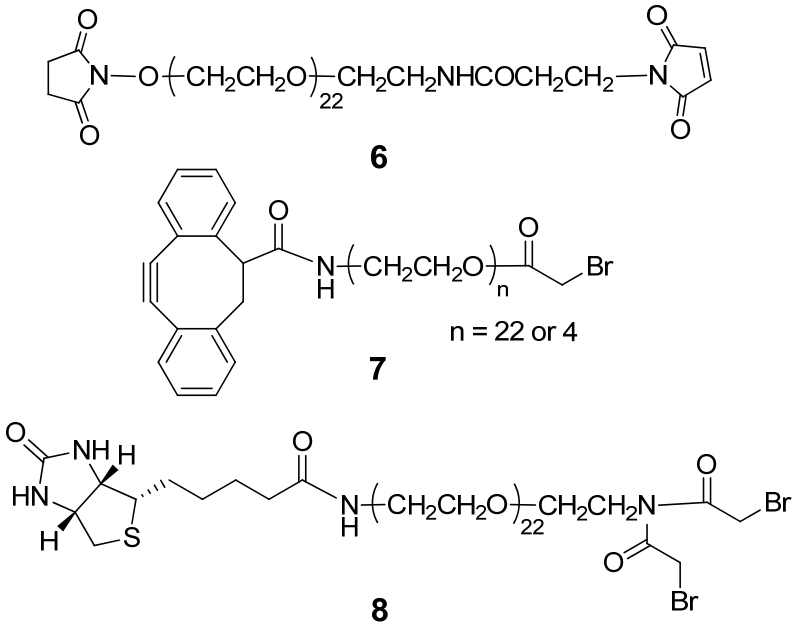

Figure 2.8 The structures of cross-linkers for silicon related surface modification.

The AFM tips are mainly made of Si_3N_4 or silicon and the extensively used substrates for AFM experiments include MICA, glass, and silicon wafer. The chemical modifications for all these materials are very similar and mainly based on the organo-silane without exception. Here, the AFM tip functionalization process is used as an example to illustrate the basic scheme. Usually the process includes three sub-steps shown in ***Figure 2.7***: Activation of AFM probe surface, coupling with cross-linker at one end, and conjugation with probe molecules at the other end of cross-linker. The activation of AFM can be achieved by silanization. The silanol groups on probe surface can react with organosilane, such as APTE, MPTE or other organo-silanes. Next, the functional groups decorated on probe surface will couple with the moiety at one end of cross-linker through amide, thiol ester, or others bonds. Several different cross linkers were used in my studies, as shown in ***Figure 2.8***. Finally, probe molecule can conjugate with the functional group left at the other end of cross-linker. Based on the functionalization of tip and substrate, the AFM imaging and force spectroscopy can be successfully carried out. The purposely designed functionalization methods will be helpful to both imaging process and force measurement.

2.4.1 Synthesis of Compound 8

Figure 2.9 shows the synthesis route for **Compound 8**. It started from polyethylene glycol with 1.0 K average molecular weight. First, TsCl (20.97 g, 110 mmol) and anhydrous pyridine (30 mL) was added to a solution of an uncapped 1.0 K average molecular weight PEG diol (50.0 g, 50 mmol) in anhydrous DCM (300 mL). The resulting mixture was stirred overnight at r.t.. The precipitate was filtered and the solvent was evaporated. The residue was dissolved in anhydrous DMF (200 mL) with addition of NaN3 (16.25 g, 250 mmol). The reactant was stirred at 80 °C overnight. The precipitate was filtered again and the solvent was evaporated. The crude was purified by silica gel column. The product was eluted with DCM/MeOH (20: 1). Compound

9, the attained pale yellow solid (45 g, 90% yield) was characterized by MALDI and used for the next selective Staudinger reaction. MALDI HRMS: m/z 1139.8, 1184.0, 1228.9 [M-N_2]. ^{1}H NMR (300 MHz, $CDCl_3$, 298 K): 3.63-3.58(92H, br, CH_2CH_2), 3.32(4H, m, N_3CH_2). ^{13}C NMR ($CDCl_3$): δ=70.87, 70.85, 70.81, 70.75, 70.21, 50.86. (***Figure A.9*** and ***10*** in APPENDIX A)

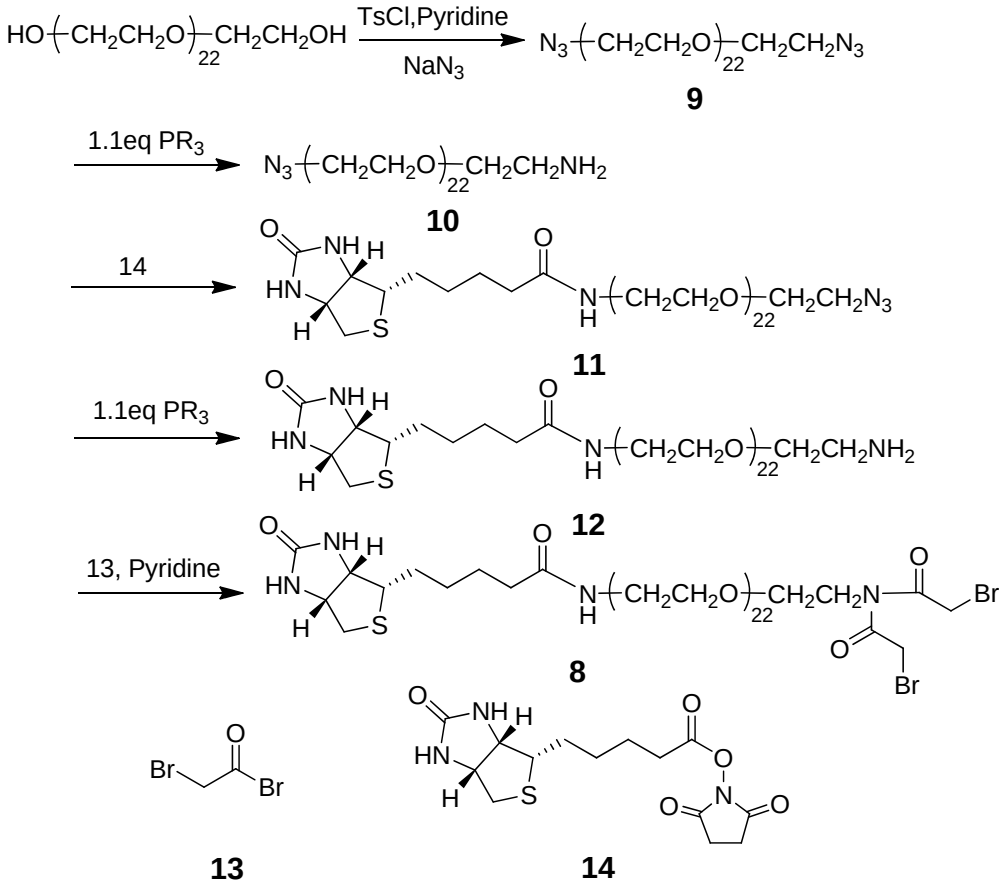

Figure 2.9 The synthesis route for Compound 8.

PPh_3 (2.51 g, 9.56 mmol) and H_2O (3 mL) were added into Compound 9 (8.37 g, 7.97 mmol) in THF (100 mL). The reaction was monitor by check TLC plate stained by ninhydrin in ethanol. The reactant was kept react overnight at r.t. under argon protection. The solvent was evaporated under high *vacuo*. The crude was purified by silica gel column. The product was eluted with DCM/MeOH/TEA (10: 1:0.1). Compound 10, the attained pale yellow solid (4 g, 48%

yield), was characterized by MALDI and used for next condensation reaction. MALDI HRMS: m/z 982.2, 1026.2, 1070.2 [M-N_2]. ^{1}H NMR (300 MHz, $CDCl_3$, 298 K): δ=3.93(2H, m, $NH_2CH_2CH_2O$), 3.67(92H, br, CH_2CH_2O), 3.39(2H, m, N_3CH_2), 3.18(2H, m, $NH_2CH_2CH_2O$). ^{13}C NMR ($CDCl_3$): δ= 70.90-69.92, 66.99, 50.89, 40.68. (***Figure A.11*** and ***12*** in APPENDIX A)

Biotin-NHS (0.39 g, 1.131 mmol), TEA (0.240 mL, 1.74 mmol) and acetonitrile (5 mL) were added into Compound 10 (0.87 g, 0.87 mmol) in anhydrous DCM (5 mL). The reactants were stirred overnight under argon protection. The cloudy reactant was filtered and filtrate was dried at *vacuo*. The crude was purified by silica gel column. The product was eluted with DCM/MeOH (10:1). Compound 11, the attained pale yellow solid (0.6 g, 57% yield), was characterized by MALDI and NMR. MALDI HRMS: m/z 1144.8, 1188.9, 1132.9, 1176.8 [M+Na^++H_2-N_2], 1164.8, 1208.8, 1252.9 [M-N_2]. ^{1}H NMR (300 MHz, $CDCl_3$, 298 K): δ=6.84(1H, br, *NH*), 6.62(1H, br, *NH*), 5.80(1H, br, *NH*), 4.39(1H, m, *CH*), 4.19(1H, m, *CH*), 4.00-3.25(80H, br), 3.03(1H, m, *CH*), 2.79-2.64(2H, br, SCH_2), 2.12(2H, m, $NCOCH_2$), 1.59(4H, br), 1.33(2H, br). ^{13}C NMR ($CDCl_3$): δ=173.56, 173.50, 164.30, 71.45-70.08, 61.88, 60.36, 55.81, 50.82, 50.79, 42.87, 40.64, 39.26, 36.07, 29.78, 28.40, 28.30, 25.76. (***Figure 2.10*** and ***11***)

Compound 12 (0.23 g, 89% yield) was obtained from Compound 11 (0.258 g, 0.215 mmol) by following the same procedure as Compound 10. MALDI HRMS: m/z 1123.9, 1167.9, 1212.0 [M+H^+] 1145.9, 1190.0, 1234.2 [M+Na^+] 1161.9, 1205.9 [M+K^+]. ^{1}H NMR (300 MHz, $CDCl_3$, 298 K): δ=6.84(1H, br, *NH*), 6.62(1H, br, *NH*), 6.18(21H, br, *NH*), 5.80(2H, br, NH_2), 4.39(1H, m, *CH*), 4.19(1H, m, *CH*), 4.00-3.25(80H, br), 2.20(2H, m, $NCOCH_2$), 1.68(4H, br), 1.44(2H, br). ^{13}C NMR ($CDCl_3$): δ=173.45, 163.94, 158.90, 70.91-70.03, 61.96, 60.38, 55.71, 53.10, 50.79, 40.74, 40.55, 39.34, 36.07, 29.88, 28.33, 25.76.(***Figure A.13*** and ***14*** APPENDIX A)
A solution of Compound 12 (100 mg, 0.083 mmol) in anhydrous CH_2Cl_2 (10 mL) was placed

under an atmosphere of Argon and then bromoactyl bromide (51 mg, 0.83 mmol) and pyridine (33 mg, 0.3 mmol) were added. After stirring the reaction mixture overnight at ambient temperature, the solvent was removed under reduced pressure and the residue was purified by silica gel column chromatography (CH_2Cl_2/CH_3OH, 30/1, v/v) to afford Compound 8 (74 mg, 67%). MALDI HRMS: m/z 1188.2, 1232.2, 1276.2, 1320.2, 1364.2, 1408.3, 1452.4, 1496.5 [M].

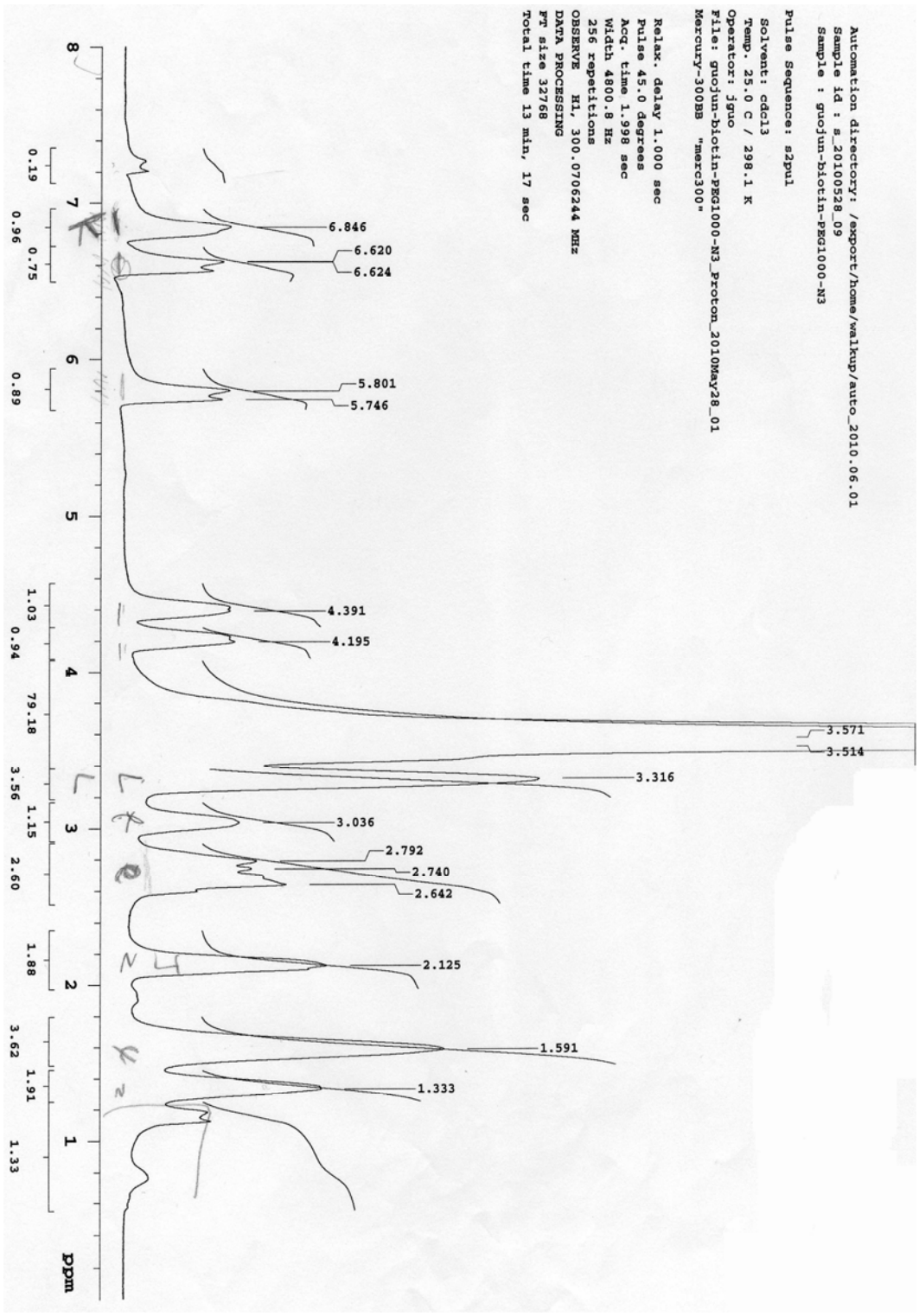

Figure 2.10 ^{1}H-NMR spectrum of **Compound 11** in Deuterochloroform ($CDCl_3$)

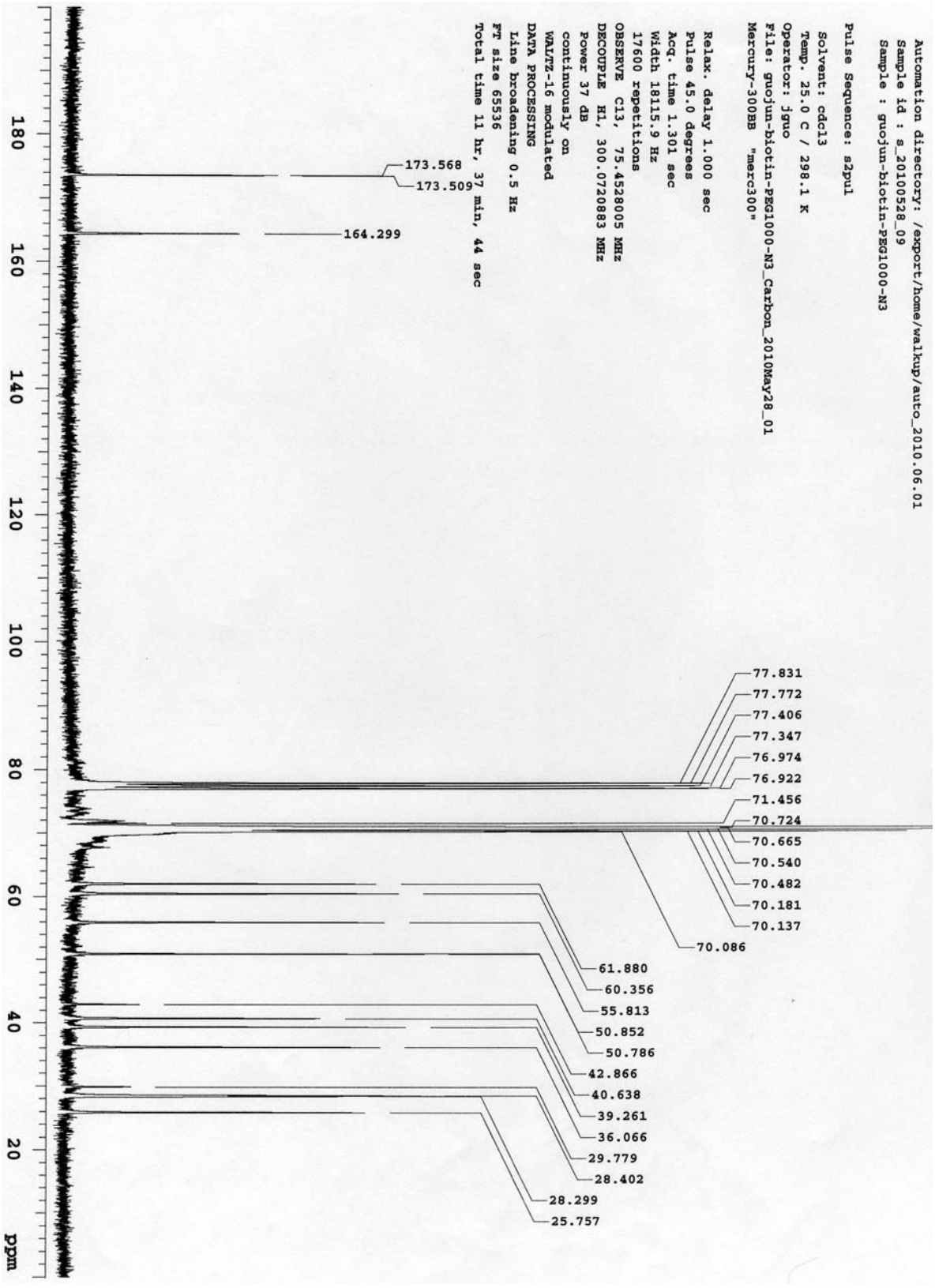

Figure 2.11 ^{13}C-NMR spectrum of **Compound 11** in Deuterochloroform ($CDCl_3$)

2.5 Conclusions

To achieve the purpose of imaging and force measurement, several organo-sulfurs and polyethylene glycol derivatives for molecule immobilization were synthesized to facilitate the immobilization of biomolecule of interest. By delicately designing the method of molecule immobilization on solid surface, the surface density and orientation of interested molecule can be controlled in some way, which is helpful to increase the probability of force measurement and suppress some of negative unspecific interactions in imaging and force measurement.

The designed molecule immobilization methods not only offer useful platforms for AFM based single molecule imaging and force spectroscopy, but also benefit other techniques requiring special surface functionalizations, such as: surface plasmon resonance (SPR), quartz crystal microbalance (QCM), and micro-fluid.

CHAPTER 3

RICIN DETECTION AND INTERACTION STUDY

3.1 Abstract

The authors report a study of detecting ricin molecules immobilized on chemically modified Au (111) surface by chemomechanically mapping the molecular interactions with a chemically modified AFM tip. AFM images resolved the different fold-up conformations of single ricin molecule as well as their intra-molecule structure of A- and B- chains. AFM force spectroscopy study of the interaction indicates that the unbinding force has a linear relation with the logarithmic force loading rate, which agrees well with calculations using one-barrier bond dissociation model.

3.2 Introduction and literature review

AFM with molecular recognition module is gaining increasing attention.[154] It offers a rapid and sensitive tool for molecular identification and interaction studies[146,155,156]. Due to its high sensitivity and fast imaging process, it could be a high-resolution alternative for detection of deadly biological warfare agents (BWA), such as ricin toxin.

Ricin toxin, which is a byproduct of castor oil production, was discovered in the seeds of castor bean plant, *Ricinis communis*. It is a heterogeneous proteinaceous toxin, which consists of many different proteins[157,158]. The average lethal dose of ricin in humans is approximately 0.2 mg, which makes it 6000 times more toxic than cyanide and 12000 times more lethal than rattlesnake venom by weight. There is no antidote for ricin toxin once introduced above the lethal dosage[23]. In addition, ricin can be formulated in a variety of physical forms including powder, mist, pellet, or dissolved in water or weak acids. Due to its ready availability, high toxicity, and stability, ricin has the potential to be used in bioterrorism attacks. For this reason, a

rapid, sensitive, and quantitative detection method for trace amounts of the toxin is greatly needed[159,160].

The current detection approaches for ricin are mostly based on traditional immunological methods, such as radioimmunoassay (RIA)[161], enzyme-linked immunosorbent assay (ELISA)[162], and enhanced colorimetric and chemi- luminescence ELISA[163]. However, lengthy assay time and limited throughput make these methods impractical for rapid responses. Numerous alternative techniques have been developed, and examples include functionalized gold nanoparticle[164,165], capillary electrophoresis (CE)[166], hybrid combination of quadrupole with time-of-flight (Qq TOF) [167], and hydrogel-based protein microchips[168]. Although the detection time is greatly decreased, these methods still do not meet all the requirements for sensitive, rapid, and inexpensive detection of toxins.

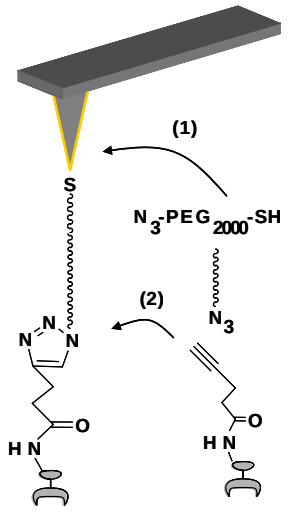

Figure 3.1 Schematic representation of AFM tip modification. (1) The thiol moiety of PEG_{2000} formed a SAM on the gold-coated tip; (2) the anti-ricin Ab with an alkyne group attached to the tip through click chemistry.

To apply the AFM technique in the detection work, tip modification is a critical step[100,169]. As discussed previously, AFM tip functionalization process generally entails three steps, namely modification of a tip surface, grafting of a cross-linker, and conjugation of a biomolecule[32,85,170]. Here, a simplified method was developed to modify AFM tip based on the powerful "click chemistry"[171,172], which facilitated practical and sensitive detection of toxins.(***Figure 3.1***) A key feature of the approach involves the use of a polyethylene glycol derivative (compound **5**, ***Figure 3.3***) with a thiol and azide end group. The thiol moiety of the PEG derivative enables attachment to a gold-coated tip without the need for initial tip modification. The azide of the immobilized PEG can then be employed in a Cu^{I} catalyzed 1,3-dipolar cyclization with an alkyne moiety of an appropriate biomolecule. This cycloaddition reaction, which has been coined 'click chemistry", is attractive because it can be performed at room temperature to provide stereospecifically stable triazoles in high yield and compatible with a variety of solvents and functional groups[173]. An anti-ricin antibody (anti-ricin Ab) with alkyne moiety was anchored on AFM probe surface, which made it possible to qualitatively and quantitatively detect ricin by AFM[160]. In addition, the interaction between these two biomolecules can be studied, which would give extra information to confirm the binding between anti-ricin Ab and ricin.

3.3 Experiments

3.2.1 Materials

Fluorescein labeled Ricinus Communis Agglutinin II (RCA II, RCA60, ricin) (Vector Laboratories Inc.), affinity purified goat anti-ricinus communis agglutinin I&II (1mg/ml, Vector Laboratories AS-2084), regenerated cellulose dialysis membrane (MWCO=3500) (Membrane Filtration Products, Inc.), 1-(5-[1,2]dithiolan-3-yl-pentanoyl)-pyrrolidine-2,5-dione (LA-NHS,

Compound **1**), pentynoic acid 2,5-dioxo-pyrrolidin-1-yl ester (Alkyne-NHS), HS–$PEG_{(2000)}$–N_3, PNS buffer (10mM phosphate, pH=7.8, 0.15M NaCl, 0.08% Sodium Azide), CS-10 silicon AFM probe (Nanoscience Instruments).

3.2.1 Alkyne modification of Anti-Ricin Ab.

Commercial anti-ricin Ab in a PNS buffer (200 μL, 1 mg/mL) was dialyzed using a regenerated dialysis membrane (MWCO:3500 Da, two Quick Seps) in purified water (18.2 MΩ) at 0 °C for 12 hours. Salt removal was deemed important to avoid possible inference with the conjugation reaction. The resulting anti-ricin Ab (200 μL) was mixed with alkyne NHS (200 μL, approx 1mg/mL) in dimethyl sulphoxide/CH_2Cl_2 (1:1). The mixture was stirred at 0 °C for 1 hour. Next, the solution was extracted with ethyl acetate (3 x 400 μL) to remove the active ester residues and the aqueous solution was placed in Quick Seps and dialyzed against water at 0 °C for 12 hours.

3.2.2 Functionalization of AFM tip

The Functionalization steps were shown in ***Figure 3.1***. Tips were coated with 20~30 nm of gold using an E-beam evaporator and then immersed in HS–$PEG_{(2000)}$ –N_3 in chloroform (5 mg/mL) at 4 °C for 10~12 h to form a compact SAM [174]. The PEG modified tips were washed with dimethyl sulphoxide followed by purified water three times. The tips were placed into alkyne modified antibody solution (200 μL, 0.1 mg/mL) and then sodium ascorbate (3 μL, 1 M) and copper (II) sulfate (1μL, 0.3 M) in water were added to the solution [175]. The click reaction was allowed to perform for 10~12 hours in the dark at 0 °C. Finally, the tips were washed by PNS buffer three times and stored in PNS buffer at 4 °C.

3.2.3 Ricin immobilized on the functionalized gold substrate

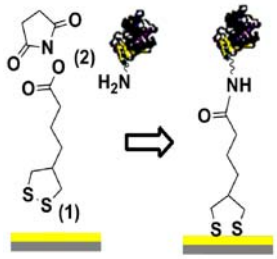

Figure 3.2 Schematic representation of ricin immobilization on the gold surface. (1) active ester **10** attached to the gold coated mica surface by the thioctic acid moiety; (2) ricin binds to active ester **10** by forming amide bond with amine groups on the protein surface.

The ricin immobilization on gold surface was shown in ***Figure 3.2***. A fresh thermal gold-coated mica substrate was annealed by a hydrogen flame for 2 min, and then LA-NHS in dichloromethane (200 μL, 5mg/ml) was immediately added to the surface. The substrate was kept at 4 °C for 3 hours[176]. Following rinsing by dimethyl sulphoxide and purified water, 200 μL (24 fg/mL) of ricin solution was put on the surface. The mixture was maintained at 4 °C for 30 min.

3.2.4 AFM experimental setup

An Agilent 5500 AFM system equipped with an inverted light microscope (ILM) system (Agilent, Chandler, AZ) was used. An Agilent multi-purpose AFM scanner was used for scanning an area of 10 μm^2. Silicon cantilever tips with a nominal spring constant of about 0.1 N/m were used throughout the experiments. All the images were taken in buffer using recognition imaging module based on Agilent magnetic AC (MAC) mode AFM with a

magnetically-coated lever. The detailed parameters for the image were as follows: drive was approximately 46%, resonance gain was 2, resonance frequency was 12.95 KHz, resonance amplitude was 1.68 v, and scan rate was 1.22 line/s.

3.4 Results and discussions

3.3.1 Tip and substrate modification

A novel approach for AFM tip modification has been developed employing bifunctional PEG derivative, Compound **5**. The thiol moiety of Compound **5** allows convenient attachment to a Au modified tip because of the high bond energy of the Au-S bond which ranges from 20-35 kcal/mol (85-145 kJ/mol) and its ability to form compact monolayers[176]. The azido moiety of the resulting SAM can then be employed in click reactions with biomolecules modified with alkynes.

An anti-ricin Ab was modified with alkyne groups by aminolysis with NHS ester of 4-pentynoic acid**,** Compound **1**. The NHS ester can easily be prepared by the esterification of the carboxylic acid with hydroxysuccinimide using EDC. Alkyne modified anti-ricin Ab was then attached to the SAM using a Cu (I) catalyzed reaction between azide of tip and alkyne of the toxin.

For ricin immobilization to gold-coated mica substrate surface, LA-NHS was employed which contains a thioctic acid moiety for immobilization to the gold surface and an activated ester for capturing of proteins. The thioctic was deemed attractive because it forms more stable complexes with gold with two Au-S bond compared to monothiol ligands[176].

3.3.2 Ricin detection and recognition

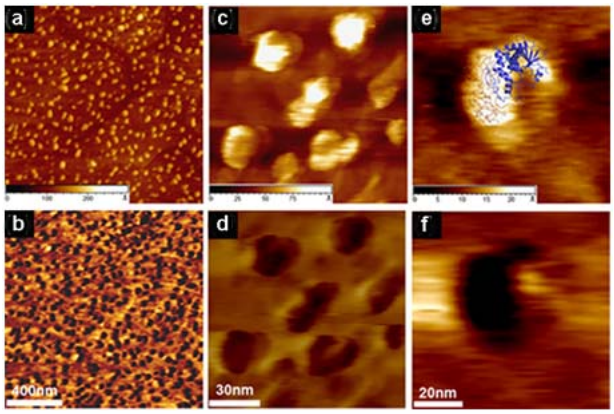

Figure 3.3 AFM topography and recognition of ricin molecules immobilized on Au (111) surface. Single molecule resolution was resolved with Au (111) terraces underneath clearly seen in large area (1300nm X 1300nm) topography image (a) but not seen in the corresponding recognition image (b). Small area images (c, d) show that the ricin protein on the surface fold up to form different shapes, some of which even clearly show two chains (e,f).

During scanning, the anti-ricin antibody functionalized tip interacted stronger with ricin immobilized to gold modified mica than with other parts of the surface. Therefore, in the recognition image, the ricin molecules are visualized as black dots. The scanned topography image was simultaneously recorded to provide further proof of detection. By using this method, one can not only detect the presence of the ricin, but also estimate the quantity of the ricin. Thus, 200 μL of a ricin solution (24 fg/mL) was kept on the modified gold surface for 30 min; then the chip was placed into the AFM system for scanning. Clear topography and recognition images were obtained (***Figure 3.3*** a-b, respectively). As can be seen in ***Figure 3.3*** *a*, each ricin molecule has a spherical shape (dimensions 20~30nm). By comparing the topographical and recognition images, we can easily identify which feature belonged to a ricin molecule: each bright spot in the

topographic image, if represents a ricin molecule, will result in a dark spot in the recognition image at the same location. Based on the obtained results, it was concluded that the detection method based on AFM can easily be achieved in the femto- or sub femto-level. Compared with other detection methods, this method is much easy and faster, and offers a significant advantage in both sensitivity and resolution.

In addition, ricin molecules were found to be approximately uniformly distributed on the surface, which was expected because of the uniformly close-packed NHS ester (succinimidyl active esters) layer on the Au (111) surface. Besides, the underneath Au (111) terraces were also clearly shown in the topographic image (***Figure 3.3*** a), suggesting a better immobilization method. On the other hand, the lacking of Au (111) terraces in the recognition image (***Figure 3.3*** b) unambiguously indicates that the recognition is specific. Molecular modeling[177] yielded a three-dimensional model that shows the overall folding of the ricin A-chain is fully conserved despite a few discrepancies due to the deletions and insertions between the secondary structures. However, a recent study[178] revealed that ligand binding will cause the ricin A-chain conformational change. We do found several different folded-up conformations of ricin molecules in our small area topographic image (***Figure 3.3*** c). ***Figure 3.3*** d is the recognition image corresponding to the ***Figure 3.3*** c, which is used to decide if the white dot in ***Figure 3.3*** c is indeed a ricin molecule. Among these different conformations, we focused on one single ricin molecule that has a 'native' conformation, with the A chain and B chain clearly resolved in the topographic image (***Figure 3.3*** e, recognition image in ***Figure 3.3*** f), matching the molecule structure (The A chain is shown in blue and the B chain in orange) very well. Therefore, we demonstrated that using the delicate AFM chemomechanical mapping with the tip modification and surface modification protocols, we are able to resolve not only single molecules but also

intra-molecule structures. However, the sizes (~20nm in diameter) measured by AFM, is about twice the size of about 10x10x10 nm crystal structure determined by X-ray crystallography[179]. This can be explained by tip broadening effect [180] and compression of the molecules due to the applied force[33].

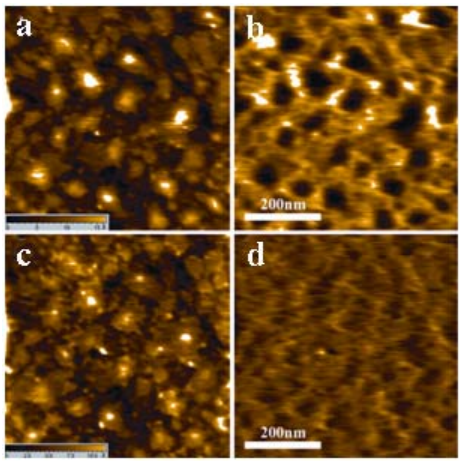

Figure 3.4 The blocking experiment. Topographic image before (a) and after (c) the blocking of antibodies on AFM tip and the corresponding recognition image before (b) and after (d) the blocking.

To further confirm the detection and recognition results, a control experiment was carried out adopting a flow-cell technique[134]. When the AFM system was stable, 200 μL of ricin protein (24 pg/mL) was injected into the liquid cell using an inlet syringe. Meanwhile, 200 μL of water in the liquid cell was drawn out by the outlet syringe to prevent the liquid in the cell from overflowing. The real time changes in the recognition image were monitored at the same location. It was observed that features were still clear in the topography image (***Figure 3.4***, a, c). However, the corresponding black dots fully disappeared in the recognition image (***Figure 3.4*** b, d). This observation can be explained by the binding of the injected ricin molecules to the anti-ricin Ab on the tip and blocking the interaction between the anti-ricine Ab and the ricin on the surface.

These results strongly support that the detection results (***Figure 3.3*** *a* and *b*) were reliable and indicate that AFM with recognition module is a powerful technique for toxin detection and bio-molecular interaction study.

3.3.3 Force Spectroscopy

Up to now, the main source of error in single molecule force microscopy came from the nonlinear elasticity during the stretching of the polymer crosslinker.[181] People tried to reduce it by adopting the different expression of force loading rate.[182] Currently, there were two main approaches widely adopted, nominal loading rate and instantaneous loading rate. [182,183] Since the later method can give out more accurate results, it was adopted here to carry out the force analysis. Some typical force curves were shown in ***Figure 3.5*** a. Further, we constructed the force histograms from about 3000 force-distance curves for each loading rate (as shown in ***Figure 3.5*** b) and applied Gaussian-fitting to identify the peak values, the most probable unbinding force (***Figure 3.5*** b). The corresponding instantaneous loading rates from the statistical analysis (***Figure 3.5*** d) were used for drawing the correct kinetic information for the force studies. The corresponding disruptive forces were measured to range from 25 pN to 80 pN, which is quite reasonable for the unbinding force between antibody and antigen.[146] The unbinding forces were in linear relation with the loading rates in the logarithmic scale (***Figure 3.5*** c), which indicates that the binding complex only went through one high-energy transition state before dissociation.[109]

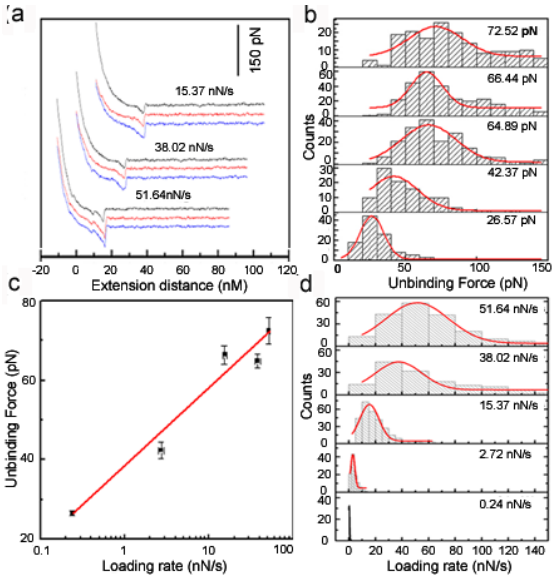

Figure 3.5 The dynamic force measurement. a) Typical AFM retraction curves at instantaneous loading rate of 15.37 nN/s, 38.02 nN/s, and 51.64 nN/s. b) Most probable unbinding force histogram and their Gaussian fitting curves for 5 different force loading rates. c) Most probable unbinding force at different instantaneous loading rate. The linearity fits the one-barrier dissociation model well. d) The corresponding instantaneous loading rate histogram and their Gaussian fitting curves.

To get barrier length, the relation between the unbinding force and logarithmic loading rate was fit by a line according to ***Equation 3.1*** [184], shown in ***Figure 3.5*** c.

$$F^* = \frac{kT}{x}\ln r - \frac{kT}{x}\ln(k_d(0)\frac{kT}{x}) \qquad \textbf{Equation 3.1}$$

where x is the barrier length, kT is the thermal energy, F^* is the most probable rupture force, and r is the force loading rate. The slope of the fit line was determined to be around 8.54 pN. Therefore the barrier length x was calculated from this slope to be 0.46 nm according to $x = kT/s$ where s is the slope of the best-fit line. This is a bit bigger than most of the reported

barrier length of 1.5~3 Å.[185,186] This could due to several reasons: Firstly, because of the nonlinear elasticity and limited force sensitivity, the value could have about 10% error.[181] Secondly, the barrier length would vary with the size of hydrophobic ricin molecule (10~20 nm). The dissociation rate at zero force $k_d(0)$ estimated from the intercept of the fit line in ***Figure 3.5*** c, $k_d(0)=1.43\times10^{-3}$ s^{-1}, was quite reasonable for antibody-antigen complex. However, it would also carry with errors originating from the slope fitting process, nonlinear character of the cross-linker and so on.[187,188] According to the simulation studies, the error could be several folds.[188]

Following these previous work,[116] the momentum-based approach of Jarzynski equality was adopted to calculate the unbinding free energy. Since the free energy calculation is independent on the force loading rate, only 20 force curves at nominal force loading rate of 450 nN/s were used for free energy analysis shown in ***Figure 3.6*** a. Certainly, the quantity is far away from the request for the high accuracy analysis. And the quantity is more, the results of free analysis would be better. The amount of force-distance curves used to do free-energy analysis is always around 50 in experimental reports [115,117,189,190]. However, most of these reported data are focused in the DNA or protein folding experiment[117,189-192]. Comparing to these folding experiments, the system in our experiment is a little bit complex because of the included cross-linker, PEG, which increase not only the event probability, but also the heterogeneity of F-D curves. Hence, the amount of F-D curves in energy analysis is less than that reported in the folding-unfolding experiment. Although the amount of curve is limited, the accuracy of the free energy analysis is still acceptable. As stated by Ritor,[115] it was showed that the deviation between the results from 20 and 50 force curves is only about 5 K_BT.[193]

After the F-D curves were smoothed and aligned[117], the section was abstract out from 538 nm to 517 nm for the pulling rate of 450 nN/s. Whereafter, the free energy was analyzed by the

momentum-based method, shown in ***Figure 3.6***. The average force in ***Figure 3.6*** b is very close to the value estimated by the histogram at the same loading rate. After the free energy profile sharply increased, there was still somehow increment, around 8 K_BT and 15 K_BT, which is mainly due to the noise of the whole system. It was shown that the unbinding free energy value G_{JF} from Jarzynski equality was 86 K_BT.

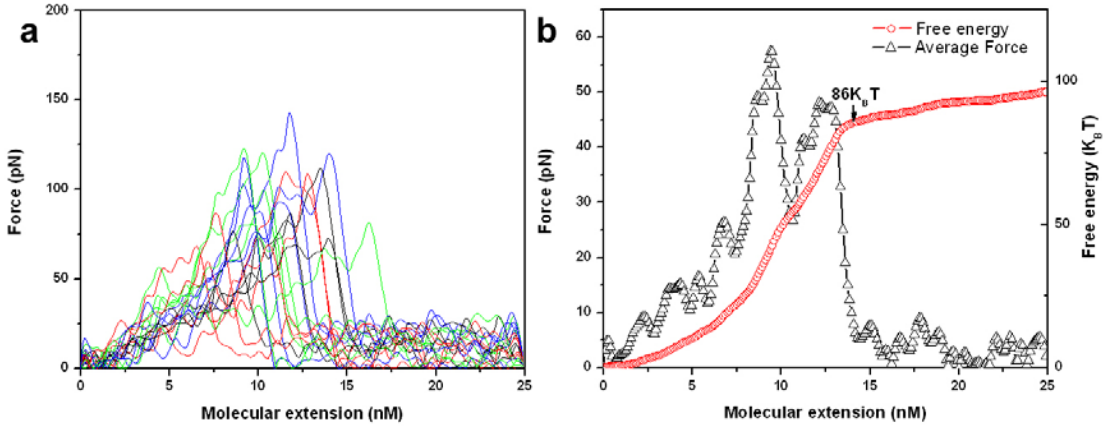

Figure 3.6 Free energy calculation. a) Alignment of 25 pieces of force distance curves at nominal force loading rate of 450 nN/s. b) Mean unbinding force and free energy calculated from Jarzynski's equality.

3.5 Conclusions

A new and efficient protocol for tip functionalization for AFM has been developed using a PEG derivative containing a thiol and azide end group. This heterofunctional linker can be employed for SAM formation on a gold modified tip and the azides of the resulting SAM can be applied for the immobilization of an anti-ricin Ab modified by alkynes using a click reaction. The high efficiency, mild reaction condition, and simple operation of the click reaction greatly simplified the tip modification process. Furthermore, ricin can be immobilized on a gold-coated

mica substrate by employing another novel bifuntional compound composed of an *N*-hydroxysuccinimidyl ester and a thioctic acid moiety. The thiotic acid moiety of this reagent binds strongly with a gold-coated mica substrate and the active esters of the resulting surface can then be reacted with amines of the protein. Using the recognition approach, qualitative and quantitative information can be easily obtained from the images attained by the AFM system. Compared with other detection methods, this approach has significantly higher sensitivity (sub-femtogram level), a faster responses, and easier operation protocol. The detection results were further confirmed by blocking experiment. Therefore, it was expected this AFM based technique to be an attractive method for single molecule toxin detection as well as for studies of molecular recognition events.

On the other hand, nanoscale variations of single molecule structure and intra-molecular structure of the different fold-up conformations as well as A- and B- chains of ricin protein molecule have been resolved. Further, AFM force spectroscopy study shows that the binding dissociation process agrees with the prediction of one-barrier dissociation model and free energy from Jarzynski equality was about 86 K_BT.

CHAPTER 4

SINGLE MOLEULE INTERACTION STUDY BETWEEN CANCER TARGET EPHA2 AND ITS LIGANDS

4.1 Introduction

Both single molecule force spectroscopy and recognition imaging were applied to understand the interactions and binding kinetics between the candidate anti-cancer peptide and the EphA2 receptor, a novel target in cancer therapies. The membrane receptor EphA2, a member of the Eph (erythropoietin-producing hepatocellular) family of receptor tyrosine kinases, is known to regulate multiple cellular signaling pathways and to influence cell attachment, motility and survival[194-197]. Recent data indicate overexpression of Eph2 in many cancers including ovarian, breast, colon, brain, and pancreatic[194-197] and associate elevated levels of this protein with cancer metastatic potential. Therefore, EphA2 signaling is a promising novel target for cancer treatment.[194-196] However, there is no highly selective inhibitor of EphA2 in clinical applications. This work is an initial step to develop a specific, peptide-drug inhibitor for EphA2. It was shown earlier that previously identified 12-amino acid peptide,[198] termed YSA (YSAYPDSVPMMS), targets nanoparticles directly to cancer cells expressing the EphA2 receptor, indicating that YSA may be used to specifically deliver anticancer drugs in order to increased drug efficacy.[199,200] Recently, it was demonstrated that the YSA peptide is useful in targeted delivery of the therapeutic, gene-specific siRNA to cancer cells by using peptide-functionalized nanogels, and subsequent sensitization of cancer cells to taxane chemotherapy.[201] It was also shown that YSA alone partially inhibits tumor growth in a xenograft tumor model.

Thus, YSA presents itself as a very promising candidate for anticancer therapy. However, the molecular basis of YSA and EphA2 receptor interactions, and the YSA anticancer mechanism are largely unknown. While the initial characterization of YSA indicated that it mimics the activity of ephrinA1[198], the natural ligand of EphA2, it was determined that YSA exerts downstream signaling effects different from the natural ephrinA1 ligand. These results prompted to further investigate differences between binding of YSA and ephrinA1 to EphA2, in order to develop an YSA-based anticancer drug specifically targeting EphA2.

Here, the following aspects of their interactions were analyzed: 1) competitiveness of YSA and ephrinA1 in binding to EphA2; 2) binding kinetics of YSA and ephrinA1 to EphA2; 3) importance of the N- and C-terminal parts of YSA peptide for its binding to EphA2; and 4) differences in binding of monomeric and dimeric forms of ephrinA1 to the EphA2 receptor. The data obtained in this study can improve the understanding of similarities and differences of interactions in ephrinA1-EphA2 and YSA-EphA2 complexes, and provide a basis for future work on rational design of high-affinity peptide ligand for EphA2 in anti-cancer therapies.

4.2 Experiments

4.2.1 Materials

Receptor. EphA2 (R&D Systems, Inc.). The protein is consisted of the entire extracellular domain of human EphA2 (residues 25-534), and C-terminal six-residue His tag.

Ligands. EphrinA1-Fc dimer (R&D Systems, Inc.). Since two units of EphrinA1-Fc is connected by disulfide bonds between the two Fc fragments, EphrinA1-Fc monomer was prepared by reducing the disulfide bonds between the two Fc fragments of the EphrinA1-Fc

dimer. YSA (Biomatik Corporation, Sequence: YSAYPDSVPMMS), YSA with cysteine residue at C-terminus (Biomatik Corporation, Sequence: YSAYPDSVPMMS-Cys).

Other reagents. FITC (fluorescein isothiocyanate, Sigma-Aldrich Inc.); Regenerated cellulose dialysis membrane (MWCO=3500) (Membrane Filtration Products, Inc.); Crosslinkers: NHS-$(PEG)_{12}$-Maleimide (Thermo Fisher Scientific Inc.); 3-Triethoxysilylpropylamine (APTE, Sigma-Aldrich Inc.); 3-Triethoxysilyl-1-propanethiol (MPTE, Sigma-Aldrich Inc.); Dithiobis-succinimidylpropionate (DTSP, Fluka); Amino-nitrilotriacetic Acid (ANTA, Fluka); CS-10 silicon AFM probe (Nanoscience Instruments); Gold (99.999%, Kurt J. Lesker Company); Phosphate Buffer Saline (PBS, pH 7.4, w/o Mg^{+2} or Ca^{+}, Cellgro by Mediatech Inc.), DTT (Dithiothreitol) (Acros Organics, Morris Plains, NJ, USA), Iodoacetamide (Sigma-Aldrich Inc.). Chemicals were used without further purification.

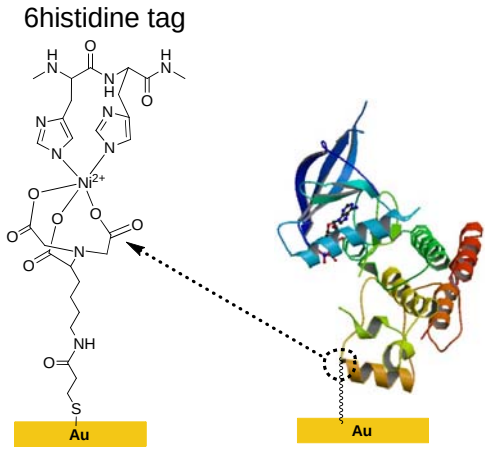

Figure 4.1 Optimized attachment of His-tagged Epha2 with specific orientation on gold surface.

4.2.2 Methods

Preparation of the ephrinA1-Fc monomer. To generate a monomeric form of ephrinA1 previous procedure was followed,[202] in which an ephrinA1-Fc homodimer (ephrinA1-Fc-Fc-

ephrinA1) was transformed to a monomer (ephrinA1-Fc) by using DTT and Iodoacetamide to reduce the disulfide bonds between the two Fc fragments.

Immobilization of the EphA2 protein on the Au substrate. Through C-terminal His-tag (six histidine residues) and Ni^{+2}–NTA (nitrylo-triacetic acid) shown in ***Figure 4.1***, the procedure for site-specific immobilization of EphA2 receptor was optimized on the Au surface. DTSP-ANTA linker was synthesized to conjugate with the EphA2 molecules so that the carried disulfide moiety of EphA2 can attach to the annealed Au surface. In detail, DSP-ANTA (1mg/ml, 10μl) and Ni^{2+} solution (40 mM, 1μl) were mixed first for 1~2 hour, then 200 μl of EphA2 in PBS solution (100 μg/ml) was added into the mixture and kept for 4~5 hours at 4 ºC. Next, the mixture was transferred into the dialysis vial with a regenerated cellulose membrane (MSCO=3500) against the PBS buffer with 1 mM Ni^{2+} for 24 h at 4 ºC. The obtained conjugated EphA2 was aliquot and stored at -20 ºC. The conjugated EphA2 was immobilized on the annealed (hydrogen flame) Au surface through the disulfide group of the DTSP-ANTA linker. After incubation for 4 hours at 4 ºC (200 μL of conjugated EphA2 in PBS solution, 10 μg/mL), the modified surface was rinsed several times with PBS buffer. This method allowed us to obtain a stable monolayer of the protein on the surface and a site-specific protein attachment, which increases the chance of binding since the binding site of the receptor will remain exposed to the ligand during the AFM scanning. The sizes of molecules of about 20 nm on the topography image (***Figure 4.2*** c) were consistent with the approximate size of the ectodomain of EphA2 that we estimated from the structural modeling. This method resulted in much better protein monolayer compared to the one obtained by using the immobilization protocol applied earlier, in which first the DTSP-ANTA was deposited on the annealed Au surface and next the EphA2 protein was immobilized on the DTSP-ANTA monolayer (***Figure 4.2*** a and b). This approach

also decreased the possibility of interfering interactions between the tip and the DTSP-ANTA molecules on the surface that remained not conjugated to EphA2.

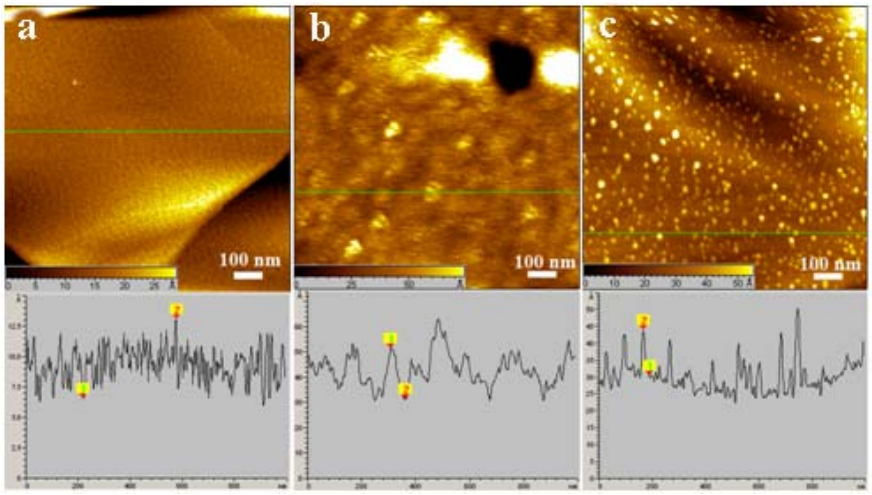

Figure 4.2 The profile of several functionalized surface. (a) Topographical image of the gold surface modified with DTSP-ANTA; (b) Topographical image after addition of EphA2 to the previously DTSP-ANTA functionalized surface; (c) Topographical image of the DTSP-ANTA-EphA2 complex attached the gold surface.

Functionalization of the AFM tip with ligands. The scheme of the AFM cantilevers functionalization was shown in ***Figure 4.3*** a. First the magnetically coated tips were modified with -NH_2 or -SH groups by using APTES or MPTE organosilanes, respectively, under the vapor phase for 20 min at 1 torr. After sonic cleaning in hexane, the modified tips were immersed in NHS-$(PEG)_{12}$-Maleimide in DMSO solution (concentration 20 mM) for 2 hours at r.t., following by rinsing with DI water. Finally, the tips were transferred into biological sample solution (YSA, YSA-Cys, ephrinA1 dimer, or ephrinA1 monomer, concentration 1 mM) for another 12 h at 4 ºC. After rinsing with DI water several times the functionalized tips were stored in PBS solution, at 4 ºC. The use of bi-functionalized NHS-$(PEG)_{12}$-Maleimide linker allowed us for the site-specific

attachment of the YSA peptide to an AFM tip, either by the N-terminus of YSA or the C-terminal cysteine residue of YSA-Cys. For the connection of YSA through its N-terminus, the AFM tip was functionalized with -SH group, coupled with maleimide group of linker, and the remaining succinic acid group of linker (NHS) can react with -NH_2 group in the peptide's N-terminus (there is only one amino group available at N-terminus of YSA). For connection of YSA by the C-terminal cysteine (-SH) the tip was functionalized with -NH_2 group which reacted with succinic acid group of the linker, and linker's maleimide group reacted with the -SH group of the C-terminal cysteine of YSA (there is no other –SH group in the peptide sequence). The attachment of the ephrinA1-Fc dimer and monomer was performed through protein surface lysine residue and was not site-specific.

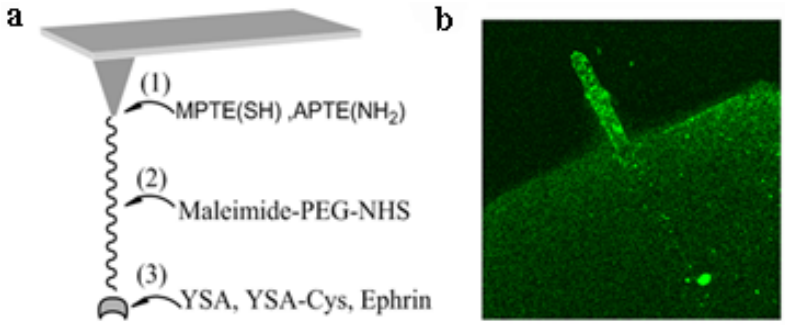

Figure 4.3 The tip modification procedure and its proof. a) Tip functionalization scheme for YSA, YSA-Cys, or Ephrin. b) Fluorescence image of the AFM tip functionalized with YSA-Cys peptide and stained with FITC demonstrating that the peptide was attached to the AFM tip.

To verify attachment of a ligand to the AFM tip, the FITC (fluorescein isothiocyanate) was applied to stain the YSA-Cys functionalized tip. The FITC dye can react with the -NH_2 group of the YSA peptide resulting in tip fluorescence if the YSA was attached to the tip. The YSA-Cys modified tips were immersed in the FITC solution in DMF (1 mg/mL) for 12 h at 4 ºC. After rinsing with water to remove a physically adsorbed FITC dye, the tips were imaged under

water by confocal microscopy (488 nm Green Argon laser (Eclipse, TE 3000, Nikon). As shown in ***Figure 4.3*** b, green fluorescence of FITC indicates that the ligand is attached to the AFM tip.

AFM experimental setup. (the same apparatus and similar operation method as Chapter 3)

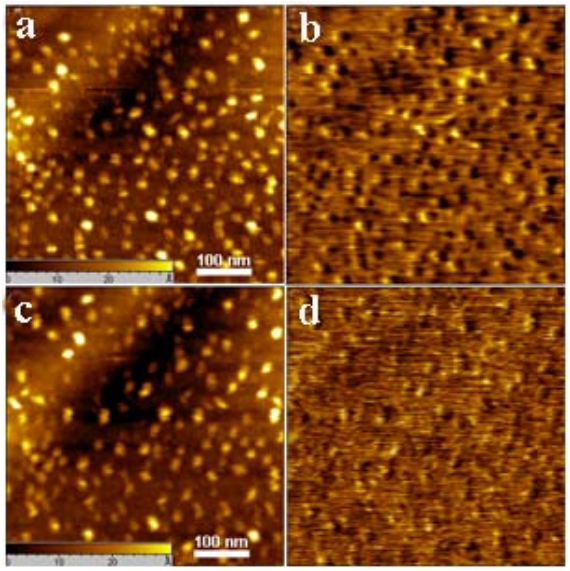

Figure 4.4 The AFM recognition imaging of the YSA-EphA2 interaction. The YSA peptide was tethered by the PEG linker to the AFM tip. The EphA2 receptor was immobilized on the surface through a C-terminal His-tag. a) topography and b) recognition images obtained with the YSA-modified tip, c) topography and d) recognition images obtained with the bare tip.

Control test for non-specific interactions of the AFM tip. For an accurate recognition imaging, the non-specific interactions between the bare, unmodified AFM tip and the receptor molecules on the substrate should be minimal. To check whether the nonspecific interaction of the unmodified tip with the receptor are negligible, the topography and recognition images of EphA2 immobilized on the surface were collected, using the AFM tip functionalized with YSA-Cys (***Figure 4.4*** a, b) and compared them with images obtained by using the unmodified tip (***Figure 4.4*** c, d). As shown in ***Figure 4.4*** c and d, the bare tip differentiated shapes of the

EphA2 molecules in topography images (***Figure 4.4*** c, white spots) but it didn't interact with the receptor (***Figure 4.4*** d, lack of dark interaction spots). In contrast, the tip modified with YSA-Cys not only differentiated the topography of the receptors (***Figure 4.4 a***, white spots), but also interacted with the EphA2 molecules (***Figure 4.4*** b, dark interaction spots).

4.2.3 Data collection and analysis

Force spectroscopy - evaluation of a dissociation rate constant k_{off}. The dynamic force spectroscopy was applied to determine the dissociation rate constant k_{off}.[203] The force spectroscopy data were collected under several different nominal force loading rates (three loading rates for each ligand, at 4000, 400, and 40 nN/s). For each loading rate, 1000 force-displacement curves were recorded at room temperature, at different positions on a sample that corresponded to receptor molecules of the topography images. The same force spectroscopy experiments were carried out for all four ligands attached to the AFM tips: YSA, YSA-Cys, ephrinA1-Fc monomer, and ephrinA1-Fc dimer. For each force-distance curve, the apparent loading rate was determined by calculating the slope of the curve just before rupture of the complex[188]. We applied linear fit of the rupture force, F_R, versus apparent loading rates, r, according to the Bell model[109,204], ***Equation 4.1***, to obtain the rupture force at zero loading rate (an intercept of the linear fit to ***Equation 4.1***), F_0, and the width of the interaction well, x (a slope of the linear fit to ***Equation 4.1***). The dissociation rate constant, k_{off}, was calculated from ***Equation 4.2***, where k is the Boltzmann constant and T is temperature.

$$F_R = \frac{kT}{x}\ln(r) + \frac{kT}{x}\ln\left(\frac{x}{k_{off}\cdot kT}\right) \qquad \textbf{Equation 4.1}$$

$$\ln(r) \to 0 : F_0 = \frac{kT}{x}\ln\left(\frac{x}{k_{off}\cdot kT}\right) \qquad k_{off} = \frac{x}{kT}\exp\left(-\frac{F_0\cdot x}{kT}\right) \qquad \textbf{Equation 4.2}$$

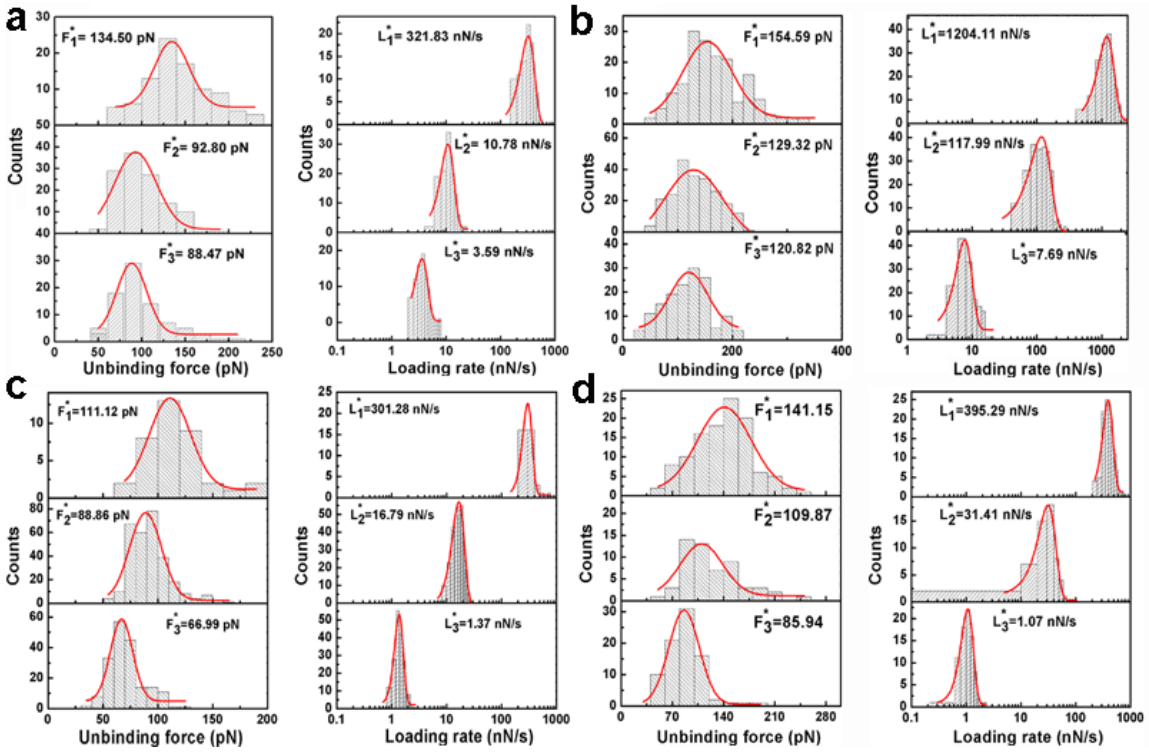

Figure 4.5 Histograms of rupture forces (left) and corresponding apparent loading rates (right) for EphA2-ligand complexes. For ligands: (a) ephrinA1-Fc-monomer, (b) ephrinA1-Fc-dimer, (c YSA-Cys, and d) YSA. For each ligand (a, b, c, d), there are three subpanels, corresponding to three different nominal loading rates (nN/s) 400 (top), 40 (middle), 4 (bottom). Histograms were fitted with Gaussian function and the most possible values of these fitting were labeled on the figures.

The average life-time of a receptor-ligand bond was calculated as $\tau_0 = k_{off}^{-1}$. Because of deviations of the data from linearity, the most probable apparent loading rates and the corresponding most probable rupture forces were selected. In detail, the histograms of each apparent loading rate were built (***Figure 4.5***). Each of the three histograms was fitted with the Gaussian function and the loading rates within +/-σ value of each Gaussian were selected (approximately half of the Gaussian width, centered at the Gaussian's mean). Next, for each of

the selected loading rates, the histograms of rupture forces were obtained and applied by the same selection procedure as for the loading rates to choose the final sets of the force versus loading rate data that were then used for the linear fit to Bell model. The histograms for loading rates and rupture forces for all the ligands can be found in ***Figure 4.5*** and the linear fitting curves of the rupture force versus apparent loading rates were shown in ***Figure 4.6***.

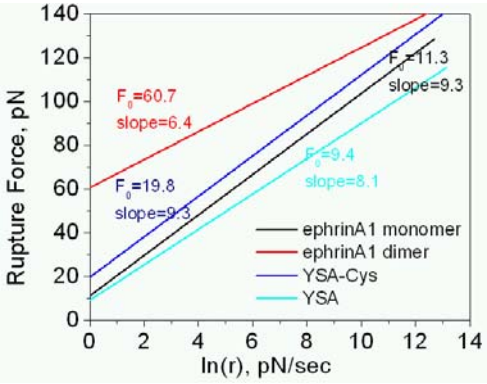

Figure 4.6 Results of dynamic force spectroscopy for EphA2-ligand complexes. Linear fit of the rupture forces versus natural logarithm of force loading rates for EphA2-ligand complexes; ligands: ephrinA1-Fc monomer, black; ephrinA1-Fc dimer, red; YSA-Cys, blue; YSA, cyan.

Evaluation of the association rate constant k_{on}. To calculate the receptor-ligand association rate constant k_{on}, the reported method by Lee et al. [178] was used, which is based on a competitive inhibition of the receptor's binding site by the ligand attached to the tip and the same ligand in the solution surrounding the immobilized receptor. In these experiments, the time-lapsed AFM topography and recognition images of the interactions were recorded between the immobilized receptor and the ligand on a tip, before and after addition of the same ligands to the solution in fluid cell. These images were used to calculate time-dependent changes of the number of bound receptor-ligand molecules after addition of the ligand to the solution, for a chosen

500x500 nm area of the receptor sample. The k_{on} was then calculated from a kinetic differential equation, ***Equation 4.3***, describing the process:

$$Ligand\ (L) + Receptor(R) <\frac{kon}{koff}> Complex\ (C)$$

$$\frac{dC}{dt} = k_{on} \cdot R \cdot L - k_{off} C \qquad \textbf{Equation 4.3}$$

Where R, L, and C were concentrations of the unbound receptor, unbound ligand, and receptor-ligand complex respectively. Because of excess of the ligands in solution compared to the amount of the receptor, it was assumed that L is constant and equal the known initial concentration of the ligand added to the solution, L_0. By replacing $R = R_T - C$, where R_T is a known total concentration of receptors (bound and unbound) on the surface we obtain ***Equation 4.4***:

$$\frac{dC}{dt} = k_{on} \cdot (R_T - C) \cdot L_0 - k_{off} C \qquad \textbf{Equation 4.4}$$

with a boundary condition of $C(t=0) = 0$ (due to the initial lack of the ligand in solution) and the solution, ***Equation 4.5***:

$$C(t) = \frac{k_{on} L_0 R_T}{k_{on} L_0 + k_{off}} \left[1 - \exp((-k_{on} L_0 + k_{off}) \cdot t)\right] \qquad \textbf{Equation 4.5}$$

At the saturation state (t⟶ ∞), ***Equation 4.6*** and ***Equation 4.7*** were obtained:

$$C(\infty) = \frac{k_{on} L_0 R_T}{k_{on} L_0 + k_{off}} \qquad \textbf{Equation 4.6}$$

$$k_{on} = \frac{C(\infty) k_{off}}{L_0 (R_T - C(\infty))} \qquad \textbf{Equation 4.7}$$

The concentration of a bound receptor-ligand at equilibrium (time⟶ ∞), $C(\infty)$, was determined by the exponential fit of the dependence of the bound receptor-ligand concentration,

$C(t)$, versus time, ***Equation 4.5***. For the k_{off} the values was obtained from force spectroscopy (***Table 4.1***). The detailed data for the k_{on} calculation for each ligand can be found in ***Table 4.2***. The exponentially fitted curves of $C(t)$ versus time are shown in ***Figure 4.7***. The equilibrium dissociation constant, K_D, is calculated as k_{off}/k_{on}. The binding energy is calculated as $E = \boldsymbol{R}Tln(K_D)$, where $\boldsymbol{R}$ and T are the gas constant and temperature, respectively.

Table 4.1 Kinetic and thermodynamic data. They were obtained from the AFM recognition imaging and force measurements for binding of the EphA2 receptor with its ligands, ephrinA1-Fc dimer, ephrinA1-Fc monomer, YSA-Cys, and YSA.

	ephrinA1-Fc Dimer	**ephrinA1-Fc Monomer**	**YSA-CYS**	**YSA**
$\mathbf{k_{off}}$ [a] (s^{-1})	$1.7*10^{-4}$ (1.0-2.9)[g]	$3.6*10^{-4}$	$1.5*10^{-2}$ (0.8-2.7)[g]	$5.8*10^{-2}$ (4.0-8.6)[g]
$\mathbf{k_{on}}$ [b] ($s^{-1}M^{-1}$)	$6.0*10^{4}$ (1.3)[g]	$2.6*10^{4}$ (1.5-6.4)[g]	$1.9*10^{3}$ (1.6-2.3)[g]	$1.9*10^{3}$
x [c] (Å)	5.7 (0.2)[h]	5.9 (0.2)[h]	4.3 (0.2)[h]	4.9 (0.2)[h]
$\boldsymbol{\tau_0}$ [d] (S)	5882	2778	67	17
$\mathbf{K_D}$ [e] (M)	$2.8*10^{-9}$	$1.4*10^{-8}$	$7.9*10^{-6}$	$3.1*10^{-5}$
E [f] (kcal/mol)	11.6	10.8	7.0	6.2

[a] k_{off} – dissociation rate constant, [b] k_{on}– association rate constant, [c] x – width of the interaction well, [d] τ_0 – average life-time of a receptor-ligand complex, [e] K_D – equilibrium dissociation constant , [f] E – ligand-receptor binding energy. In parentheses are experimental errors: [h] standard deviation, [g] minimal and maximal value.

Estimation of the sizes of the EphA2 ectodomain and the ephrinA1-Fc dimer. The extracellular domain of the EphA2 protein used in this study consists of the ligand binding domain, the cysteine-rich fragment, and two fibronectin III repeats. The experimental structure of the ligand binding domain is known.[205] For the remaining domains threading-based structure prediction was applied using the I-TASSER[206] method and the LOMETS server[207]. The approximate size of the ectodomain was obtained by adding up the sizes of all four subdomains (from N- to C-terminus) and was evaluated to be about 20 nm. To estimate the maximum separation of the two binding loops (one loop in each ephrinA1 monomer) of the ephrinA1-Fc

dimer (ephrinA1-Fc-Fc-ephrinA1), the sizes of experimental structure of the two Fc domains (about 5.5 nm from N- to C-terminus per domain), and the distance from C-terminus to the binding loop in the experimental structure of ephrinA1 for each of two fragments (about 2.2 nm per protein) were summed with the size of about 15 nm. This gives us an approximate maximum distance between the two receptor molecules that could be bound simultaneously by two subunits of ephrinA1-Fc dimer.

Table 4.2 Experimental data used for the calculation of association binding constant, k_{on}, for binding between EphA2 and the ligands.

	ephrinA1-Fc Dimer		**ephrinA1-Fc Monomer**		**YSA-CYS**	
Time-lapse Blocking Data	**t[a] sec**	**C_t[b]**	**t[a] sec**	**C_t[b]**	**t[a] sec**	**C_t[b]**
	0	0	0	0	0	0
	720	26	600	15	524	52
	2520	36	1200	26	1093	59
	2880	46	1800	30	1675	72
	3240	51	3600	40	2239	78
	4680	56	5400	56	2920	78
			7800	61		
R_T [c]	60[f]		72[f]		86[f]	
	$17.65*10^{-11}$ M[g]		$21.16*10^{-11}$ M[g]		$25.28*10^{-11}$ M[g]	
C_∞ [d]	56.97[f]		63.60[f]		76.88[f]	
	$16.75*10^{-11}$ M[g]		$18.69*10^{-11}$ M[g]		$22.60*10^{-11}$ M[g]	
L_0 [e]	$53.4*10^{-9}$ M[g]		$106.8*10^{-9}$ M[g]		$6.9*10^{-5}$ M[g]	

[a] Time after adding of the blocking ligand to the EphA2 receptor immobilized on the surface, sec, [b] C_t – number of EphA2 molecules blocked with the ligand after time *t*,

[c] R_T – total number of EphA2 molecules in the analyzed AFM image,

[d] C_∞- number of EphA2 molecules blocked with the ligand at equilibrium, after time $t->\infty$,

[e] L_0 – initial concentration of ligand, mol/liter , [f] amounts of reagents expressed in number of molecules in the analyzed AFM image, [g] amounts expressed in molar concentration, mol/liter.

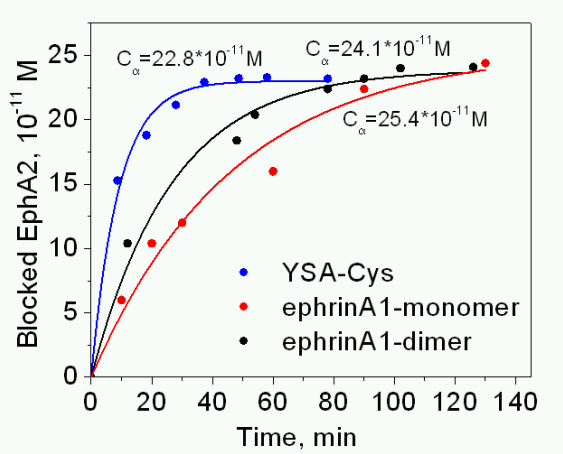

Figure 4.7 Results of EphA2 blocking with ligands. Exponential fit of the dependence of the concentration of blocked EphA2 (bound EphA2-ligand complexes), $C(t)$, versus time after addition of ligand to the fluid cell; ligands: YSA-Cys, blue; ephrinA1-Fc monomer, red; ephrinA1-Fc dimer, black. C_∞ denotes the concentration of blocked receptor at equilibrium (time -> ∞).

4.3 Results and discussions

YSA and ephrinA1 bind competitively to EphA2. It has been suggested, based on a macroscopic competitive binding experiment that the YSA peptide mimics binding of ephrinA1 to EphA2, the receptor's natural ligand[198], i.e. both ligands bind to a similar binding region of the receptor. To verify these earlier results at the single-molecule level the AFM blocking experiments were performed, using ephrinA1-Fc dimer as blocking ligand. In this experiment first the topography and recognition images of the unblocked EphA2 were collected, by using the YSA-Cys modified AFM tip. Next, the ephrinA1-Fc dimer solution (concentration 10 μg/mL) was added to the liquid cell which can bind to EphA2. Time-lapsed topography and recognition

images of the same surface fragment were collected with the YSA-Cys-modified tip. If ephrinA1 and YSA bind competitively to EphA2, it was supposed to observe a decreasing with time number of interaction sites of YSA with EphA2, as a result of an increasing number of EphA2 binding sites being occupied by ephrinA1 from the solution. It is evident from the recognition images in ***Figure 4.8*** c, d that the number on YSA and EphA2 interactions (dark spots on the recognition images, ***Figure 4.8*** c, d) decreases with post-blocking time, indicating that ephrinA1 and YSA compete for the binding site on EphA2. The simultaneously recorded topography images show that number of the receptor molecules remains almost unchanged during the experiment (***Figure 4.8*** a, c, white spots). In the contrary, it can be noticed that second bright spot is next to the marked EphA2 receptor that likely corresponds to the ephrinA1 molecule bound to the EphA2 receptor after ephrinA1 is added.

A quantitative representation of these results was shown in ***Figure 4.8*** e, where white bars represent a histogram of YSA and EphA2 interactions forces before blocking and the grey bars represent a histogram of YSA and EphA2 interaction forces 3 hours after blocking of EphA2 with ephrinA1. The histograms were obtained by measuring the rupture forces between the interacting YSA-Cys (on a tip) and EphA2 (on the surface) before and after blocking of the receptor with ephrinA1. It is evident from these histograms that after blocking of EphA2 with ephrinA1, number of interactions between YSA and EphA2 decreases indicating that YSA binds in a similar region of the EphA2 molecule as ephrinA1. This result confirms at a single-molecule level observations of Koolpe and his coworkers that indicated competitive binding of YSA and ephrinA1 to Epha2 in macroscopic studies[198]. This finding is important in terms of further improvement of peptide inhibitor of EphA2, as the crystal structure of EphA2 and ephrinA1 is

known[205] and the binding interface of this complex could be used as a source of structural data for the peptide re-design to improve its binding and specificity to EphA2.

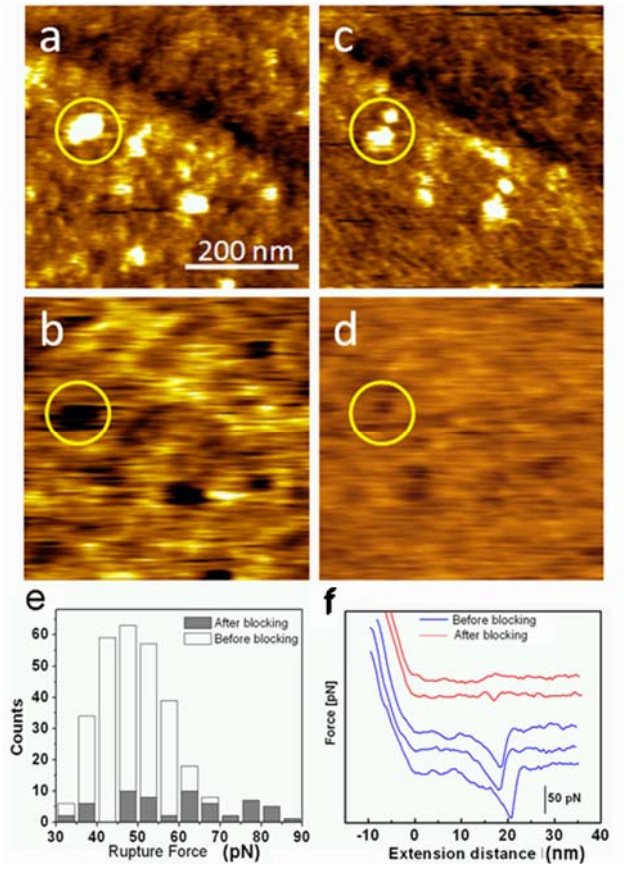

Figure 4.8 The AFM demonstration of the competitive binding of the YSA and ephrinA1 ligands to EphA2. a) topography and b) recognition images obtained with the YSA-modified tip before blocking of EphA2 with the soluble ephrinA1, c) topography and d) recognition images obtained with the YSA-modified tip after 3h post blocking of EphA2 with the soluble ephrinA1. The yellow circle shows an example of competitive binding the YSA and ephrinA1 ligands to EphA2. e) A histogram of rupture (unbinding) forces obtained from AFM force-distance curves (f) of the YSA-EphA2 interactions before and after blocking of EphA2 with the soluble ephrinA1.

Identification of the force peak representing the specific ligand-protein binding. Differentiation between the nonspecific tip-ligand and specific protein-ligand interaction is often difficult. Given the length of the PEG cross-linker applied in our study (about 6 nm) and the size of the EphA2 ectodomain estimated to be at the maximum ~20 nm, it was supposed that the rupture events with stretching distance in the range of 6 to 26 nm (the distances between the length of the PEG linker and the sum of lengths of the PEG linker and the EphA2 receptor) would be counted here as specific interactions. This rule was used to select the relevant force curves in all the force spectroscopy experiments probing the ligand-EphA2 binding. Additional identification of the position of the specific interaction force peak on the force-distance curves was done based on the previously described blocking experiment. ***Figure 4.8*** f showed the typical force-distance curves of YSA-Cys (on a tip) and EphA2 (on the surface) interactions measured before and after blocking of EphA2 with ephrinA1 in solution. The force peak present on force-distance curves before blocking (***Figure 4.8*** e, blue curves) disappeared after ephrinA1 inhibits binding between YSA and EphA2 (***Figure 4.8*** e, red curves), indicating that this force peak represents specific interactions of YSA with EphA2.

Binding force and kinetics of the ligands with the EphA2 receptor. The strength and kinetics of binding between various ligands and EphA2 were analyzed, including a) YSA-Cys, b) YSA, c) ephrinA1-Fc monomer, and d) ephrinA1-Fc dimer. A pair of peptide ligands (YSA-Cys and YSA) was used to investigate which part of the peptide is more essential for its binding to EphA2. The ephrinA1-Fc monomer and ephrinA1-Fc dimer were used to compare binding of the mono- and bivalent ephrinA1 ligands to EphA2. In the following sections the binding affinities and kinetics of these ligands to EphA2 were compared. The kinetic rate constants, k_{off} and k_{on}, the equilibrium dissociation constant, K_D, and the binding affinities were calculated based on the

AFM force spectroscopy and imaging experiments, as described in Materials and Methods, *Data collection and analysis.*

Evaluation of the binding strength between different parts of the YSA peptide and EphA2. The molecular basis of the YSA and EphA2 binding are largely unknown. Our and other's[198] results suggest that the YSA binds in the similar binding site as the ephrinA1 ligand. In another study, the known crystal structure of EphA2-ephrinA1 complex was used to build the homology model of the EphA2-YSA complex assuming the same binding sites for ephrinA1 and YSA, and simulated the interactions between the receptor and the peptide by using all-atom molecular dynamics. These simulations indicated that the N-terminal tyrosine residues in the positions 1 and 4 in the YSA peptide sequence (**Y**SA**Y**PDSVPMMS) play important role in binding to the EphA2 receptor. a simple approach was used to test which end of the peptide is more essential for its binding to EphA2, by measuring the peptide-receptor interaction for the YSA peptide attached in two different ways to the AFM tip, 1) by the N-terminus, limiting accessibility of the N-terminal end of the peptide during its binding to EphA2-this type of connection we called here YSA, and 2) by C-terminal cysteine added to the peptide sequence to enable site-specific attachment of the peptide to the tip by its C-terminal end; this attachment limits accessibility of the C-terminal end of the peptide to the binding site of EphA2 and it was called here YSA-Cys. The determined value of k_{off} for YSA-Cys peptide ($1.5*10^{-4}$ s^{-1}) is smaller than that for the YSA peptide ($5.8*10^{-2}$ s^{-1}) indicating a longer average lifetime of peptide-ligand complex for YSA-Cys than for YSA (67 seconds for YSA-Cys compared to 17 seconds for YSA) (***Table 4.1***). This suggests that the residues closer to the N-terminus of the YSA peptide are stronger involved in the YSA-EphA2 interactions. This observation is consistent with conclusions from the previous simulation studies, indicating importance of N-terminal tyrosine

residues. The value of k_{on} was calculated for YSA-Cys as $1.9*10^{3}$ s^{-1} M^{-1} (***Table 4.1***, concentration of 100 μg/mL of blocking YSA-Cys peptide) and was assumed to be the same for both the YSA-Cys and YSA peptides, based on their very similar sizes and sequence, and in consequence similar dynamics in solution and during binding to the receptor. The dissociation constants, K_D, obtained as k_{off}/k_{on} were $7.9*10^{-6}$ M and $3.1*10^{-5}$ M, giving binding affinities of 7.0 and 6.2 kcal/mol, for YSA-Cys and YSA, respectively. For comparison, the reported K_D value obtained from the Surface Plasmon Resonance (SPR) experiment was $1.9*10^{-7}$ M[198]. Based on these data it was concluded that the N-terminal part of the YSA peptide is more essential for the peptide's binding to the EphA2 receptor. This agrees with the simulation data supporting the importance of N-terminal tyrosine residues in peptide's binding to EphA2.

Comparison of binding of monomeric and dimeric ephrinA1 forms. Himanen et al.[208] demonstrated existence of two binding sites for ephrin ligands on the EphB2 receptor, the higher affinity binding site allowing for formation of the receptor-ligand dimers, and the lower affinity binding site allowing for tetramerization of the receptor-ligand units. The high affinity binding interface for EphA2/ephrinA1 dimer was recently characterized by Himanen et al.[205]. There is a strong indication that a lower affinity binding interface also exists for interaction of EphA2 with ephrinA1[205,208]. Here, both binding kinetics and strengths between single molecules of EphA2 receptor and monomeric (ephrinA1-Fc) and dimeric (ephrinA1-Fc-Fc-ephrinA1) molecules are compared. There is a possibility that the dimeric form of the ligand could bind simultaneously to both binding sites on the receptor, which should be reflected in the larger binding force for the ephrinA1-dimer compared to the monomeric ligand, which can only bind to one binding site, presumably the higher affinity one. The estimated distance between the ephrinA1 subunits in the dimer is ~15 nm, which is sufficient to reach both binding pockets on EphA2[205]. In contrast, in

our experiment there is only a small possibility that the ephrinA1 subunits of a dimer could bind at the same time to two high affinity binding sites on two different EphA2 molecules because the average distance between the centers of receptor molecules immobilized on Au surface is larger than 15 nm (~50 nm). The calculated k_{off} values of $3.6*10^{-4}$ and $1.7*10^{-4}$ s^{-1} for monomeric and dimeric ephrinA1 (***Table 4.1***) respectively, indicate slightly stronger interaction for the dimer, which can be explained by binding to both binding sites in some fraction of binding events. Occurrence of double rupture peak on force-distance curves was rarely observed (only sporadically two peaks were observed). However, given close localization of two binding sites on EphA2 (~4 nm)[205] it is possible that rupture of both interaction interfaces occurs at a very similar tip extension distance. The k_{on} values of $6.0*10^{4}$ and $2.6*10^{4}$ s^{-1} M^{-1} indicate slightly faster binding of the dimer (***Table 4.1***), which can be explained by availability of two ephrinA1 ligands in the dimer as compared to one ligand unit in the monomer, resulting in higher probability of binding to the receptor. The K_D values of $2.8*10^{-9}$ and $1.4*10^{-8}$ M, were obtained for the dimeric and monomeric ephrinA1, respectively (***Table 4.1***), indicating slightly higher binding affinity for the dimeric ephrinA1. These values are consistent with the dissociation constant obtained in the SPR experiments for EphA2 and ephrinA1 monomer [209], which are in the range $0.3\text{-}25*10^{-9}$ M. For comparison, the reported value of K_D from SPR experiment for a dimeric ephrinA5 interacting with a dimeric EphA3[210], a pair of homological receptor and ligand from the same protein families, was $1.3*10^{-12}$ M, which supports our assumption that in our experiment the dimeric ephrinA1 rather do not interact with two high affinity binding sites on two different EphA2 receptors in our sample. Based on these data, it was concluded that the dimeric form of ephrinA1 used in our experiment bound in some binding events to two binding sites on single EphA2 receptor that was reflected in smaller dissociation constant compared to

the monomeric ephrinA1. This result indicated that for therapeutic targeting of the EphA2 receptor it may be beneficial to use dimeric forms of a ligand, connected by a sufficiently long spacer, so that the dimer is able to bind to two binding pockets on the receptor. This could improve lifetime of the ligand-receptor complex and the efficiency of therapeutic targeting. Given the fact that EphA2 in cell membrane is often clustered, another way of increasing ligand-receptor lifetime would be preparing dimeric form of a ligand with spacing sufficient to bind simultaneously two molecules of the receptor.

Comparison of binding of the YSA peptide and ephrinA1 to EphA2. The blocking experiment demonstrated that YSA and ephrinA1 bind competitively to EphA2. Here the binding strength and kinetics of these two ligands were compared (we focus on YSA-Cys and ephrinA1-monomer). The smaller k_{off} value for ephrinA1 than for YSA-Cys ($3.6*10^{-4}$ s^{-1} versus $1.5*10^{-2}$ s^{-1}, respectively) indicate that binding interactions between EphA2 and ephrinA1 are stronger than interactions for the YSA peptide. This result is consistent with a larger binding interface for ephrinA1 that besides the major interaction G-H loop also involves residues in the C and E'-K fragments[205]. In contrast, much shorter (13 residues) YSA-Cys is thought to mimic only the G-H of ephrinA1. Smaller range of the YSA-EphA2 interactions compared to ephrinA1 is also reflected in the smaller width of binding well x (4.3 versus 5.9 Å, for YSA and ephrinA1, respectively, ***Table 4.1***). The association rate constant k_{on}, is larger for ephrinA1, indicating faster adjustment of this ligand in the receptor's binding site ($2.6*10^{4}$ versus $1.9*10^{3}$ s^{-1} M^{-1}, for ephrinA1 and YSA, respectively). Recent crystallographic data of Himanen et al.[205] suggested the lock-and-key binding mechanism for EphA2 and ephrinA1, in which the structure of the unbound receptor is almost retained comparing to the bound form and it is pre-shaped to accommodate ligand binding. In such case the association rate will depend on how fast ligand

can adjust to the receptor's binding site. Because the G-H binding loop in ephrinA1 is enclosed in the remaining protein structure and has limited flexibility compared to a very flexible YSA peptide, it is expected that the association rate for ephrinA1 will be faster than for YSA. The dissociation constants, K_D, $1.4*10^{-8}$ versus $7.9*10^{-6}$ M (***Table 4.1***), for ephrinA1 and YSA respectively, indicate stronger binding affinity of ephrinA1 (10.8 kcal/mol), compared to the YSA peptide (7.0 kcal/mol).

4.4 Conclusions

In this work, single-molecule AFM recognition imaging was applied to obtain quantitative data of binding thermodynamics and kinetics of YSA, a potential anti-cancer peptide, to the new cancer target, receptor tyrosine kinase, EphA2. This data comprise basis for further re-redesign of the YSA peptide towards its improved inhibitory properties against EphA2 and anti-cancer function. Binding of this peptide was compared with binding of ephrinA1, the natural ligand for EphA2. It was demonstrated at the level of individual receptor-ligand interactions that YSA and ephrinA1 bind competitively to EphA2, which suggest that YSA may bind in the same binding pocket of EphA2 as ephrinA1. These single-molecule resolution results agree with macroscopic studies of Koolpe et al. that also suggested competitive binding of YSA and ephrinA1 to EphA2[198]. This finding indicates that the known crystal structure[205] of the binding interface of the EphA2 and ephrinA1 complex could be used as a template for the re-design of the peptide to improve its inhibitory properties and specificity to EphA2. Based on interactions of individual YSA molecules and EphA2 receptors, it was also determined that the limitation of the access of the YSA's N-terminus to the EphA2 binding pocket weakens its interactions with the receptor more than when the C-terminus is blocked from contact with the receptor. This indicates that the N-terminal residues of the YSA peptide are essential for its binding to EphA2.

This result is consistent with simulation result supporting the importance of the N-terminal tyrosine residues for peptide's binding to EphA2. It provides further guidance about interactions and residues of the peptide that could be manipulated to improve its binding and specificity for EphA2. It was also determined that the monomeric ephrinA1 has larger affinity for EphA2 than the YSA peptide. Both components of equilibrium dissociation constant, the association rate constants k_{on}, and dissociation rate constants k_{off}, contribute to this larger affinity of ephrinA1. The dissociation rate constant is slightly smaller for ephrinA1, which is not surprising given the larger binding interface on EphA2-ephrinA1 complex resulting in its longer lifetime. The association rate constant is larger for ephrinA1, which can be attributed to the pre-defined, more rigid geometry of the binding loop in the full length protein than in the flexible short YSA peptide. This result is consistent with suggestion of Himanen et al. of lock-and-key binding mechanism for EphA2 and its ephrin ligands[205]. It was also tested whether using a dimeric form of ephrinA1 (ephrinA1-Fc-Fc-ephrinA1) could result in its stronger binding to EphA2 compared to a monomeric form of the ligand. In our experimental setup, dimeric ligand could only bind to two binding sites on a single receptor molecule (a known high affinity binding site and a suspected lower affinity binding site) rather than two different receptor molecules simultaneously, because of too large distances between immobilized receptor molecules. A smaller dissociation rate constant and lager association rate constant for a dimeric ephrinA1 were obtained compared to a monomeric form, resulting in larger affinity of a dimer to EphA2 and indicating that the two ephrin subunits could bind to two binding sites of the receptor molecule. This result supports the existence of second binding site on EphA2 receptor and suggests that useful strategy for improving affinity of a peptide inhibitor to EphA2 could be synthesis of its dimeric form connected by a linker. This work improves our understanding of previously

unknown interactions of the promising anti-cancer peptide candidate and the emerging cancer target, EphA2. Using the AFM recognition imaging offered capabilities to measure dynamic interactions between single molecules of receptor and ligand and obtain quantitative energetic and kinetic binding data. This data can be further used as a basis to improve therapeutic properties of the YSA peptide and develop a small-molecule anti-cancer drug targeting EphA2 receptor.

CHAPTER 5

VISUALIZING SURFACE FUNCTIONAL GROUPS OF MULTIFUNCTIONAL MACROMOLECULAR ASSEMBLIES

5.1 Introduction

Nanocarriers, such as liposomes, micelles, and self-assembled polymers, are emerging as attractive vehicles for drug delivery[211-214]. Such carriers may increase longevity of a drug in the blood stream, solubilize a lipophilic drug, offer controlled release by environmental sensitive or external stimuli, and accumulate in solid tumors by enhanced permeability and retention effect. The therapeutic efficiency of nanoparticle drug delivery systems can be further improved by surface functionalization by for example a tissue targeting ligand such as folic acid[215], a cell-penetrating molecule such as TAT or arginine rich peptides[216], or by an appropriate signaling peptide for targeting an organelle such as the nucleus[217,218].

The copper (I)-catalyzed azide-alkyne 1,3-dipolar Huisgen cycloaddition (CuAAC)[219,220] to give stable triazoles is emerging as an attractive tool for the functionalization of polymeric materials and organomicelles[221-223]. This reaction is highly efficient at ambient temperature, and tolerates a wide range of functional groups and solvents including water. Furthermore, problems arising for the cellular toxicity of Cu(I) catalysts have been addressed by employing cyclooctynes, which react with azides at room temperature without the need of a catalyst[224,225].

Although bulk compositions of functionalized organomicelles can easily be determined by conventional analytical techniques such as X-ray photoelectron spectroscopy (XPS)[226,227], transmission electron microscopy (TEM)[228], and small angle X-ray scattering[229,230], it has been

difficult to examine chemo-physical properties of individual micelle such as ultrahigh resolution images in a native environment, spatial arrangements of functional groups for the attachment of targeting devices, and mechanical properties of individual macromolecules in macromolecular assemblies. To address these pertinent problems in nanotechnology, here a convenient approach was described for the synthesis of multifunctional organomicelles that have at their surface azide moieties for attachment of targeting devices, and thioctic acids for immobilization to a gold surface. The latter type of attachment made it possible to obtain high-resolution images of the micelles by magnetic AC mode *(*MAC mode*) AFM*.[231] The distribution of azido molecules at the organomicelle surface was probed by a novel type of AFM recognition imaging that used an AFM tip functionalized with 4-dibenzocyclooctynol (DIBO)[225] (***Figure 5.1***). This functionality can react with an azide to reveal its presence and measure the force required to remove an azido-containing polymer from the macromolecular assembly.

5.2 Experiments

Materials. (3-Mercaptopropyl)triethoxysilane (80%, Sigma Aldrich); N,N-diisopropylethylamine (99%, redistillation, Sigma–Aldrich); Triethylamine (99.5%, Sigma-Aldrich); Hexane (97%, Sigma-Aldrich); CS-10 silicon AFM probe (Nanoscience Instruments); Alexa Fluor® 488 azide (Invitrogen); Doxorubicin (Bridge Bioservice); Rhodamine B (Sigma).

General procedure for the preparation organomicelles without loading (A, D, E and F): A mixture block copolymers (10 mg) in THF (1.0 ml) was slowly added to water (15 ml) under sonication. The final mixture was opened to air overnight, allowing slow evaporation of THF and formation of micelles, then dialyzed against 2.0 L of nanopure water (pre-swollen semi-permeable membrane: cutoff 12,000 – 14,000 Da) for 4 h, the water was replaced every hour.

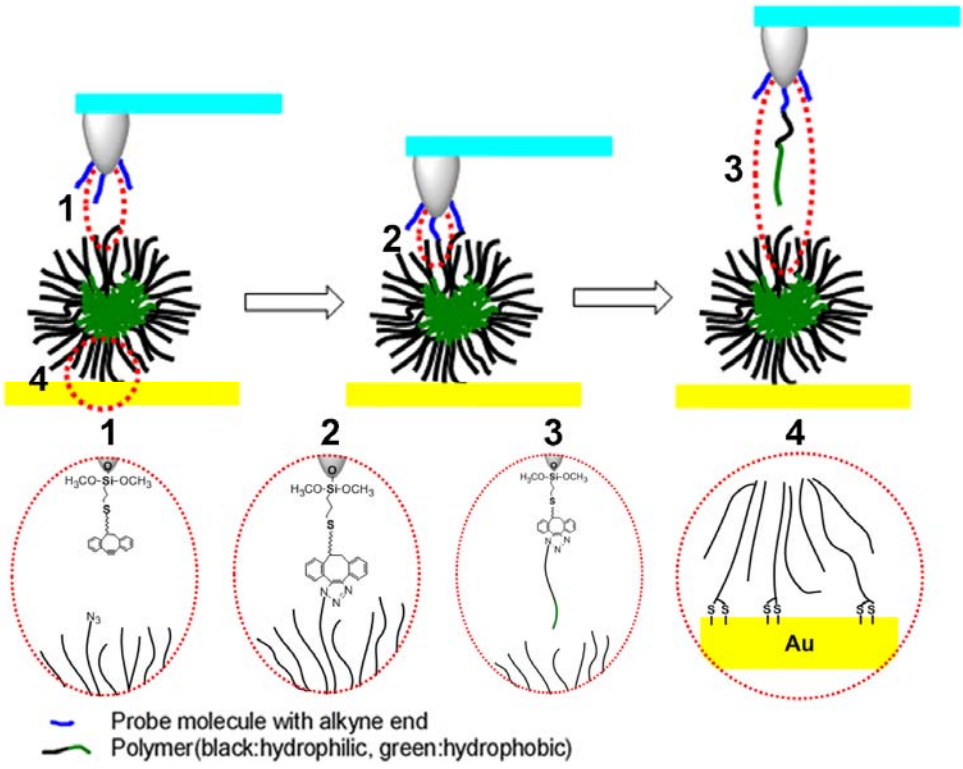

Figure 5.1 Schematic illustrations of the functionalized tip and its use in AFM recognition imaging and force microscopy for the micelles. **1.** The AFM tip was first modified by (3-mercaptopropyl) triethoxysilane to cover its surface with thiol groups which were further reacted with Compound **7** to obtain cycloalkyne functionalized surface; **2.** The recognition between the functionalized tip and micelle with azido moiety was accomplished through catalyst-free Huisgen cycloaddition; **3.** The cycloadditioned polymer was pulled out from the micelle assembly; **4.** The micelle with thiol moiety was immobilized on gold substrate through Au-S bond.

General procedure for the preparation of loaded organomicelles (B and C): DOX or rhodamine B (1 mg) was added to a solution of block copolymer (10 mg) in THF (1.0 ml). The mixture was slowly added to water (15 ml) under sonication. The final mixture was opened to air overnight, allowing slow evaporation of THF and formation of micelles, then dialyzed against

2.0 L of nanopure water (pre-swollen semi-permeable membrane: cutoff 12,000 – 14,000 Da) for 4 h, the water was replaced every hour. The micelle solution was passed through a syringe filter (pore size 0.45 μ m; Millipore, Billerica, MA) to remove drug or dye aggregates.

AFM tip modification: Tips were cleaned by UV for 30 min and then coated with a magnetic film by the e-beam deposition. The tips were immediately placed in a glass desiccator filled with argon. Next, (3-mercaptopropyl)triethoxysilane (20 μL) and of *N*,*N*-diisopropylethylamine (10 μL) was added into the small containers in the desiccator; then the desiccator was vacuumed until the pressure inside was about 1 torr and the tips were kept in the environment for 60 min.[32,132] The organo-silicon coated tips were washed with hexane for 15 min using sonication and then immersed in the solution of Compound **7** (4 mg/mL) in DMF (400 μl) and triethylamine (5 μL) for 5 h. Finally, the tips were rinsed with water for several times and kept in the pure water at 4 ºC.

AFM sample preparation: A fresh thermal evaporated gold surface was annealed by hydrogen flame, then immediately covered with nanoparticle solution (1 mg/mL) for 2 h at 4 ºC. The surface was rinsed three times with 18 MΩ DI water and then examined by the AFM. For recognition experiment, a ten-fold diluted solution of nano-particles was employed.

AFM experimental procedures: For the force microscopy study, the AFM cantilevers were stretched under several different pulling rates, range from 300~4000 nm/s. For each pulling rate, 1000 pulling trajectories (*i.e.* force-distance curves) were recorded at room temperature. The statistical histograms of force-distance curves were obtained from a subset of the pulling traces that represented the successful binding events. In the statistical study, the apparent loading rate was applied to attain the loading rate dependence of force and stretching distance.

Experiment procedure for force spectroscopy with retention time: The fresh annealed gold surface was incubated with Micelle A solution (0.1 mg/mL) for 1~2 hour. After incubation, the sample was gently rinsed with water and kept under water. Before doing force spectroscopy, few images for an area of 2000 nm by 2000 nm were scanned. After a suitable area was found, AFM probe was directly located above the micelles, thereafter only 200 force curves was collected for each retention time at loading rate of about 10 nN/s under force spectroscopy controlled by home-built Labview program since our previous experience in force spectroscopy showed one modified tip only had limited lifetime of about 1000 fore curves. During force curve collection, tip was relocated on couple of micelle surfaces to ensure there are enough azide moieties available on micelle surface. Comparing to commercial force spectroscopy including two sections (approach and retraction), force spectroscopy used in our study provides extra accessibility in retention time and stretch mode including the continuous and modulated. Several retention times were measured here, 0 ms, 200 ms, 400 ms, 600 ms, 800 ms and 1000 ms.

5.3 Results and discussions

5.3.1 Micelle preparation

Various compounds have been designed for this study (***Figure 5.2***). Dibenzocyclooctynes (Compounds **7**) and azides (Compound **15**) were selected for tip and macromolecule modification respectively. These groups, which individually exhibit excellent stability, have been shown to undergo a fast strained promoted cycloaddition to give a stable triazole. Block copolymer **15** was synthesized, which in an aqueous environment will assemble into micelles carrying azido functions at its surface. The additional use of block copolymer **16**, which carries a thioctic moiety at the polar terminus, was expected to offer an opportunity to attach the resulting

particles to a gold surface. Block copolymer **17**, having the polyethylene glycol moiety modified as methyl ether, would allow controlling the density of the functionalities at the micelle surface. Copolymer **18** has a similar structure as **17**, however, it contains an azido function at the apolor β-poly(ε-carprolactone) moiety and it was expected to reside at the internal environment of micelles. To synthesise the macromolecular assembly micelles with different compositions, chemical and physical properties, various combinations of block copolymers (**15-18**) in THF were added to nanopure water followed by dialysis to give a range of micelles expressing different sets of functional groups (***Table 5.1***).

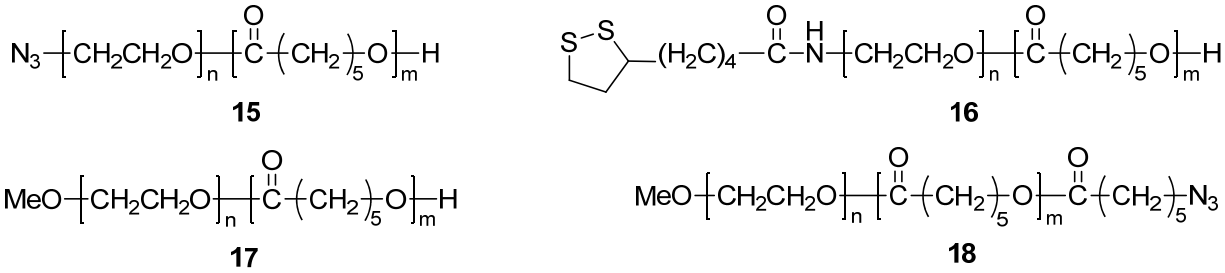

Figure 5.2 Components for the assembly of multi-functional organomicelle.

Table 5.1 Copolymer Composition of Organo-micelles[a]

Micelle	Polymer 15	Polymer 16	Polymer 17	Polymer 18	loading
A	10%	10%	80%		-
B	10%	10%	80%		Doxorubicin 3wt%
C	10%	10%	80%		Rhodamine B 9wt%
D		10%	90%		
E		10%	80%	10%	
F	10%		90%		

[a]The composition of the micelles is expressed as weight percent

5.3.2 High resolution image

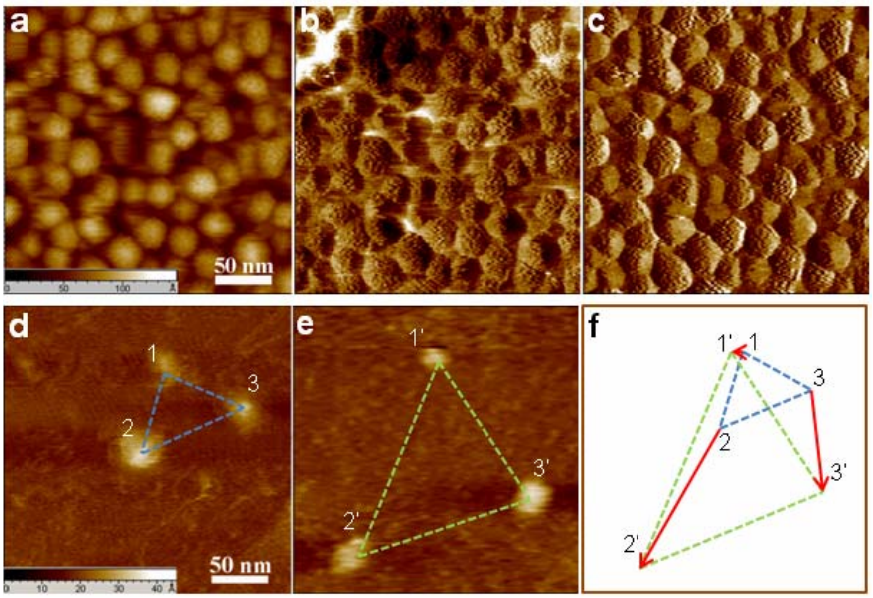

Figure 5.3 The topographical (a), phase (b) and amplitude (c) images of micelles **A** using Magnetic AC mode *(*MAC mode*)* AFM imaging. The nanometer features of the micelle surface are clearly resolved. The topographic images of Micelles F at the beginning (d) and after 8 minutes of scanning (e). The positional change of the micelles (f).

To obtain high-resolution MAC mode images, the various multifunctional micelles were attached to an Au(1,1,1) surface *via* thiol-gold linkages (***Figure 5.1***) and unbound material was removed by washing with water. AFM tips, which were cleaned by UV exposure and coated with a magnetic film by ion-beam deposition, were employed for scanning a maxium area of 10 μm^2 using an Agilent multi-purpose AFM scanner. Silicon cantilever tips (Nanoscience Instruments) with a nominal spring constant of approximately 0.1 N/m were used throughout the experiments.

Ultrahigh resolution images of micelles **A** using MAC mode scanning are shown in ***Figure 5.3***. The organomicells are uniformly distributed and have a diameter in the range of 20 to 50 nm. The topographic (a), phase (b) and amplitude (c) images show fine structural details of the micelle surface, and in particular the phase and amplitude images reveal molecular details. In this respect, the spots and strings represent the chemical groups and polymers that make up the micelle surface. As expected, organomicelles **B**, **C**, **D** and **E** gave similar high-resolution images (see APPENDIX B). Loaded organomicelles **B** and **C** had similar diameter as that of unloaded micelles (Micelles **A**, **D**, **E**), indicating that loading did not change the size and morphology. Importantly, micelles **F**, which did not contain surface thiol moieties for immobilization, had a similar size as the other micelles, but did not show molecular details of the micelle surface (***Figure 5.3*** d, e, f). Furthermore, these micelles appear to move randomly over the surface as shown in a topographic image measured after a lapse period of 8 minutes.

5.3.3 Map micelle surface functional group by recognition image

To examine the chemical composition of the surface of the micelles, AFM recognition images were obtained using tips modified by 4-dibenzocyclooctynol **7**. These tips were prepared by subsequent coating with a magnetic film and a gold layer followed by reaction with (3-mercaptopropyl) triethoxysilane in the presence of *N*,*N*-diisopropylethylamine. Next, the organosilicon covered tips were immersed in a solution of compound **7** in the presence of triethylamine in DMF resulting in modification with 4-dibenzocyclooctynols[225].

To validate recognition specificities, AFM recognition imaging experiments were conducted employing immobilized organomicelles **A**, **D** and **E**. First, micelles **A** were examined by employing an unfunctionalized tip, and the topographic image (bright spots, ***Figure 5.4*** a, top) clearly demonstrated the presence of micelles. As expected, the recognition image did not reveal

reaction events (***Figure 5.4*** a, bottom). However, imaging of micelles **A** with the 4-dibenzocyclooctynol functionalized tip revealed specific reaction events as represented by the dark spots in the recognition image (***Figure 5.4*** b, bottom). As expected, no recognition was observed when a similar experiment was performed with organomicelles **D** and **E**, which do not contain azido moieties or have azido groups at the interior of the micelle, respectively.

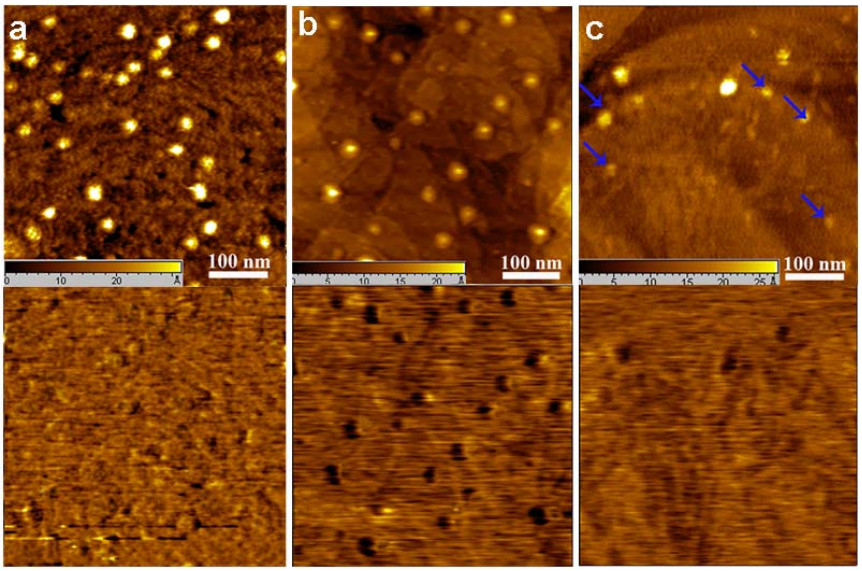

Figures 5.4 Topographic (top) and recognition (bottom) images. a) Micelles **A** examined by an unmodified tip, showing no recognition events; b) micelles **A** scanned by a 4-dibenzocyclooctynol-modified tip, showing recognition events (dark spots); c) a mixture of micelles **A** and **D**, which contain azido moiety or do not have azido in micelle composition respectively, was imaged by cyclooctyne-modified tip, showing recognition events in some of micelles and others that do not exhibit recognition events are indicated by blue arrows in the corresponding topographic image

To further verify the recognition specificity, a mixture of organomicelles **A** and **D** was investigated. As expected, in the topographic image (***Figure 5.4*** c top), the two types of micelles

were indistinguishable, however, the recognition image (***Figure 5.4*** c bottom), clearly demonstrated recognition in some but not all of the micelles. These results unambiguously demonstrate that recognition events only occur when the 4-dibenzocyclooctynols attached to the tip chemically reacts with azide moiety at the surface of organomicelles.

Previously, AFM recognition imaging has been used to examine compositions of target structures by employing receptor-ligand interactions.[32,232-235] In this approach, a magnetically driven AFM tip modified with a ligand or receptor is oscillated while scanning across the surface. The surface topography and recognition events can be delineated in a temporal and spatial manner as they affect different part of the sinusoidal cantilever oscillation. The recognition images described here are obtained by a fundamentally different approach that is based on a chemical reaction between two functional groups. As a consequence, a functional group attached to a tip can only be employed once to detect its counterpart, and hence it was important to examine the number of recognition events that can be measured by a single tip. In order to examine the number of recognition events that can be measured by a single tip until the functional groups were totally consumed, *in-situ* time-laps recognition imaging of micelles **A** was performed using a tip functionalized with compound **7** (22 mer, about 9 nm long) and (4 mer, about 2 nm long) in ***Figure 5.5***. 300~500 (compound **7,** 22 mer**)** and 50-60 (compound **7,** 4 mer) recognition events were realized by assuming that each black spot corresponds to a single reaction between azide and cyclostyle. The multiplicity of 4-dibenzocyclooctynol **7** on the AFM tips was confirmed by fluorescence images of tips labeled with Alexa Fluor® 488 azide and rhodamine B included micells **C** in ***Figure 5.6***, showing evenly distributed 4-dibenzocyclooctynol **7** on the tip surface.

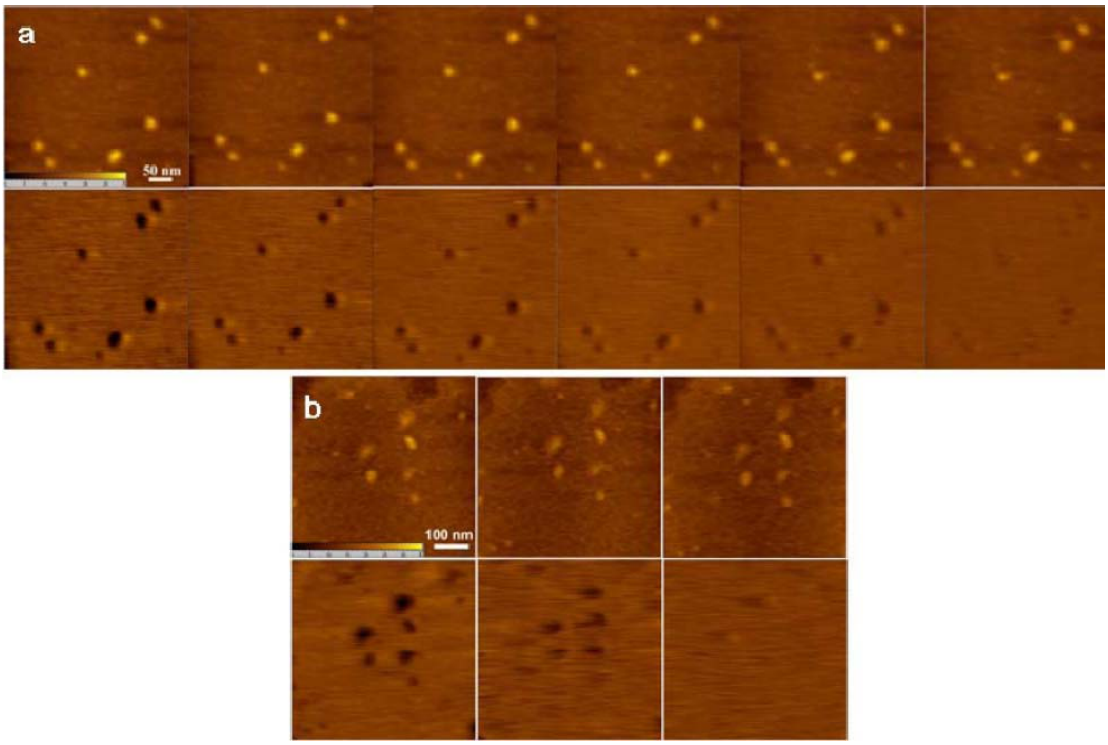

Figure 5.5 Time-laps recognition imaging of micelles A by the tip modified with 4-dibenzocyclooctynol containing linkers Compound **7** (22 mer, approximately 9 nm, a) and (4 mer, 2 nm, b). Images at 0, 30, 60, 90, 120, 150 min (from left to right, a) and at 0, 15, 30 min (from left to right, b) show fading and eventually vanishing of the recognition events as the 4-dibenzocyclooctynol groups of the tip are being consumed by reaction with azides.

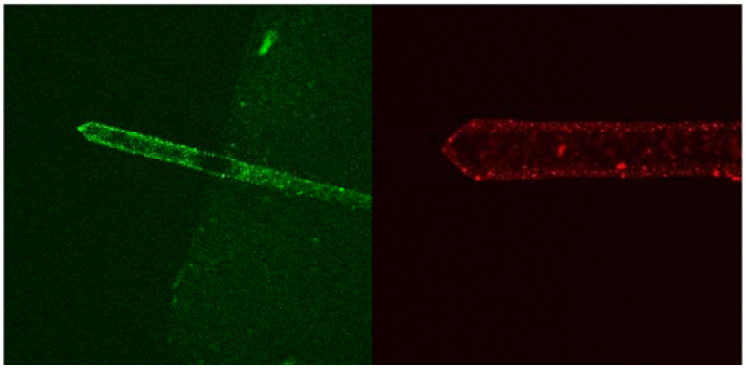

Figure 5.6 Confocal images of tips labeled with Alexa Fluor® 488 azide and Rhodamine B TAG-loaded micelles **C**.

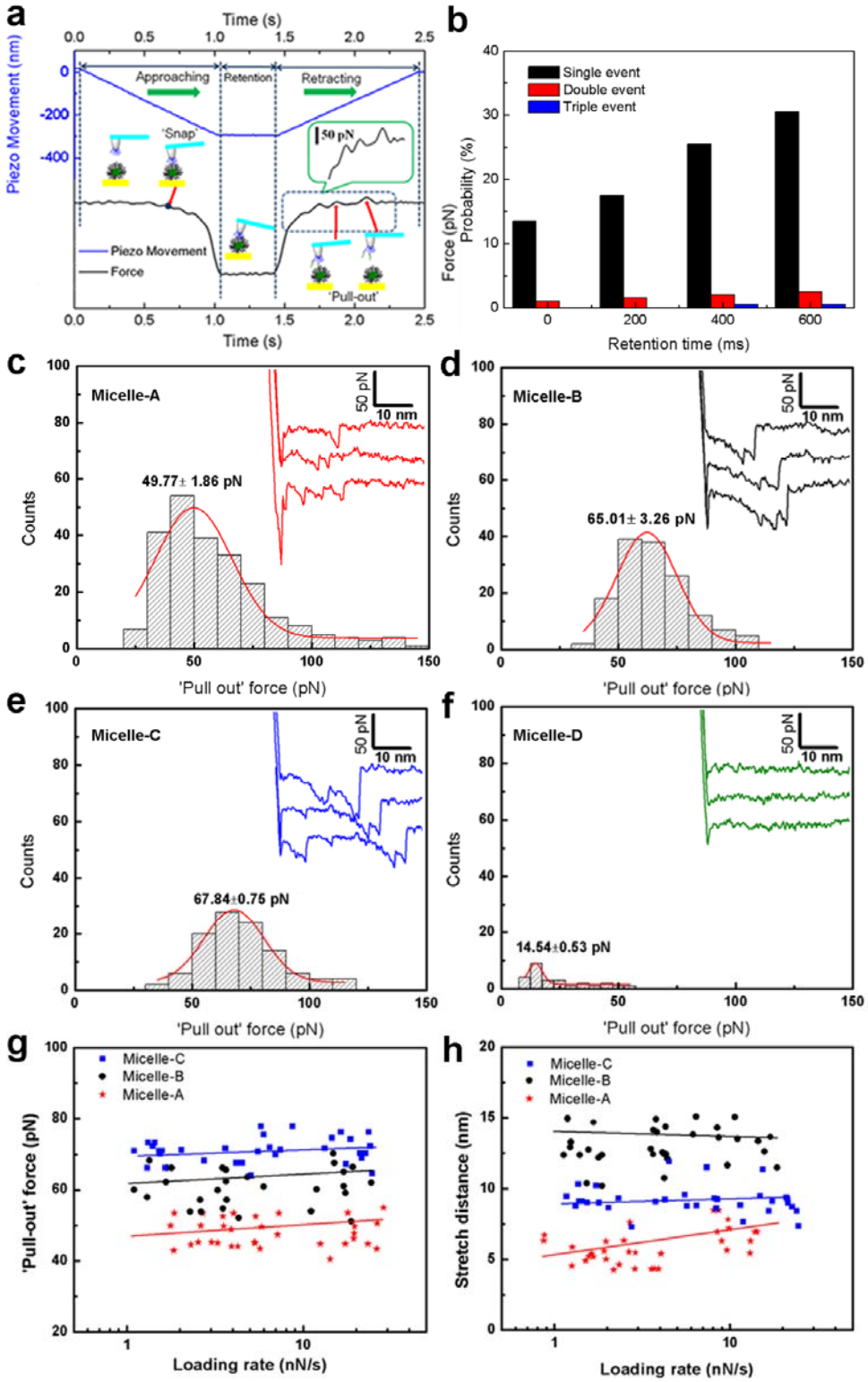
a
Time (s)
Piezo Movement (nm)
Approaching
Retention
Retracting
'Snap'
50 pN
Piezo Movement
Force
'Pull-out'
b
Single event
Double event
Triple event
Force (pN)
Probability (%)
Retention time (ms)
c
Micelle-A
50 pN
10 nm
49.77± 1.86 pN
Counts
'Pull out' force (pN)
d
Micelle-B
65.01± 3.26 pN
e
Micelle-C
67.84±0.75 pN
f
Micelle-D
14.54±0.53 pN
g
'Pull-out' force (pN)
Loading rate (nN/s)
h
Stretch distance (nm)

Figure 5.7 Relationship between the contact time and number of polymers removed. a) The active control of the AFM tip movement in which a whole process is divided into approaching, retention, and retracting. The retention process is used to control the number of the 4-dibenzocyclooctynol-azide click reactions. b) Probability of curves with single, double and triple recognition event. Histograms used to determine the most probably force to remove a "clicked polymer" from micelles **A** (c), **B** (d) , **C** (e) and **D** (f) from the force-distance curves at apparent loading rate of around 15 nN/s (inserts). g) Typical distribution of the "pulling-out" force depending on the apparent (force) loading rate for micelles **C** (blue, square), micelles **B** (black, circle) and micelle **A** (Red, pentagon), the line indicates the most possible magnitude at different force loading rate. (h) The typical distribution of stretch distance depending on apparent loading rate for micelles **C** (blue, square), micelles **B** (black circle) and micelles **A** (Red, pentagon), the line indicates the most possible magnitude at different loading rate.

5.3.4 Force spectroscopy

As the recognition is based on a chemical reaction between two functional groups followed by removal of a polymer, the number of the recognition events should also depend on the contact time of the functionalised AFM tip to the micelle surfaces. ***Figure 5.7*** a shows the experiment design to precisely control the movements of the AFM tip so as to control the retention time. It was found that the probability for the curves with single recognition event increases from about 14% with 0 retention time to about 30% with 600 ms retention time. Accordingly, the probability for the force curves with the double and triple events follow the same trend. The total recognition events add up to about 300, agrees with the previous estimation from the time-laps recognition imaging data.

The recognition images can reveal the presence of azide moieties at the surface of the micelles; however, it cannot distinguish between micelles **A** and **B** or **C,** which are composed of the same block copolymers but differ in the absence or presence of a load. Hydrophobic forces are important determinants of the assembly of organomicelles in water and therefore, it was expected that loading would influence the force required for removal of a block copolymer molecule from a micelle. Indeed, two important differences were observed in the force-distance curves of micelles **A** (***Figure 5.7*** c), **B** , **C** and **D** (***Figure 5.7*** d, e), including 'pull out' force(***Figure 5.7*** g) and stretch distance (***Figure 5.7*** h). In particular, the 'pull out' forces were significantly larger for micelle **B** (63.17±1.84 pN) and **C** (69.57±1.56 pN), which were loaded with doxorubicin and rhodamine respectively compared to micelle **A** without loading (48.16±1.81 pN). Also, the stretching distances were much longer for **B** (13.58±0.40 nm) and **C** (9.32±0.28 nm) compared to **A** (5.55±0.23 nm). The critical micelle concentration[236,237] for **A** was higher than that for **B** and **C,** supporting differences in stability of the two preparations. The increased stability of the micelles is probably due to hydrophobic interactions between the apolar loading material and the PCL component of the micelles. The difference in breaking forces and stretching distance for **B** and **C** are probably due to differences in loading content and molecular characteristics of the load.

5.4 Conclusion

Multifunctional nanocarriers such as micelles, liposomes and polymeric nanoparticles are emerging at smart materials for drug delivery. Although bulk compositions of such assemblies can easily be determined by conventional analytical techniques, it has been difficult to examine chemo-physical properties of individual micelles. Here, a novel Atomic Force Microscopy (AFM) approach was described that makes it possible to provide ultrahigh resolution images of

organomicelles, map spatial arrangements of surface functional groups, and measure forces required for removal of a block copolymer molecule from the macromolecular structure. Key features of the technology include immobilization of thioctic acid containing organmicelles to a gold surface and the use of a tip functionalized with 4-dibenzocyclooctynol. The latter functionality can react with an azido-containing polymer to reveal its presence and measure the force required for its detachment from the macromolecular assembly. It has been shown that the AFM tip can be modified with sufficient 4-dibenzocyclooctynols to detect a large number of azido moieties. The methodology made it possible to distinguish a range of different nanostructures that differ in chemical and mechanical properties.

CHAPTER 6

FIBRINOGEN ASSEMBLY ON GOLD AND ITS CLOTTING INDUCED BY GOLD NANOPARTICLE

Chen, G. J.; Ni, N. T.; Wang, B. H.; Xu, B. Q., Fibrinogen Nanofibril Growth and Self-Assembly on Au (1,1,1) Surface in the Absence of Thrombin. Chemphyschem 2010, 11 (3), 565-568. Reprinted with permission of publisher. Copyright 2011 Wiley-VCH
Chen, G. J.; Ni, N. T.; Zhou, J. F.; Chuang, Y. J.; Wang, B. H.; Pan, Z. W.; Xu, B. Q., Fibrinogen Clot Induced by Gold-Nanoparticle In Vitro. J. Nanosci. Nanotechnol. 2011, 11 (1), 74-81. Reprinted with permission of publisher. Copyright 2011 American Scientific Publishers

6.1 Fibrinogen assembly on gold

6.1.1 Abstract

Understanding protein adsorption on gold surface bears increasing importance because of surface-induced changes in conformation and bioactivity. Nanofibril structures of protein fibrinogen (fg) molecules, playing paramount role in blood coagulation, are found self-assembled on Au(1,1,1) surface without any addition of thrombin, growing in two orientations (longitude and transverse).

6.1.2 Introduction and literature review

Fibrinogen (Fg), an abundant plasma protein, is particularly paramount in the intrinsic and extrinsic coagulation cascades.[238] It is the scaffold of thrombus which is the leading cause of death in industrialized nations. The thrombosis process could also bring severe consequence to the implanted biomaterial, such as cardiovascular biomaterial, stents and catheters, if undesirable blood clot is formed.[32] In this process, the adsorption and activity of fibrinogen on biomaterial surfaces represents a key variable. Due to these considerations, extensive researches have been carried out. The studied surfaces include mica[239-242], graphite[239-242], silicon&silica[243,244], chemical modified silicon[245], polymer coated surface[246], gold[247], titanium oxide[248], and self-assembled monolayers[240,249]. Among them, the mica and graphite are intensely studied since they are the typical models of two classes of surface: hydrophilic and hydrophobic. In addition, different characterization methods were adopted in these works, such as total internal reflectance fluorescence (TIRF)[244], surface plasma resonance (SPR)[246], Ellipsometer[250], and atomic force microscope (AFM)[240,241]. Comparing to these optical measurement, AFM can provide the vivid

and high resolution image of single protein, which indicates the dynamic adsorption information.[251]

To date, the study based on the gold surface is very limited. This circumstance doesn't match the pace of the study on gold nano-particle, which has a promising biomedical application in drug-delivery, medical imaging or direct injection, since the safety of gold nano-particles is increasingly concerned[252].

Here, we focus on the special assembly process of fibrinogen on the gold surface. Control experiments were also carried out on the two typical model surfaces, hydrophobic highly ordered pyrolitic graphite (HOPG) and hydrophilic muscovite mica. A novel phenomenon was found that the ordered self-assembly of fibrinogen without any addition is proper to gold surface. This finding can benefit basic understanding of fibrinogen coagulation on implanted materials and provide some clues for other possible adverse effect of gold nano-particles.

6.1.3 Materials and Methods

Materials. Human fibrinogen was purchased from sigma-aldrich as lyophilized powder containing 68% protein and salts (~15% sodium citrate and ~25% sodium chloride). Stock solution at a concentration of 1 mg/ml were prepared in the tris buffer (20 mM Tris HCl , NaCl 300 mM, $MgCl_2$ 5 mM and pH 7.6) and stored at -20 ºC in 100 μL aliquots. To ensure the biological activity of protein, the stock solution was only kept for one week. Before using, the stock solution was thawed at r.t. for 15 min and diluted to the final concentration by the same buffer.

Sample Preparation. The fresh thermal coated gold chip[253] on mica was annealed for 2 min by hydrogen flame to remove the possible contamination and attain the Au (111) structure. Then the chip was immediately incubated with 400 μL desired concentration of fibrinogen

solution for 30~60 min. Before imaging, the sample was gently rinsed with the buffer several times.

Fibrinogen clotting test by microreader. Fresh prepared fibrinogen (1 mg/mL) solution in the buffer (20 mM Tris HCl, pH=7.6, NaCl 300 mM and $MgCl_2$ 5 mM) was diluted to final concentration (10 μg/mL, 5 μg/mL, 2 μg/mL and 1 μg/mL). The solutions were added to 96-well plate respectively. All of the mixtures were votexed by Vortex-1 Genie Touch Mixer to make the homogeneous solutions. Control solution (no fibrinogen) was also added. The UV_{405} of each well was detected by using a Perkin-Elmer microplate reader every 5 minutes.

Surface plasma resonance. The adsorption experiment (4 μg/mL fibrinogen solution, 500 μL) was performed by using surface plasma resonance (SPR) machine (Reichert SR7000C). The fibrinogen solution was prepared freshly in the buffer. The fibrinogen solution was injected at the velocity of 0.008 mL/min for around 1h, followed by several hours rinsing. The immobilization can be read out by the increasing of the signal (μRIU).

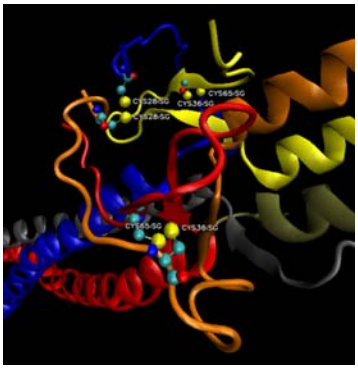

Figure 6.1 The stereo depiction of disulfide bonds (yellow colored ball) in the central E domain of fibrinogen.

Protein structure. The recent released protein crystal structure of human fibrinogen [254], denoted as '3GHG', was adopted here to obtain the three dimensional structure of E domain in

Figure 6.1. The protein sequence was edit by Swiss-pdbviewer[255] and then visualized by VMD (Visual molecular dynamics).

As known, the two halves are joined by 5 disulfide bonds, which include 3 symmetrical between adjacent AαCys[28], γCys[8] and Cys[9] [254,256,257] and the disulfide link between Bβ Cys[65] of one half and AαCys[36] of the other [258]. To explicitly illustrate the availability of disulfide bond to the gold surface, the side-chains of these residues were presented in ***Figure 6.1*** and the disulfide bonds were denoted as yellow-colored ball and stick. Since γCys[8] and Cys[9] were not found in the sequence of protein crystal structure, it would not show in the ***Figure 6.1*** either. It was clear that all these disulfide bonds were exposed outside, which made them accessible to gold surface and finally formed Au-S bonds[176].

AFM Imaging. (The same apparatus and similar operation setting up as Chapter 2)

6.1.4 Results and discussion

Conformation variation on different surface

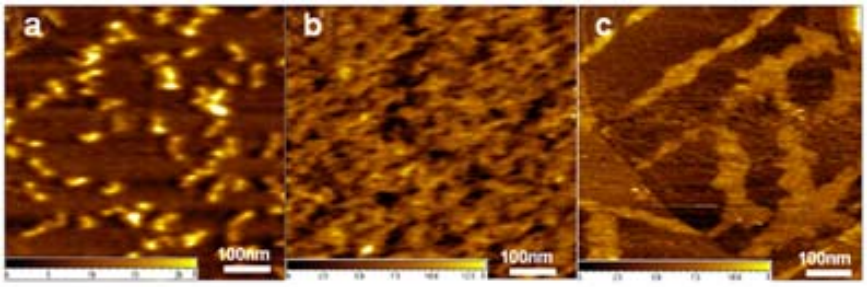

Figure 6.2 The topographical images of fibrinogen on three different surfaces. (a) mica, (b) HOPG, and (c) gold. All the surfaces were prepared under the same condition (fibrinogen solution (4 μg/mL) and 50 min incubation time).

The fibrinogen samples on three different surfaces were prepared and performed under the same condition (4 μg/mL fibrinogen and 50 min incubation). As shown in ***Figure 6.2*** (a), most of fibrinogen molecules on the mica surface keep their native trinodules structures, which was first proposed by Hall and Slayter in 1959[259] and the length of which is about 50 nm consistent with the reported data.[240] By contrast to the mica surface, the HOPG surface was covered a more condensed protein layer, which illustrates that the hydrophobic HOPG surface has stronger adhesion to fibrinogen than hydrophilic mica surface. The similar conclusion was also attained by Agnihotri[239] and Geer[260]. Although the isoelectric point of gold surface is found at around pH=4.5[261], which indicate that the gold surface is also hydrophilic and negative charged in the presence of buffer, there is more compact ordered fibrinogen on the gold surface than the mica surface, as shown in ***Figure 6.2***(c). It either shows the totally different organization features compared to the HOPG surface. The fibrinogen patches on gold surface have specific ordered structure, to the contrary there is only messy and unordered Fg layer piled up on HOPG surface. Since the UV405 nm data in ***Figure 6.3*** already excluded the possibility of fibrinogen coagulation in the solution, it was certain that this new finding is due to the interaction between the surface and protein molecules. And a kinetic adsorption measurement was carried out below to explore the instinct causes.

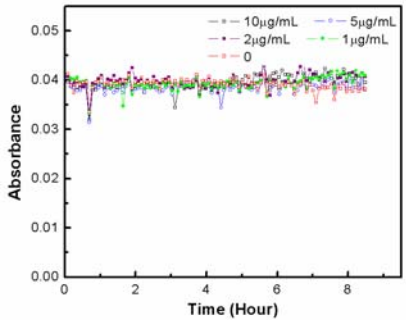

Figure 6.3 UV 405nm absorption of different concentration fibrinogen solution.

Two growing pathway

The flow-cell technique was adopted here to monitor the developing process of fibrinogen patches on the gold surface. In the stable condition of AFM, 400 μL fibrinogen solution (4 μg/mL) was slowly injected into the liquid cell while AFM probe was scanning. From the time-line data, ***Figure 6.4*** (a), it was clear that the fibrinogen can grow into fibril at two orientations (longitude and transverse) without any addition, step by step once the initial fibrinogen molecules attached on the surface. The quantitative kinetic information can also be estimated from the image by measuring the dimension of fibrinogen patches. To present the patches in detail, a snapshot in the process was taken out as ***Figure 6.4*** (b) and (c), which showed the delicate structural features of the fibrinogen patches grown in two different directions. It was further schematically illustrated in ***Figure 6.4*** (d). The single fibrinogen strand can be distinguished clearly from both the topographical and amplitude images, with around 5 nm in width, which is pretty close to the diameter of nodule of D domain and E domain[238].

To the knowledge of the authors, it has not been reported so far that fibrinogen can polymerized into the fibril in the absence of thrombin and Ca^{2+} in the aqueous condition and its two growing pathways. There is no exact model to follow; and the mechanism for these assemblies on gold surface is still unknown. Sit[241] *et al* reported the fibrinogen monomers can assemble into an extensive fibrin network from initial short linear strands on HOPG with the addition of thrombin; However, all the proteins including the added thrombin would keep their monomeric states on mica. Reichert[262] *et al* recently discovered that the formation of fibrinogen fibril can be induced by the surface steps of the HOPG without addition under ambient condition; However, fibrinogen fibril cannot be found in the liquid condition. They thought the fibrils were formed during sample rinsing and drying steps. It was proposed that the coupling of 'αC domains'

on adjacent molecules contributes to the formation of fibrinogen fibril[242,262]. However, this explanation isn't fully fit with our observation since the electrostatic interaction between the negative charged gold surface and positive charged 'αC domains' would make these domains unavailable to form the lateral intermolecular interactions[242]. By contrast, fibrinogen on gold surface can automatically assemble into an ordered fibrin network without the addition of catalyst, 'thrombin'. The possible reason to promote the assembly of fibrinogen could be the strong interaction between Au and sulfide, since there are plenty of disulfide bridges in the structure of fibrinogen, which play a pivotal role in the inter-chain and intra-chain linkages[263].

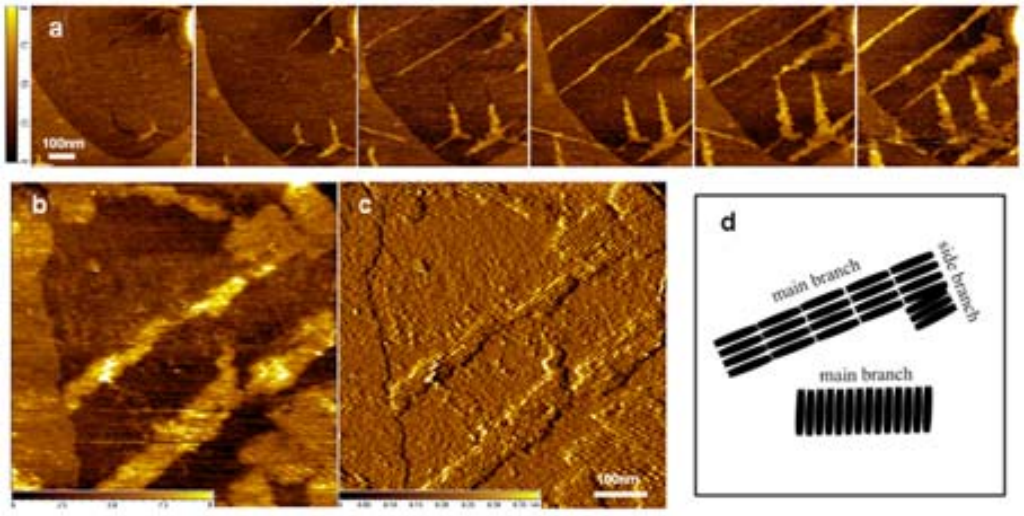

Figure 6.4 The fibrinogen growing process on gold surface. (a) The time-laps images of the fibrinogen assembly process on the gold surface. The interval between each image is about 7~8 min. The high resolution images of fibrinogen patches on the gold surface. (b) topography image, (c) amplitude image, (d) the schematic description of fibril grown in two orientations: transverse and longitude.

Possible mechanism

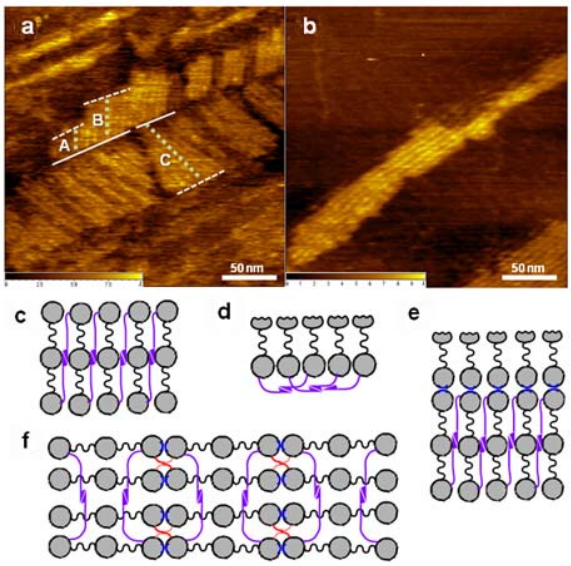

Figure 6.5 The high resolution image of fibrinogen transverse assembly (a) and longitude assembly (b). The schematic representation of the possible mechanism for the assembly: (c) for patch B in transverse case; (d) for patch A in transverse case; (e) for patch C in transverse case; (f) for the longitude case. (Curve with arrow: 'αC-domain' interaction; blue fragment: 'D:D' interaction; red curve: 'γ_{XL}' interaction)

Human fibrinogen is a dimeric molecule, the paramount disulfide bonds can act as connectors and organizers[263]. The study indicated that the disruption of disulfide bonds in E domain can result in the appearance of half-molecules[264]. In our study, fibrinogen patches with different length were observed in the transverse growing fibrils as shown in ***Figure 6.5*** (a), and were labeled as A, B, C, respectively. The length of A part is around 22 nm, which is almost exact half of the dimeric molecule. Nevertheless, B part could be assembly of intact fibrinogen molecule according to its length (about 41 nm). The length of c) part could be longitudinal sum of intact and half fibrinogen with 65 nm in length. These data demonstrated that the interaction

between Au and disulfide bonds in E domain could cleave the dimeric fibrinogen into halves and also facilitate the coagulation process. The ***Figure 6.5*** (b) presented case of longitude growing fibrils. To further prove our hypothesis, a surface plasma resonance (SPR) experiment was done, which was shown in ***Figure 6.6***. The data clearly indicated that the adsorption process was not pure physical process and there was strong binding between the protein and gold surface which only could be Au-S bonding. Additionally, the three dimension protein structure also provided very strong evidences to our hypothesis shown in ***Figure 6.1***.

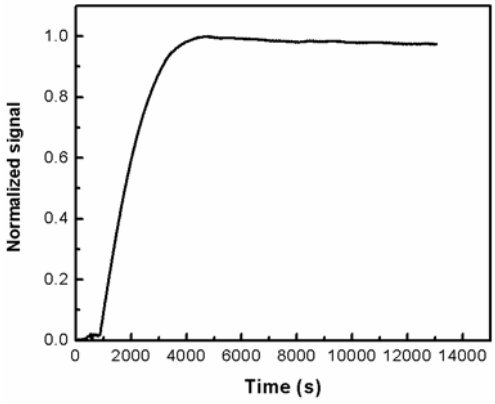

Figure 6.6 The adsorption curve of fibrinogen on the bare gold surface which collected by SPR

Although it was certain that the proteins can attach to the surface through the Au-S bond, the impetus to align them orderly was still unclear. There are three possible non-covalent interaction participating in fibrinogen assembly and cross-linking, namely 'αC-domain' in α chain of D domain[265], 'γ_{XL}' and 'D:D' in γ chain of D domain[266,267]. Among them, the 'αC-domain' is an important factor in lateral fibril association and extensive network assembly. As discussed previously, the negative charge of gold surface could be impedance to activate the 'αC-domain'. However, the strong interaction of Au-S between surface and E domain would overcome the hindrance to make the the 'αC-domain' separate from E domain since the

interaction between C-terminal of the α-chains and E domain highly depends on the formation of disulfide bonds [268]. And 'αC-domain' interaction already was thought to be a vital factor in the formation of fibril on the surface[242,262]. For the later two interactions, they are self-association processes, so they would be available when the binding sites happen to each other. Certainly, the most important Au-S interaction cannot be ignored.

The intact fibrinogen assembly (patch B, ***Figure 6.5***(a)) may be the simplest case. The released 'αC-domain' by Au-S interaction could be main reason for the patterned structure, as shown in ***Figure 6.5*** (c). For the patch A in ***Figure 6.5*** (a), the half molecule assembly, it could possibly attribute to the same reason but in different connection way illustrated in ***Figure 6.5*** (d). While the length was getting longer, such as patch C in ***Figure 6.5*** (a), the possible interactions inside the assembly would be more complicated; however, 'αC-domain' interaction undoubtedly would be still the main cause. Besides, the 'D:D' interaction would be helpful for the elongation, as shown in ***Figure 6.5*** (e). The ***Figure 6.5*** (f) illustrated the most complicated case, the longitude growing fibril. All the three interaction could possibly contribute to the formation of the longitude assembly.

6.1.5 Conclusion

It has been known that thrombin plays an important role in the fibrinogen coagulation; however, fibrinogen on gold surface can self-assemble into fibrin network surface without any addition. This circumstance is special for gold surface comparing with mica and HOPG. The fibrinogen patches can grow in two orientation, longitude and transverse. According to the experimental results, it was kindly safe to make the deduction about assembly mechanism: Au-S interaction and its activated interaction in 'αC-domain' are two main causes for the patterned assembly. Besides, 'D:D' and 'γ_{XL}' interactions do help to the elongation and strengthen of fibril

assembly. Comprehensively, for all the cases, longitude and transverse, the previous two factors were believed to be very important. The phenomena also provide some clues about bio-safety study of gold nano-particles.

6.2 Fibrinogen Clot Induced by Gold-nanoparticle[269]

6.2.1 Abstract

Protein-gold nanoparticle (GNP) interactions and their biological consequences are one of the most fundamental issues that are exigent for GNP biomedical applications. Wee report on our findings here that the interaction of GNP and fibrinogen (fg) could induce blood clot, one important blood protein, under near-physiological conditions (see Figure). Firstly, through different characterization methods, namely, UV spectrum, dynamic lighter scattering and atomic force microscopy, fg-GNP clots with the μm size were found to be formed and their average size is time- and concentration dependent. Besides, the dissociation constant was calculated to be 1.36~2.05 μg/mL (nM level), suggesting that the interaction between fg and GNP is very strong. Finally, by scrutinizing the fg sequences, this strong binding was found to originate from many Cys residues distributed in α, β, and γ chains of fg through Au-S bond. Most of these Cys residues are in the form of disulfide bonds, which locate at the central E domain and flank parts of C-terminal and N-terminal in the coil-coil region.

6.2.2 Introduction and literature review

The unique and tunable optical properties of gold nanoparticle (GNP) as a result of surface plasmon resonance offer many promising applications in biomedicine, such as chemical sensing, imaging and photo-thermal therapy.[270-276] Currently, the huge challenge associated with

these applications to real clinical test is to fully understand, at the single molecular level, of the physiological interactions of gold nanoparticles.[277,278] Therefore, the effort to study the potential effects of GNP and other types of nanoparticles in biological systems is urgently needed.[279,280]

There have been intensive studies of the cytotoxicity of GNP.[281-284] Most of work has focused on the nuclear transfection and targeting.[252] It was reported that GNP can easily enter the cell through endocytosis[285] or diffusion[281]. However, in most cases the GNP was rejected out of the nucleus.[283] Beside these two aspects, the influence on the immunological response of cells was also found to be a possible adverse effect.[286] All these studies were carried out at the cell level. To better understand how particles will interact with cell and tissues, the studies of protein-nanoparticle interactions and their biological consequences is necessary and helpful since the interaction can alter conformations, expose novel epitopes and disturb the function of the same protein.[287]

Fibrinogen is the scaffold of thrombus which is the direct cause of many diseases, such as heart attack, stroke and pulmonary embolism.[288] As is known, nanoparticles can easily enter human blood circulation system through different uptake routes, such as intravenous injection, inhale, and oral administration.[279,289] Reported studies showed that nanoparticles can affect pulmonary function[290,291]and induce its inflammation,[292] maybe further alter cardiovascular parameter for particulate pollution after translocation into the blood.[293]

Last section already discussed that fibrinogen self-assembled by firmly anchoring on gold surface through the Au-S bond,[294] and therefore GNP can possibly activate Fg to form the clot through a similar mechanism. To test our hypothesis in different perspectives, several characterization methods were applied to study the clot formation of Fg and GNP in vitro. From the SPR (surface Plasmon resonance) shift of GNP, the dissociation constant was deduced by

one bond-site model to illustrate how strong the complexes are. The measurement by DLS (Dynamic light scattering) intuitively gave out the size dependence on the concentration and time. AFM static and kinetic imagings were used to visualize the clot formation and thus confirmed the results from UV spectrum and DLS. Furthermore, the mechanism of the complex formation was attributed to the binding of the NPs and the distributed disulfide bonds in the Fg structure through Au-S interaction.

6.2.3 Experiment

Materials. Human fibrinogen was purchased from Sigma-Aldrich as lyophilized powder containing 68% protein and salts (~15% sodium citrate and ~25% sodium chloride). Over 96% protein is clottable. Stock solutions at a concentration of 0.8 mg/ml were prepared in pure water and incubated at 37 ºC for 30 min to fully dissolve the protein powder. All the protein solution was freshly prepared and used to ensure the biological activity. HAuCl4.xH2O (Alfa Aesar), Trisodium citrate (J. T. Baker), and all other reagents were used as received without further purification. The water used was ultra-pure water with conductivity of 18 MΩ/cm. 0.45 μm nylon syringe filter (Micron Separations Inc.), regenerated cellulose tubular membranes with nominal MWCO=3500 (Membrane Filtration Products, Inc.).

GNP synthesis. All glasswares used for preparation of colloids were thoroughly washed by aqua regia (volume ratio of HCl/ HNO_3=3:1), rinsed extensively with water, and then dried in oven prior to use. Gold colloids were prepared by sodium citrate reduction of gold salt as reported earlier.[295,296] Firstly, 200 mL of 1mM $HAuCl_4$ was heated to vigorous boiled under stirring in a round-bottomed flask fitted with a reflux condenser, and 20mL of 38.8mM sodium citrate solution was rapidly added to the solution. The solution was kept boiling for another 15 min and the color of the solution changed from pale yellow to deep red during the reaction. Then,

the solution was cooled to room temperature with continuing stirring and then filtered through 0.45 μm nylon filter. Finally, dialysis was used to remove the possible reactant residues in solution by regenerated cellulose membrane with nominal MWCO=3500 at 4 ºC for 48 h. The product was then stored at 4 ºC until further use.

Sample preparation. The concentration of GNP stock solution is 24.8 nM and its size is around 10 nm. Two different concentrations of GNP solution were used here. One is 10 fold diluted GNP solution with concentration of 2.48 nM, the other is the 32 fold diluted GNP solution with concentration of 0.775 nM. According to different volume ratio, GNP solutions are mixed with fg solution in water, with a series of fg concentrations of 0, 1.25, 2.5, 5, 10, 20, and 40 μg/ml in two GNP solutions (1 μg/mL is equal to 2.94 nM, concentration of stock solution is calculated from absorbance at 280 nm). In the static experiment, new cleaved MICA surface was incubated in the fg and GNP mixture for 30 min and directly imaged in water after rinsed by water for several times. For the dynamic experiment, the flow-cell technique was adopted here. Once the AFM was stable, several hundred micro liter of the fg and GNP mixture was injected into the liquid cell to observe the time-line change of the complexes on surface.

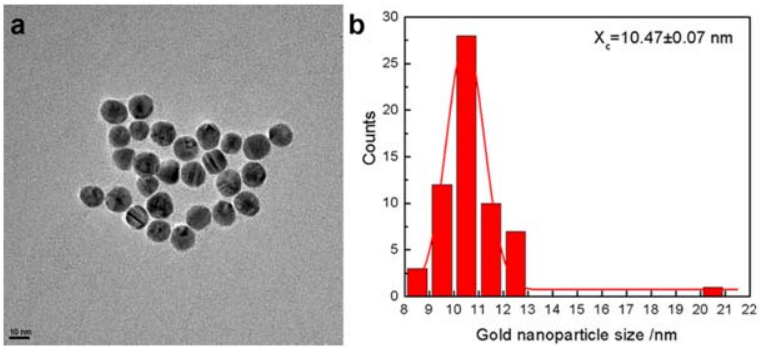

Figure 6.7 TEM images and statistical size analysis of gold nanoparticles. a) TEM image of gold nanoparticles (scale bar: 10 nm). b) Size distribution of the diameter of gold nanoparticles with the center value X_c*=10.47±0.07 nm*.

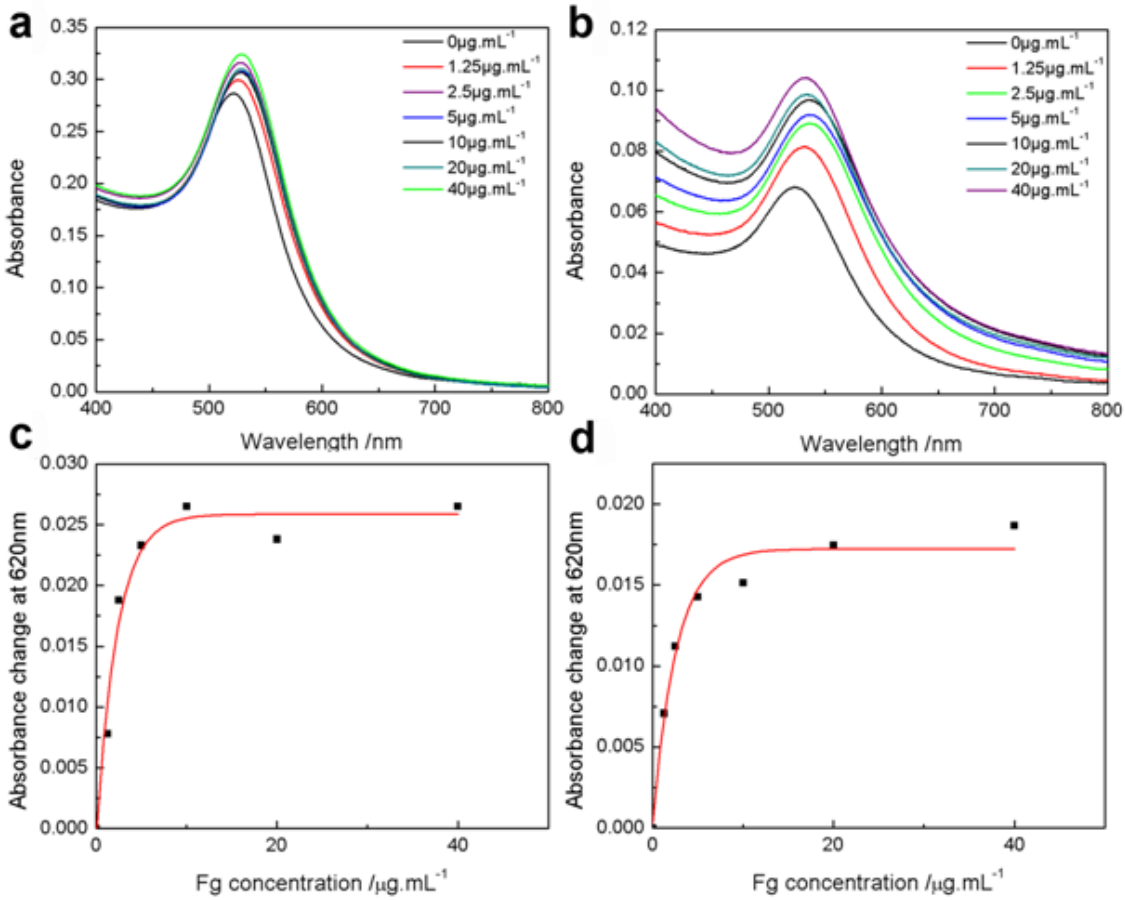

Figure 6.8 UV absorbance spectra of the mixture solutions and the dependence of its related SPR shift on the fg concentration. a) Absorbance curves of series of fg concentrations in 10 fold diluted GNP solutions, b) absorbance curves of series of fg concentrations in 32 fold diluted GNP solutions, c) The correlation curve between absorbance alteration at 620 nm and fg concentration in 10 fold diluted GNP solution. (The red line is the fitted curve) The calculated value of K_D is 1.96±0.21 μg/mL with R^2=0.994. d) The correlation curve between absorbance alteration at 620 nm and fg concentration in 32 fold diluted GNP solution. (The red line is the fitted curve) The calculated value of K_D is 1.57±0.25 μg/mL with R^2=0.987.

Characterization by TEM, UV, DLS, and AFM. The TEM images were obtained for evaporated drops of GNP solution on a carbon covered copper grid by (FEI Technai 20) operating at 200 kV. The absorption measurements were carried out at r.t. using UV-1700 Spectrophotometer from Shimadzu Scientific Instruments. ZetaPALS (zeta potential analyzer) from Brookhaven Instrument Corporation was applied to measure the hydration mean diameter of the complex in ambient condition at a scattering angle (θ) of 90º. The topography images were collected by AFM.

6.2.4 Results and discussions

TEM (Transmission Electron Microscopy) imaging

The size distribution of the GNP was determined by counting about 100 particles in TEM images. The typical TEM image of GNP and its size distribution are shown in ***Figure 6.7***. The most probable diameter of GNP is determined by the size distribution histogram to be 10.47 nm. The particles in this size were found to be able to transfer freely through multiple biological barrier,[297] such as blood–brain barrier[298] and blood–retinal barrier[299].

UV absorbance spectrum

The absorption properties of the mixture were measured immediately after vortex. Once Fg was added into GNP solution, the color of GNP solution immediately changed from light red to crimson, indicating a shift of the SPR (surface Plasmon resonance) peak. The SPR peak shift can be caused by many factors, such as medium, shape and size.[278] However, it is clear that the interaction between GNP and Fg is a spontaneous process based on the observations.

It can be shown by UV absorbance spectra experiments and through calculations according to its UV-vis absorption[300] that GNP induced particle size alteration is the dominant factor for SPR shift. Firstly, bonding between Fg molecules and GNPs would cause the size

changing and indeed obvious SPR shifts were observed from the UV absorption properties when GNP solution was mixed with different Fg concentrations (***Figure 6.8*** a and b). This indicates that the introduction of Fg caused the formation of the complex particle with larger size even for highly diluted GNP solution (the concentration of pM level). Furthermore increasing Fg concentration brought about larger SPR peak shift (***Figure 6.8*** a and b). In order to find out how strong the bonding between GNP and Fg is, the dissociation constant was estimated from the relation between SPR shift and Fg concentration based on a one-site bonding model:[301,302]

$\Delta A = \frac{A_{\max}[c]}{[c]+K_D}$ Where ΔA is the absorbance change at 620nm, A_{max} is the maximum absorbance change at 620nm, *[c]* is the fg concentration, and K_D is the equilibrium dissociation constant for GNP and fg. Both fitting curves produced the dissociation constant at nM level: 1.96±0.21 μg/mL with R^2=0.994 for 10 fold diluted GNP solution and 1.57±0.25 μg/mL with R^2=0.987 for 32 fold diluted GNP solution (shown in ***Figure 6.8*** c and d). The small dissociation constant indicates strong interaction between Fg and GNP, which is consistent with the origin of the binding. Besides the two GNP solution used here, more diluted GNP solution (128 fold diluted, 0.194nM) were tested, which also showed obvious SPR shift. However, due to the very low absorbance of GNP solution (≤0.02) and sensitivity limitation of UV photospectrometer, the SPR shifts didn't show good exponential relation with fg concentration (data not reported). Higher concentrations of Fg (up to several hundred micro-gram per milliliter) in the mixture were also tested and visible red color precipitations were observed in the solution. Hence, the absorbance would not be accurate at high concentrations of over hundred micro-gram per milliliter and therefore the data were not shown here.

DLS (Dynamic Light Scattering)

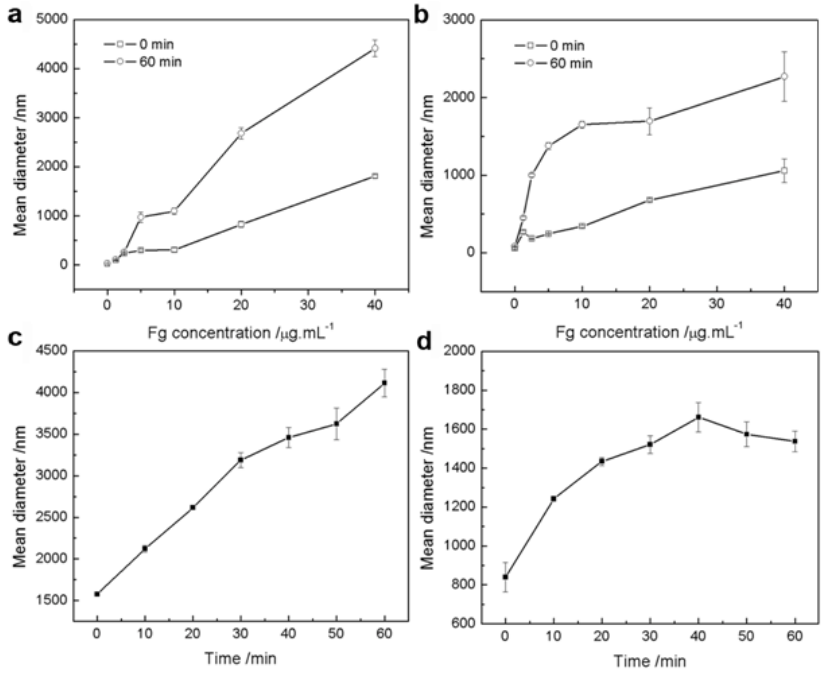

Figure 6.9 Mean diameters from DLS measurement. a) 10 fold diluted GNP solution and b) 32 fold diluted GNP solution with series of fg concentration from the range of 0 to 40 μg/mL. For each sample, it was measured twice. One is done right after the mixture (the square dotted line) and the other is measured after 1 h (the circle dotted line). The time dependent measurement for c) the 10 fold diluted GNP solution and d) 32 diluted GNP solution with fg concentration of 40 μg/mL.

The purpose of DLS experiments was to confirm that the SPR peak shift is mainly caused by the size effect and the formation of the larger size complexes with GNP was due to the introduction of Fg in solution. It is known that the decay time of photon intensity fluctuation in DLS measurement is related to the diffusion constants and therefore, the sizes of the particles. The solutions of Fg and GNP mixture were freshly prepared and measured immediately at 0 min and 60 min by DLS. The measured diameters for the pure GNP solutions are in the range of

25~35 nm, larger than those measured from TEM. This is expected because the measured diameter in photon correlation spectroscopy (PCS) is the hydrodynamic diameter (the particle diameter plus the double layer thickness). As shown in ***Figure 6.9*** a) and b), the size increases of the complex are getting much bigger with the increasing of Fg concentration in both GNP concentrations. The mean diameter here is the average diameter which is measured by the intensity of light scattered by each particle. For the concentrations of Fg over 5 μg/mL, the increase of diameter is more obvious compared to that at lower concentrations. When Fg concentration is around 40 μg/mL, the size reached micro-meter level. The measurements taken at 60 min shows tremendous size enlargement compared to those at 0 min. The time-dependent size changes were shown in ***Figure 6.9*** c) and d), which indicates that the size of GNP and Fg complex was developed with time. Depending on the concentration of GNP solution, the curve of time-dependent mean diameter finally reached a plateau in 30~40 min as shown in ***Figure 6.9*** c) and d), meaning most free GNPs in solution were consumed up and the clot formation process was thus stopped. Based on the experimental observations, a conclusion can be drawn that the size change is the dominant reason for the SPR peak shift and the larger concentration of the GNP solution, the bigger the size of the complexes and the faster the growing rate of the size. This might be a danger signal for the GNP clinical application since the normal Fg concentration in blood is 20 ~45 mg/mL. If GNP accidentally goes into the blood circulation, it might lead to the clot formation, which is the cause of thromboembolic disease.

In-situ AFM imaging

AFM experiments were performed to visualize the formation of GNP induced fg coagulation in situ. In the static experiment, several concentrations of fg in the GNP solutions were investigated. When the concentration of Fg exceeded 10 μg/mL, the Fg covered the whole

surface thus making it impossible to distinguish single complex of fg with GNP (The data was not shown here). For all the cases shown in the first row of ***Figure 6.10***, there were many small pieces of complexes observed on MICA. These small pieces were the most popular distribution on the MICA surface. The sizes of small pieces were measured to be about 100~200 nm for 2.5 and 5 μg/mL and 200~500 nm for 10 μg/mL. The conformations and sizes of these complexes are totally different with the pure Fg and GNP on MICA surface respectively shown in ***Figure 6.2*** *a* and ***6.11***, indicating surface induced differences of Fg adsorptions. Besides the small pieces, the much bigger coagulations of fg and GNP were formed for all the concentrations shown in the second row of ***Figure 6.10***. The only difference among them lies in the sizes of these coagulations.

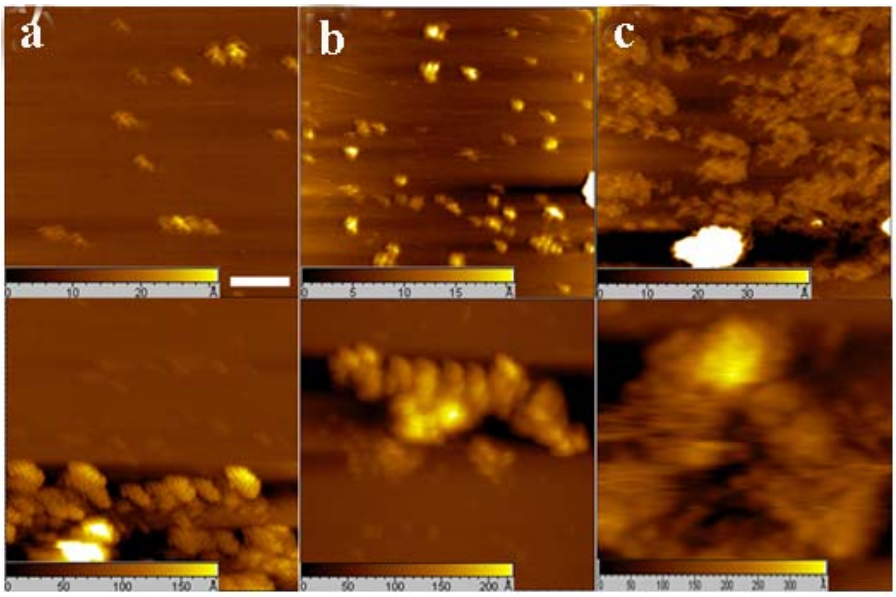

Figure 6.10 The AFM topographical images of the fg and GNP complexes in the 10 fold diluted GNP solution. The images in the first pane show the most popular complexes of fg and GNP and some large size complexes of fg and GNP were shown in the second pane. a) 2.5 μg/mL fg, b) 5 μg/mL fg, and c) 10 μg/mL fg. (Scale bar: 200 nm)

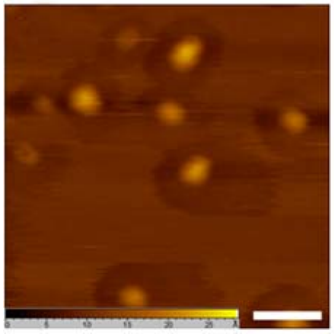

Figure 6.11 The topographical image of GNP on MICA surface (scale bar :50 nm)

To further confirm the time dependent growing process of the coagulation, a time-line imaging was carried out for the 10 fold GNP solution with 2.5 μg/mL fg. Once the AFM was stable, around three hundreds of micro liter of the fg and GNP mixture was injected into the liquid cell while imaging. In the process, there were more small pieces anchored on MICA surface and a big piece gradually formed with the size of 400~500 nm in length, shown in ***Figure 6.12***. This result agrees with those from UV, DLS measurements and therefore confirmed that the mean diameter of the fg and GNP complex grows with time to assemble into the bigger coagulation.

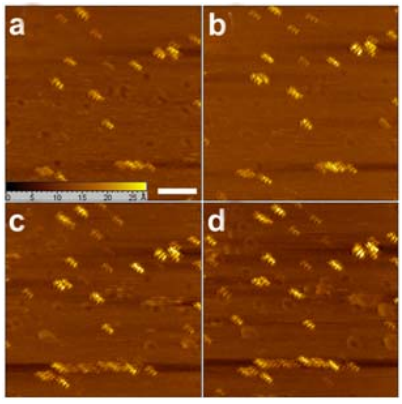

Figure 6.12 The time-laps images of the complexes formation in the 10 fold GNP diluted solution with 2.5 μg/mL fg. The interval between the two is about 6 min. a) 0 min, b) 6 min, c) 12 min, and d) 18 min. (scale bar: 200 nm)

Fg Clotting Mechanism

It has been shown that fg can interact with gold through the Au-S bond because of the widely distributed Cys residues.[294,303,304] Through scrutinization of fg sequence,[254] it was found that there were 5 Cys residues in the α chain of fg, 11 Cys residues in the β chain and 10 Cys residues in the γ chain. Most of them form disulfide bonds to keep the protein structure intact, only a few of free Cys residues exist in the β and γ chain of D domain. Several disulfide bonds locate at the amino-terminal of the chains in E domain, such as: symmetrical disulfide bonds of γ Cys^{8} and Cys^{9}. Some of them flank the N-terminal of coil-coil region, for example: the unsymmetrical one between α Cys^{45} and γ Cys^{23}. The others flank the C-terminal of coil-coil region, for instance: the unsymmetrical one between β Cys and α Cys^{165}.[257,264]

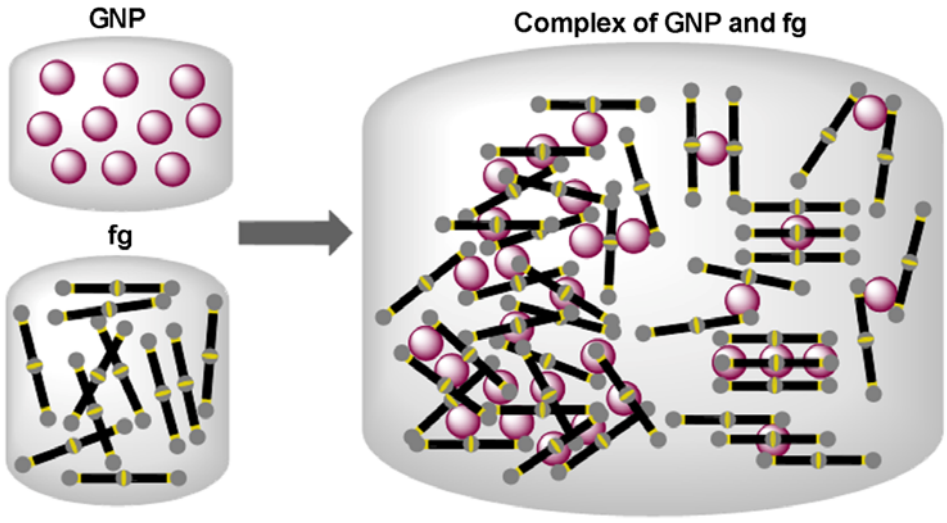

Figure 6.13 The configuration of the complexes formation of the GNP and fg. Yellow denotes the available disulfide bonds in Fg structure.

Through visually investigating the fg crystal structure, it was found that most of free Cys residues in D domain hide in the loop, hence not unavailable for the formation of Au-S bonds.

Comparatively, most of these disulfide bonds are exposed outside, which makes them accessible to GNPs.[294] Moreover, for GNP with 10 nm in diameter the disulfide bonds in E domain and flank part at N-terminal only can be taken as one interaction site since the size of E domain is about 5 nm. Besides, the flank part at C-terminal with disulfide bonds is the other possible interaction sites. Hence, ***Figure 6.13*** schematically denotes the possible binding sites as the yellow stripes in fg molecules, and it also shows some of the configurations of the complexes formed through the interaction between the binding sites and GNP. Finally, it is believed that the originality of the complex formation process is from the interactions between GNP and disulfide bonds in the E domain and flank part at C-terminal and N-terminal.

6.2.5 Conclusion

Through UV, DLS and AFM, it was demonstrated that the adsorption of fg on GNP induces the coagulation of fg and the SPR shift of GNP. The change of absorption was mainly attributed to the size change, which is still prominent even for concentrations down to sub-nM. Furthermore, this coagulation process occurs spontaneously and rapidly when fg meets GNP. From the fitting of SPR shift, it was also found that the dissociation constant is at nM level, which indicates the strong bonding between fg and GNP. The strong binding may indicate that the clot formed by Fg and GNP could stand shear force of blood circulation, which need further studies *in vivo*. In addition, the size of clot was time- and concentration- dependent. It was observed from DLS measurement that the size of clot can be μm level when Fg concentration is over 10 μg/mL. The growing size of the clot by the time would be an important aspect worthy of consideration in the possible GNP clinical application, which may induce the blockage of blood circulation. The possible mechanism of the clot formation lies in the disulfide bonds in the E

domain and flank part at C-terminal and N-terminal which could bond with GNP through Au-S bonds. This mechanism is also consistent with the nM-level dissociation constant.

CHAPTER 7

SUMMARY AND OUTLOOK

7.1 Summary

For AFM based single molecule study, there are three pivotal points: how to attach the molecule of interest to one or two surfaces; how to control tip movement; and how to translate the obtained force information into common used kinetic and thermodynamic terms. In all my studies, this logic way is followed.

To achieve the purposes of imaging and force spectroscopy, several organosulfur compounds and heterofunctional polyethylene glycol (PEG) derivatives were synthesized for gold substrate and AFM probe functionalization. The organosulfur compounds carry with thiol or disulfide moiety in one end for gold attachment and active modules for molecule coupling in the other end including active ester, triacetic acid or biotin. The heterofunctional PEG derivative for tip functionalization bears bromoacetyl ending group, which is reactive with thiol group on organosilane decorated tip surface, and biotin in the other end.

Based on these chemical derivatization strategies, both AFM magnetic AC imaging and force spectroscopy techniques were applied simultaneously to study several interesting systems, such as: ricin and its antibody, EphA2 and its peptide ligands, organomicelle, and fibrinogen.

1) In the ricin study, the anti-ricin decorated AFM probe was applied to perform the detection and fundamental interaction for the ricin immobilized on gold surface. The detection sensitivity of fg/mL level can be easily achieved by AFM recognition imaging and the linear relationship between unbinding force and force loading rate revealed that

the interaction between ricin and anti-ricin follows Bell's one-barrier model for the force loading rate from 0.2 to 100 nN/s. From Jarzynski equality, it was estimated that unbinding free energy for ricin pair is around 86 k_BT.

2) In the EphA2 related study, AFM recognition image and force spectroscopy were applied to study the competitive bindings between its natural ligand, Ephrin, and artificial ligands, polypeptides, for preliminary ligand screening. Through employing the Bell's model and recognition event counting, the kinetic and equilibrium parameters can be inferred, such as: dissociation rate constant (k_{off}), association rate constant (k_{on}) and dissociation constant (K_D). The parameters indicate that peptide has weaker binding affinity (μM) with EphA2 comparing to Ephrin (nM). Besides, peptides share the similar binding sites with Ephrin and tyrosine residue in the N-terminal of peptide is paramount for the binding.
3) A fundamental new concept of AFM recognition technique was accomplished, which is based on the metal free 'click chemistry' between dibenzocyclooctynol (DIBO) and azide. Based on this method, the surface functional groups and assembly strengths can be investigated for the organomicelles with different compositions and loadings through pulling out polymer strands from the assembly. It was discovered that the chemical modification by organosilane can offer enough DIBO moiety on tip surface and the stabilities of organomicelles loaded with Doxorubicin or Rhodamine B are stronger than the micelles without loading, telling from the 'pull-out' force and stretch distance.
4) The conformation differences of fibrinogen (fg) on various surfaces, e.g., mica, HOPG and gold surface were studied. It was found that fg can self-assembly on gold surface in longitude and transverse direction without any addition of clotting factors, such as

thrombin, which is essentially distinct with fg adsorption on mica and HOPG. Through scrutinize the fg structure, it was believed that the disulfide bridges inside the fg is the main impetus for the assembly process and its triggered intermolecular interactions, such as: 'αC-domain' 'D:D' and 'γ_{XL}', are helpful to stabilize the assembly structure. Under the enlightenment of this observation, the fg clot induced by gold nanoparticle (GNP) was further investigated by several methods including UV spectrum, dynamic light scattering (DLS) and AFM. The dissociation constant of fg-GNP complex at nM level indicated the strong binding between fg and GNP and the size of clot can quickly increase to μm level when fg concentration is over 10 μg/mL. The behind mechanism of the clot formation lies in the disulfide bonds in the E domain and flank part at C-terminal and N-terminal which could bond with GNP through Au-S bonds.

In a word, the properly designed chemical modifications are a prerequisite for reliable imaging and force spectroscopy. The recorded topography images can visualize the shape, size, distribution and organization of the studied objects on surface; the collected recognition images provide directly evidences and localizations for noncovalent interactions between varieties of macromolecules. The results from force spectroscopy further quantitively characterized the strength of these noncovalent interactions, termed as 'rupture force' with the unit of pN. Through employing the Bell's model and Jarzynski equality, the force information can be translated into kinetic and thermodynamic parameters, such as: dissociation rate constant (k_{off}), association rate constant (k_{on}) and dissociation constant (K_D), in which the biologists and chemists are mostly interested.

7.2 Outlook

Single molecule studies have opened up new avenues of chemistry, material and especially biological research. The rapidly growing number of applications illustrates the power and success of single molecule studies. Meanwhile, great challenges need to be addressed. One of the primary difficulties is the want of feasible ways to characterize the biological molecules and processes in their natural conditions, such as discrete cells or cells on tissues and organs. With only a few notable exceptions[234], single molecule studies have mainly focused on *in-vitro* measurements of purified proteins on solid-supported surfaces. Performing the same or similar experiments *in vivo* will offer an unparalleled view of how the conformation of individual protein changes on the cell membrane by the applied perturbations, and how the interaction between the ligand and receptor triggers the cascaded cell response at the molecular level.

On one hand, the cell surface is crowded with many kinds of proteins, polysaccharides, and lipids. The specific molecules or interactions are required to be differentiated from others. The combination of AFM based techniques with other single molecule methods, in particular single molecule fluorescence spectroscopy, is a possible solution for this problem. However, the labeling of fluorescent tag will inevitably modify the original status of molecules structurally and/or functionally. Alternatively, the characterization of bio-molecules embedded in the artificial lipid membrane will provide more meaningful data than on solid supporter. Based on the knowledge of lipid membranes, the measurements on cell with some gene knock-outs or overexpression would be a viable way to simplify the inhomogeneous condition of the cell surface. The density of molecules under investigation can be greatly increased on the mutated cell surface in order to facilitate the measurements.

On the other hand, the specific, non-invasive and fast single molecule measurements also depend on the advances in instrumentation. Current AFM based image and force spectroscopy techniques are suffering from noisy feedbacks and large cantilever with high stiffness. To perform the fast measurements with high specificity and less perturbation, smaller cantilevers with sharp tip radius, high Q value (Q value describes how under-damped an oscillator or resonator is) and chemical stability are greatly desirable. The small size of the probe will enable high resonance frequency and small forces, while reducing hydrodynamic damping in liquid. The high resonance frequency allows fast scanning rates and small forces can decrease the perturbations or deformation of sample when observing the dynamic processes or the structures of bio-molecules. The high speed AFM system equipped with small cantilever-tip was successfully applied to observe the movement of single myosin molecule along the actin filament at certain video rate.[97] The feedback systems with high sensitivity and low inherent noise, such as magnetic[305] and optical feedback[306], will support the fast and specific scan properly. Further, versatile tip movement modes could be powerful modules to screen out the nonspecific interactions.[106] In addition, further development of a new type of AFM tip, FIRAT (Force sensing Integrated Readout and Active Tip)[307], can improve the imaging speed to chase the bioprocesses and record movies of such processes.

Through all these improvements, it is anticipated that more applications of AFM based image and force spectroscopy techniques will come out, especially in biological fields. They definitely will deepen our understanding in the mechanics of biological systems, colloid systems, and polymeric materials.

REFERENCE

(1) Deniz, A. A.; Mukhopadhyay, S.; Lemke, E. A. *J. R. Soc. Interface* **2008**, *5*, 15-45.

(2) Tamarat, P.; Maali, A.; Lounis, B.; Orrit, M. *J. Phys. Chem. A* **2000**, *104*, 1-16.

(3) Ashkin, A.; Dziedzic, J. M.; Bjorkholm, J. E.; Chu, S. *Opt. Lett.* **1986**, *11*, 288-290.

(4) Strick, T.; Allemand, J. F.; Croquette, V.; Bensimon, D. *Prog. Biophys.Mol. Bio* **2000**, *74*, 115-140.

(5) Binnig, G.; Quate, C. F.; Gerber, C. *Phys. Rev. Lett.* **1986**, *56*, 930-933.

(6) Cluzel, P.; Lebrun, A.; Heller, C.; Lavery, R.; Viovy, J. L.; Chatenay, D.; Caron, F. *Science* **1996**, *271*, 792-794.

(7) Evans, E.; Ritchie, K.; Merkel, R. *Biophys. J.* **1995**, *68*, 2580-2587.

(8) Smith, S. B.; Finzi, L.; Bustamante, C. *Science* **1992**, *258*, 1122-1126.

(9) Kim, S. J.; Blainey, P. C.; Schroeder, C. M.; Xie, X. S. *Nat. Methods* **2007**, *4*, 397-399.

(10) Neuman, K. C.; Lionnet, T.; Allemand, J. F. *Ann. Rev. Mater. Res.* **2007**, *37*, 33-67.

(11) Neuman, K. C.; Nagy, A. *Nat. Methods* **2008**, *5*, 491-505.

(12) Block, S. M.; Goldstein, L. S. B.; Schnapp, B. J. *Nature* **1990**, *348*, 348-352.

(13) Svoboda, K.; Block, S. M. *Cell* **1994**, *77*, 773-784.

(14) Svoboda, K.; Schmidt, C. F.; Schnapp, B. J.; Block, S. M. *Nature* **1993**, *365*, 721-727.

(15) Abbondanzieri, E. A.; Greenleaf, W. J.; Shaevitz, J. W.; Landick, R.; Block, S. M. *Nature* **2005**, *438*, 460-465.

(16) Wang, M. D.; Schnitzer, M. J.; Yin, H.; Landick, R.; Gelles, J.; Block, S. M. *Science* **1998**, *282*, 902-907.

(17) Herbert, K. M.; La Porta, A.; Wong, B. J.; Mooney, R. A.; Neuman, K. C.; Landick, R.; Block, S. M. *Cell* **2006**, *125*, 1083-1094.

(18) Neuman, K. C.; Abbondanzieri, E. A.; Landick, R.; Gelles, J.; Block, S. M. *Cell* **2003**, *115*, 437-447.

(19) Shaevitz, J. W.; Abbondanzieri, E. A.; Landick, R.; Block, S. M. *Nature* **2003**, *426*, 684-687.

(20) Friese, M. E. J.; Nieminen, T. A.; Heckenberg, N. R.; Rubinsztein-Dunlop, H. *Nature* **1998**, *394*, 348-350.

(21) Deufel, C.; Forth, S.; Simmons, C. R.; Dejgosha, S.; Wang, M. D. *Nat. Methods* **2007**, *4*, 223-225.

(22) La Porta, A.; Wang, M. D. *Phys. Rev. Lett.* **2004**, *92*.

(23) Koster, D. A.; Croquette, V.; Dekker, C.; Shuman, S.; Dekker, N. H. *Nature* **2005**, *434*, 671-674.

(24) Koster, D. A.; Palle, K.; Bot, E. S. M.; Bjornsti, M. A.; Dekker, N. H. *Nature* **2007**, *448*, 213-217.

(25) Bausch, A. R.; Moller, W.; Sackmann, E. *Biophys. J.* **1999**, *76*, 573-579.

(26) Keller, M.; Schilling, J.; Sackmann, E. *Rev. Sci. Instrum.* **2001**, *72*, 3626-3634.

(27) Binnig, G.; Garcia, N.; Rohrer, H. *Phys. Rev. B* **1985**, *32*, 1336-1338.

(28) Dai, P.; Wang, S. K.; Taub, H.; Buckley, J. E.; Ehrlich, S. N.; Larese, J. Z.; Binnig, G.; Smith, D. P. E. *Phys. Rev. B* **1993**, *47*, 7401-7407.

(29) Garcia, R.; Magerle, R.; Perez, R. *Nat. Mater.* **2007**, *6*, 405-411.

(30) Magonov, S. N.; Elings, V.; Papkov, V. S. *Polymer* **1997**, *38*, 297-307.

(31) Tamayo, J.; Garcia, R. *Appl. Phys. Lett.* **1997**, *71*, 2394-2396.

(32) Stroh, C.; Wang, H.; Bash, R.; Ashcroft, B.; Nelson, J.; Gruber, H.; Lohr, D.; Lindsay, S. M.; Hinterdorfer, P.; Quate, C. F. *Proc. Nat. Acad. Sci. U.S.A.* **2004**, *101*, 12503-12507.

(33) Raab, A.; Han, W. H.; Badt, D.; Smith-Gill, S. J.; Lindsay, S. M.; Schindler, H.; Hinterdorfer, P. *Nat. Biotechnol.* **1999**, *17*, 902-905.

(34) Chen, G. J.; Ning, X. G.; Park, B.; Boons, G. J.; Xu, B. Q. *Langmuir* **2009**, *25*, 2860-2864.

(35) Stroh, C. M.; Ebner, A.; Geretschlager, M.; Freudenthaler, G.; Kienberger, F.; Kamruzzahan, A. S. M.; Smith-Gil, S. J.; Gruber, H. J.; Hinterdorfer, P. *Biophys. J.* **2004**, *87*, 1981-1990.

(36) Chen, G. J.; Zhou, J. F.; Park, B.; Xu, B. Q. *Appl. Phys. Lett.* 2009, 95.

(37) Lin, L.; Hom, D.; Lindsay, S. M.; Chaput, J. C. *J. Am. Chem. Soc.* **2007**, *129*, 14568-+.

(38) Grandbois, M.; Beyer, M.; Rief, M.; Clausen-Schaumann, H.; Gaub, H. E. *Science* **1999**, *283*, 1727-1730.

(39) Fernandez, J. M.; Li, H. B. *Science* **2004**, *303*, 1674-1678.

(40) Lee, G. U.; Chrisey, L. A.; Colton, R. J. *Science* **1994**, *266*, 771-773.

(41) Schwaiger, I.; Kardinal, A.; Schleicher, M.; Noegel, A. A.; Rief, M. *Nat. Struct. Mol. Biol.* **2004**, *11*, 81-85.

(42) Wright, C. F.; Lindorff-Larsen, K.; Randles, L. G.; Clarke, J. *Nat. Struct. Mol. Biol.* **2003**, *10*, 658-662.

(43) Wiita, A. P.; Perez-Jimenez, R.; Walther, K. A.; Grater, F.; Berne, B. J.; Holmgren, A.; Sanchez-Ruiz, J. M.; Fernandez, J. M. *Nature* **2007**, *450*, 124-+.

(44) Scheuring, S.; Boudier, T.; Sturgis, J. N. *J. Struct. Biol.* **2007**, *159*, 268-276.

(45) Sulchek, T.; Yaralioglu, G. G.; Quate, C. F.; Minne, S. C. *Rev. Sci. Instrum.* **2002**, *73*, 2928-2936.

(46) Butt, H. J.; Siedle, P.; Seifert, K.; Fendler, K.; Seeger, T.; Bamberg, E.; Weisenhorn, A. L.; Goldie, K.; Engel, A. *J. Microsc.-Oxf.* **1993**, *169*, 75-84.

(47) Saulson, P. R. *Phys. Rev. D* **1990**, *42*, 2437-2445.

(48) Tranchida, D.; Piccarolo, S.; Deblieck, R. A. C. *Meas. Sci. Technol.* **2006**, *17*, 2630-2636.

(49) Butt, H. J.; Jaschke, M. *Nanotechnol.* **1995**, *6*, 1-7.

(50) Kobayashi, K.; Yamada, H.; Matsushige, K. *Rev. Sci. Instrum.* **2009**, *80*, 8.

(51) Alessandrini, A.; Facci, P. *Meas. Sci. Technol.* **2005**, *16*, R65-R92.

(52) Giessibl, F. J. *Mater. Today* **2005**, *8*, 32-41.

(53) García, R.; Pérez, R. *Surf. Sci. Rep.* **2002**, *47*, 197-301.

(54) Müller, D. J.; Fotiadis, D.; Scheuring, S.; Müller, S. A.; Engel, A. *Biophys. J.* **1999**, *76*, 1101-1111.

(55) San Paulo, A.; García, R. *Biophys. J.* **2000**, *78*, 1599-1605.

(56) Schabert, F.; Henn, C.; Engel, A. *Science* **1995**, *268*, 92-94.

(57) Yamamoto, D.; Nagura, N.; Omote, S.; Taniguchi, M.; Ando, T. *Biophys. J.* **2009**, *97*, 2358-2367.

(58) Scheuring, S.; MÜLler, D. J.; Ringler, P.; Heymann, J. B.; Engel, A. *J. Microsc.* **1999**, *193*, 28-35.

(59) Seelert, H.; Poetsch, A.; Dencher, N. A.; Engel, A.; Stahlberg, H.; Muller, D. J. *Nature* **2000**, *405*, 418-419.

(60) Muller, D.; Baumeister, W.; Engel, A. *J. Bacteriol.* **1996**, *178*, 3025-3030.

(61) Scheuring, S.; Sturgis, J. N. *Science* **2005**, *309*, 484-487.

(62) Darst, S. A.; Ahlers, M.; Meller, P. H.; Kubalek, E. W.; Blankenburg, R.; Ribi, H. O.; Ringsdorf, H.; Kornberg, R. D. *Biophys. J.* **1991**, *59*, 387-396.

(63) Gonçalves, R. P.; Bernadac, A.; Sturgis, J. N.; Scheuring, S. *J. Struct. Biol.* **2005**, *152*, 221-228.

(64) Garcia, R.; oacute; mez, C. J.; Martinez, N. F.; Patil, S.; Dietz, C.; Magerle, R. *Phys. Rev. Lett.* **2006**, *97*, 016103.

(65) Martínez, N. F.; García, R. *Nanotechnol.* **2006**, *17*, S167.

(66) Xu, W.; Wood-Adams, P. M.; Robertson, C. G. *Polymer* **2006**, *47*, 4798-4810.

(67) Leonenko, Z. V.; Finot, E.; Ma, H.; Dahms, T. E. S.; Cramb, D. T. *Biophys. J.* **2004**, *86*, 3783-3793.

(68) Needham, D.; Evans, E. *Biochemistry* **1988**, *27*, 8261-8269.

(69) Tokumasu, F.; Jin, A. J.; Feigenson, G. W.; Dvorak, J. A. *Ultramicroscopy*, *97*, 217-227.

(70) Xie, A. F.; Yamada, R.; Gewirth, A. A.; Granick, S. *Phys. Rev. Lett.* **2002**, *89*, 246103.

(71) Charrier, A.; Thibaudau, F. *Biophys. J.* **2005**, *89*, 1094-1101.

(72) Suo, Z.; Yang, X.; Avci, R.; Kellerman, L.; Pascual, D. W.; Fries, M.; Steele, A. *Langmuir* **2006**, *23*, 1365-1374.

(73) Tsao, Y.; Evans, D.; Wennerstrom, H. *Science* **1993**, *262*, 547-550.

(74) Biggs, S.; Mulvaney, P. *J. Chem. Phys.* **1994**, *100*, 8501-8505.

(75) Noy, A.; Vezenov, D. V.; Lieber, C. M. *Annu. Rev. Mater. Sci.* **1997**, *27*, 381-421.

(76) Nuzzo, R. G.; Allara, D. L. *J. Am. Chem. Soc.* **1983**, *105*, 4481-4483.

(77) Bain, C. D.; Troughton, E. B.; Tao, Y. T.; Evall, J.; Whitesides, G. M.; Nuzzo, R. G. *J. Am. Chem. Soc.* **1989**, *111*, 321-335.

(78) Green, J.-B. D.; McDermott, M. T.; Porter, M. D.; Siperko, L. M. *J. Phys. Chem.* **1995**, *99*, 10960-10965.

(79) Pierce, M.; Stuart, J.; Pungor, A.; Dryden, P.; Hlady, V. *Langmuir* **1994**, *10*, 3217-3221.

(80) Noy, A.; Frisbie, C. D.; Rozsnyai, L. F.; Wrighton, M. S.; Lieber, C. M. *J. Am. Chem. Soc.* **1995**, *117*, 7943-7951.

(81) Frisbie, C. D.; Rozsnyai, L. F.; Noy, A.; Wrighton, M. S.; Lieber, C. M. *Science* **1994**, *265*, 2071-2074.

(82) Noy, A.; Sanders, C. H.; Vezenov, D. V.; Wong, S. S.; Lieber, C. M. *Langmuir* **1998**, *14*, 1508-1511.

(83) Sinniah, S. K.; Steel, A. B.; Miller, C. J.; Reutt-Robey, J. E. *J. Am. Chem. Soc.* **1996**, *118*, 8925-8931.

(84) Vezenov, D. V.; Noy, A.; Rozsnyai, L. F.; Lieber, C. M. *J. Am. Chem. Soc.* **1997**, *119*, 2006-2015.

(85) Kienberger, F.; Ebner, A.; Gruber, H. J.; Hinterdorfer, P. *Acc. Chem. Res.* **2006**, *39*, 29-36.

(86) Hinterdorfer, P.; Dufrene, Y. F. *Nat. Meth.* **2006**, *3*, 347-355.

(87) Lin, L.; Fu, Q.; Williams, B. A. R.; Azzaz, A. M.; Shogren-Knaak, M. A.; Chaput, J. C.; Lindsay, S. *Biophys. J.* **2009**, *97*, 1804-1807.

(88) Lin, L.; Wang, H.; Liu, Y.; Yan, H.; Lindsay, S. *Biophys. J.* **2006**, *90*, 4236-4238.

(89) Ludwig, M.; Dettmann, W.; Gaub, H. E. *Biophys. J.* **1997**, *72*, 445-448.

(90) Kodera, N.; Kinoshita, T.; Ito, T.; Ando, T. *Adv. Exp. Med. Biol.* **2003**, *538*, 119-127.

(91) Ando, T.; Uchihashi, T.; Kodera, N.; Yamamoto, D.; Miyagi, A.; Taniguchi, M.; Yamashita, H. *Pflügers Arch.- Eur. J. Physiol.* **2008**, *456*, 211-225.

(92) Fukuma, T.; Kimura, M.; Kobayashi, K.; Matsushige, K.; Yamada, H. *Rev. Sci. Instrum.* **2005**, *76*, 8.

(93) Schaffer, T. E. *Nanotechnol.* **2005**, *16*, 664-670.

(94) Humphris, A. D. L.; Miles, M. J.; Hobbs, J. K. *Appl. Phys. Lett.* **2005**, *86*, 3.

(95) Hansma, P. K.; Schitter, G.; Fantner, G. E.; Prater, C. *Science* **2006**, *314*, 601-602.

(96) Ando, T.; Kodera, N.; Takai, E.; Maruyama, D.; Saito, K.; Toda, A. *Proc. Natl. Acad. Sci. U.S.A.* **2001**, *98*, 12468-12472.

(97) Kodera, N.; Yamamoto, D.; Ishikawa, R.; Ando, T. *Nature*, *468*, 72-76.

(98) Bhushan, B.; Hinterdorfer, P.; Ebner, A.; Gruber, H.; Kapon, R.; Reich, Z. In *Springer Handbook of Nanotechnology*; Springer Berlin Heidelberg, 2004; p 763-785.

(99) Flyvbjerg, F.; Jülicher, F.; Ormos, P.; David, F.; Evans, E.; Williams, P. In *Physics of bio-molecules and cells. Physique des biomolécules et des cellules*; Springer Berlin Heidelberg, 2002; Vol. 75, p 145-204.

(100) Barattin, R.; Voyer, N. *Chem. Commun.* **2008**, 1513-1532.

(101) Myhra, S.; Riviere, J. C. *Handbook of Surface and Interface Analysis: methods for problem solving*; Marcel Dekker, 1998.

(102) Gibson, C. T.; et al. *Nanotechnol.* **1996**, *7*, 259.

(103) Cumpson, P. J.; Zhdan, P.; Hedley, J. *Ultramicroscopy* **2004**, *100*, 241-251.

(104) Janovjak, H.; Struckmeier, J.; Müller, D. J. *Eur. Biophys. J.* **2005**, *34*, 91-96.

(105) Evans, E. *Faraday Discuss.* **1999**, *111*, 1-16.

(106) Xu, B. *Small* **2007**, *3*, 2061-2065.

(107) Chen, F.; Zhou, J. F.; Chen, G. J.; Xu, B. Q. *IEEE Sens. J.* **2010**, *10*, 485-491.

(108) Zhou, J. F.; Chen, G. J.; Xu, B. Q. *J. Phys. Chem. C* **2010**, *114*, 8587-8592.

(109) Bell, G. *Science* **1978**, *200*, 618-627.

(110) Evans, E.; Berk, D.; Leung, A. *Biophys. J.* **1991**, *59*, 838-848.

(111) Evans, E.; Ritchie, K. *Biophys. J.* **1999**, *76*, 2439-2447.

(112) Jarzynski, C. *Phys. Rev. Lett.* **1997**, *78*, 2690-2693.

(113) Jarzynski, C. *Phys. Rev. E* **1997**, *56*, 5018-5035.

(114) Hummer, G.; Szabo, A. *Proc. Natl. Acad. Sci. U. S. A.* **2001**, *98*, 3658-3661.

(115) Liphardt, J.; Dumont, S.; Smith, S. B.; Tinoco, I.; Bustamante, C. *Science* **2002**, *296*, 1832-1835.

(116) Hummer, G.; Szabo, A. *Acc. Chem. Res.* **2005**, *38*, 504-513.

(117) Preiner, J.; Janovjak, H.; Rankl, C.; Knaus, H.; Cisneros, D. A.; Kedrov, A.; Kienberger, F.; Muller, D. J.; Hinterdorfer, P. *Biophys. J.* **2007**, *93*, 930-937.

(118) Ratto, T. V.; Langry, K. C.; Rudd, R. E.; Balhorn, R. L.; Allen, M. J.; McElfresh, M. W. *Biophys. J.* **2004**, *86*, 2430-2437.

(119) Lo, Y. S.; Huefner, N. D.; Chan, W. S.; Stevens, F.; Harris, J. M.; Beebe, T. P. *Langmuir* **1999**, *15*, 1373-1382.

(120) Florin, E.; Moy, V.; Gaub, H. *Science* **1994**, *264*, 415-417.

(121) Ebner, A.; Wildling, L.; Zhu, R.; Rankl, C.; Haselgrubler, T.; Hinterdorfer, P.; Gruber, H. J. *Stm and Afm Studies on (Bio)Molecular Systems: Unravelling the Nanoworld* **2008**, *285*, 29-76.

(122) Love, J. C.; Estroff, L. A.; Kriebel, J. K.; Nuzzo, R. G.; Whitesides, G. M. *Chem. Rev.* **2005**, *105*, 1103-1170.

(123) Harada, Y.; Kuroda, M.; Ishida, A. *Langmuir* **1999**, *16*, 708-715.

(124) Bonanni, B.; Kamruzzahan, A. S. M.; Bizzarri, A. R.; Rankl, C.; Gruber, H. J.; Hinterdorfer, P.; Cannistraro, S. *Biophys. J.* **2005**, *89*, 2783-2791.

(125) Bustanji, Y.; Arciola, C. R.; Conti, M.; Mandello, E.; Montanaro, L.; Samori, B. *Proc. Natl. Acad. Sci. U. S. A.* **2003**, *100*, 13292-13297.

(126) Kienberger, F.; Pastushenko, V. P.; Kada, G.; Gruber, H. J.; Riener, C.; Schindler, H.; Hinterdorfer, P. *Single Mol.* **2000**, *1*, 123-128.

(127) Dean, D.; Han, L.; Grodzinsky, A. J.; Ortiz, C. *J. Biomech.* **2006**, *39*, 2555-2565.

(128) Gad, M.; Itoh, A.; Ikai, A. *Cell Biol. Int.* **1997**, *21*, 697-706.

(129) Wagner, P.; Hegner, M.; Kernen, P.; Zaugg, F.; Semenza, G. *Biophys. J.* **1996**, *70*, 2052-2066.

(130) Gruber, H. J.; Kada, G.; Pragl, B.; Riener, C.; Hahn, C. D.; Harms, G. S.; Ahrer, W.; Dax, T. G.; Hohenthanner, K.; Knaus, H.-G. *Bioconjugate Chem.* **2000**, *11*, 161-166.

(131) Kienberger, F.; Kada, G.; Gruber, H. J.; Pastushenko, V. P.; Riener, C.; Trieb, M.; Knaus, H.-G.; Schindler, H.; Hinterdorfer, P. *Single Mol.* **2000**, *1*, 59-65.

(132) Khatri, O. P.; Adachi, K.; Murase, K.; Okazaki, K.-i.; Torimoto, T.; Tanaka, N.; Kuwabata, S.; Sugimura, H. *Langmuir* **2008**, *24*, 7785-7792.

(133) Ratto, T. V.; Rudd, R. E.; Langry, K. C.; Balhorn, R. L.; McElfresh, M. W. *Langmuir* **2006**, *22*, 1749-1757.

(134) Ebner, A.; Kienberger, F.; Kada, G.; Stroh, C. M.; Geretschläger, M.; Kamruzzahan, A. S. M.; Wildling, L.; Johnson, W. T.; Ashcroft, B.; Nelson, J.; Lindsay, S. M.; Gruber, H. J.; Hinterdorfer, P. *ChemPhysChem* **2005**, *6*, 897-900.

(135) Crampton, N.; Bonass, W. A.; Kirkham, J.; Thomson, N. H. *Langmuir* **2005**, *21*, 7884-7891.

(136) Gauthier, S.; Aimé, J. P.; Bouhacina, T.; Attias, A. J.; Desbat, B. *Langmuir* **1996**, *12*, 5126-5137.

(137) Otsuka, H.; Arima, T.; Koga, T.; Takahara, A. *J. Phys. Org. Chem.* **2005**, *18*, 957-961.

(138) Moon, J. H.; Shin, J. W.; Kim, S. Y.; Park, J. W. *Langmuir* **1996**, *12*, 4621-4624.

(139) Jiang, Y.; Zhu, C.; Ling, L.; Wan, L.; Fang, X.; Bai, C. *Anal. Chem.* **2003**, *75*, 2112-2116.

(140) Chen, X.; Davies, M. C.; Roberts, C. J.; Tendler, S. J. B.; Williams, P. M.; Davies, J.; Dawkes, A. C.; Edwards, J. C. *Langmuir* **1997**, *13*, 4106-4111.

(141) Conti, M.; Donati, G.; Cianciolo, G.; Stefoni, S.; Samorì, B. *J. Biomed.l Mater. Res.* **2002**, *61*, 370-379.

(142) Karrasch, S.; Dolder, M.; Schabert, F.; Ramsden, J.; Engel, A. *Biophys. J.* **1993**, *65*, 2437-2446.

(143) Schindler, H.; Badt, D.; Hinterdorfer, F. K. P.; Raab, A.; Wielert-Badt, S.; Pastushenko, V. P. *Ultramicroscopy* **2000**, *82*, 227-235.

(144) Yam, C.-M.; Xiao, Z.; Gu, J.; Boutet, S.; Cai, C. *J. Am. Chem. Soc.* **2003**, *125*, 7498-7499.

(145) Michalet, X.; Weiss, S.; Jager, M. *Chem. Rev.* **2006**, *106*, 1785-1813.

(146) Zlatanova, J.; Lindsay, S. M.; Leuba, S. H. *Prog. .Biophys.Mol. Bio.* **2000**, *74*, 37-61.

(147) Myong, S.; Stevens, B. C.; Ha, T. *Structure* **2006**, *14*, 633-643.

(148) Bongrand, P. *Rep. Prog. Phys.* **1999**, *62*, 921-968.

(149) Hugel, T.; Seitz, M. *Macromol. Rapid Commun.* **2001**, *22*, 989-1016.

(150) Lindsay, S. M.; Barris, B. *J. Vac. Sci. Technol. A-Vac. Surf. Films* **1988**, *6*, 544-547.

(151) Borgia, A.; Williams, P. M.; Clarke, J. *Annu. Rev. Biochem.* **2008**, *77*, 101-125.

(152) Bokinsky, G.; Zhuang, X. W. *Acc. Chem. Res.* **2005**, *38*, 566-573.

(153) Leckband, D. *Annu. Rev. Bioph. Biom.* **2000**, *29*, 1-26.

(154) Morris, V. J.; Kirby, A. R.; Gunning, A. P. *atomic force microscopy for biologists*; Imperial College Press :London, 2004.

(155) Janshoff, A.; Neitzert, M.; Oberdorfer, Y.; Fuchs, H. *Angew. Chem., Int. Ed.* **2000**, *39*, 3213-3237.

(156) Allen, S.; Rigby-Singleton, S. M.; Harris, H.; Davies, M. C.; O'Shea, P. *Biochem. Soc. Trans.* **2003**, *31*, 1052-1057.

(157) Olsnes, S.; Kozlov, J. V. *Toxicon* **2001**, *39*, 1723-1728.

(158) Lord, J. M.; Roberts, L. M.; Robertus, J. D. *FASEB J.* **1994**, *8*, 201-208.

(159) Ler, S. G.; Lee, F. K.; Gopalakrishnakone, P. *J. Chromatogr. A* **2006**, *1133*, 1-12.

(160) Lubelli, C.; Chatgilialoglu, A.; Bolognesi, A.; Strocchi, P.; Colombatti, M.; Stirpe, F. *Anal. Biochem.* **2006**, *355*, 102-109.

(161) Ramakrishnan, S.; Eagle, M. R.; Houston, L. L. *Biochim. Biophys. Acta, Gen. Subj.* **1982**, *719*, 341-348.

(162) Koja, N.; Shibata, T.; Mochida, K. *Toxicon* **1980**, *18*, 611-618.

(163) Poli, M. A.; Rivera, V. R.; Hewetson, J. F.; Merrill, G. A. *Toxicon* **1994**, *32*, 1371-1377.

(164) Schofield, C. L.; Mukhopadhyay, B.; Hardy, S. M.; McDonnell, M. B.; Field, R. A.; Russell, D. A. *Analyst* **2008**, *133*, 626-634.

(165) Takae, S.; Akiyama, Y.; Otsuka, H.; Nakamura, T.; Nagasaki, Y.; Kataoka, K. *Biomacromolecules* **2005**, *6*, 818-824.

(166) Hines, H. B.; Brueggemann, E. E. *J. Chromatogr. A* **1994**, *670*, 199-208.

(167) Krutchinsky, A. N.; Zhang, W.; Chait, B. T. *J. Am. Soc. Mass. Spectrom.* **2000**, *11*, 493-504.

(168) Rubina, A. Y.; Dyukova, V. I.; Dementieva, E. I.; Stomakhin, A. A.; Nesmeyanov, V. A.; Grishin, E. V.; Zasedatelev, A. S. *Anal. Biochem.* **2005**, *340*, 317-329.

(169) Gabai, R.; Segev, L.; Joselevich, E. *J. Am. Chem. Soc.* **2005**, *127*, 11390-11398.

(170) Riener, C. K.; Stroh, C. M.; Ebner, A.; Klampfl, C.; Gall, A. A.; Romanin, C.; Lyubchenko, Y. L.; Hinterdorfer, P.; Gruber, H. J. *Anal. Chim. Acta* **2003**, *479*, 59-75.

(171) Nandivada, H.; Jiang, X. W.; Lahann, J. *Adv. Mat.* **2007**, *19*, 2197-2208.

(172) Moses, J. E.; Moorhouse, A. D. *Chem. Soc. Rev.* **2007**, *36*, 1249-1262.

(173) Kolb, H. C.; Sharpless, K. B. *Drug Discovery Today* **2003**, *8*, 1128-1137.

(174) Bain, C. D.; Whitesides, G. M. *Science* **1988**, *240*, 62-63.

(175) Hartmuth C. Kolb, M. G. F., K. Barry Sharpless *Angew. Chem., Int. Ed.* **2001**, *40*, 2004-2021.

(176) Ulman, A. *Chem. Rev.* **1996**, *96*, 1533-1554.

(177) Van Damme, E. J. M.; Barre, A.; Barbieri, L.; Valbonesi, P.; Rouge, P.; Van Leuven, F.; Stirpe, F.; Peumans, W. J. *Biochem. J.* **1997**, *324*, 963-970.

(178) Carra John, H.; McHugh Colleen, A.; Mulligan, S.; Machiesky Leeann, M.; Soares Alexei, S.; Millard Charles, B. *BMC Struct. Biol.* **2007**, *7*, 72.

(179) Rutenber, E.; Katzin, B. J.; Ernst, S.; Collins, E. J.; Mesna, D.; Ready, M. P.; Robertus, J. D. *Proteins* **1991**, *10*, 240-50.

(180) Radmacher, M.; Fritz, M.; Hansma, H. G.; Hansma, P. K. *Science* **1994**, *265*, 1577-9.

(181) Ray, C.; Brown, J. R.; Akhremitchev, B. B. *Langmuir* **2007**, *23*, 6076-6083.

(182) Kersey, F. R.; Yount, W. C.; Craig, S. L. *J. Am. Chem. Soc.* **2006**, *128*, 3886-3887.

(183) Perret, E.; Leung, A.; Feracci, H.; Evans, E. *Proc. Nat. Acad. Sci. U.S.A.* **2004**, *101*, 16472-16477.

(184) Evans, E. *Annu. Rev. Biophys. Biomol. Struct.* **2001**, *30*, 105-28.

(185) Kienberger, F.; Kada, G.; Mueller, H.; Hinterdorfer, P. *J. Mol. Biol.* **2005**, *347*, 597-606.

(186) Janshoff, A.; Steinem, C. *Chemphyschem* **2001**, *2*, 577-579.

(187) Rief, M.; Gautel, M.; Oesterhelt, F.; Fernandez, J. M.; Gaub, H. E. *Science* **1997**, *276*, 1109-1112.

(188) Friedsam, C.; Wehle, A. K.; Kuhner, F.; Gaub, H. E. *J. Phys. Condens. Matter* **2003**, *15*, S1709-S1723.

(189) Harris, N. C.; Song, Y.; Kiang, C. H. *Phys. Rev. Lett.* **2007**, *99*, 4.

(190) Imparato, A.; Sbrana, F.; Vassalli, M. *Epl* **2008**, *82*, 5.

(191) Liu, M.; Sun, T.; Hu, J.; Chen, W.; Wang, C. *Biophys. Chem.* **2008**, *135*, 19-24.

(192) Tinoco, I. *Annu. Rev. Biophys. Biomolec. Struct.* **2004**, *33*, 363-385.

(193) Ritort, F.; Bustamante, C.; Tinoco, I. *Proc. Nat. Acad. Sci. U.S.A.* **2002**, *99*, 13544-13548.

(194) Pasquale, E. B. *Nat. Rev. Mol. Cell Biol.* **2005**, *6*, 462-475.

(195) Pasquale, E. B. *Cell* **2008**, *133*, 38-52.

(196) Surawska, H.; Ma, P. C.; Salgia, R. *Cytokine & Growth Factor Rev.* **2004**, *15*, 419-433.

(197) Wykosky, J.; Debinski, W. *Mol. Cancer Res.* **2008**, *6*, 1795-1806.

(198) Koolpe, M.; Dail, M.; Pasquale, E. B. *J. Biol. Chem.* **2002**, *277*, 46974-46979.

(199) Blackburn, W. H.; Dickerson, E. B.; Smith, M. H.; McDonald, J. F.; Lyon, L. A. *Bioconjugate Chem.* **2009,** *20*, 960-968.

(200) Scarberry, K. E.; Dickerson, E. B.; McDonald, J. F.; Zhang, Z. J. *J. Am. Chem. Soc.* **2008**, *130*, 10258-10262.

(201) Dickerson, E. B.; Blackburn, W. H.; Smith, M. H.; Kapa, L. B.; Lyon, L. A.; McDonald, J. F. *BMC Cancer* **2010**, *10*, 10.

(202) Wykosky, J.; Palma, E.; Gibo, D. M.; Ringler, S.; Turner, C. P.; Debinski, W. *Oncogene* **2008**, *27*, 7260-7273.

(203) Cleveland, J. P.; Manne, S.; Bocek, D.; Hansma, P. K. *Rev. Sci. Instrum.* **1993**, *64*, 403-405.

(204) Evans, E.; Ritchie, K. *Biophys. J.* **1997**, *72*, 1541-55.

(205) Himanen, J. P.; Goldgur, Y.; Miao, H.; Myshkin, E.; Guo, H.; Buck, M.; Nguyen, M.; Rajashankar, K. R.; Wang, B.; Nikolov, D. B. *EMBO Rep.* **2009**, *10*, 722-8.

(206) Zhang, Y. *BMC Bioinf.* **2008**, *9*, 40.

(207) Wu, S.; Zhang, Y. *Nucleic Acids Res.* **2007**, *35*, 3375-82.

(208) Himanen, J. P.; Rajashankar, K. R.; Lackmann, M.; Cowan, C. A.; Henkemeyer, M.; Nikolov, D. B. *Nature* **2001**, *414*, 933-938.

(209) Flanagan, J. G.; Vanderhaeghen, P. *Annu. Rev. Neurosci.* **1998**, *21*, 309-345.

(210) Pabbisetty, K. B.; Yue, X.; Li, C.; Himanen, J. P.; Zhou, R.; Nikolov, D. B.; Hu, L. *Protein Sci.* **2007**, *16*, 355-61.

(211) Torchilin, V. P. *Nat. Rev. Drug Discov.* **2005**, *4*, 145-160.

(212) Nishiyama, N.; Kataoka, K. *Pharmacol. Ther.* **2006**, *112*, 630-648.

(213) Peer, D.; Karp, J. M.; Hong, S.; Farokhzad, O. C.; Margalit, R.; Langer, R. *Nat. Nanotechnol.* **2007**, *2*, 751-760.

(214) Ganta, S.; Devalapally, H.; Shahiwala, A.; Amiji, M. *J. Control Release* **2008**, *126*, 187-204.

(215) Zhao, X.; Li, H.; Lee, R. J. *Expert. Opin. Drug Deliv.* **2008**, *5*, 309-319.

(216) Torchilin, V. P. *Biopolymers* **2008**, *90*, 604-610.

(217) Nativo, P.; Prior, I. A.; Brust, M. *ACS Nano* **2008**, *2*, 1639-1644.

(218) Xie, W.; Wang, L.; Zhang, Y.; Su, L.; Shen, A.; Tan, J.; Hu, J. *Bioconjugate Chem.* **2009**, *20*, 768-773.

(219) Tornoe, C. W.; Christensen, C.; Meldal, M. *J. Org. Chem.* **2002**, *67*, 3057-3064.

(220) Rostovtsev, V. V.; Green, L. G.; Fokin, V. V.; Sharpless, K. B. *Angew. Chem. Int. Ed. Engl.* **2002**, *41*, 2596-2599.

(221) Lutz, J. F. *Angew. Chem. Int. Ed. Engl.* **2007**, *46*, 1018-1025.

(222) van Dijk, M.; Rijkers, D. T. S.; Liskamp, R. M. J.; van Nostrum, C. F.; Hennink, W. E. *Bioconjugate Chem.* **2009**, *20*, 2001-2016.

(223) Sumerlin, B. S.; Vogt, A. P. *Macromolecules* **2010**, *43*, 1-13.

(224) Agard, N. J.; Prescher, J. A.; Bertozzi, C. R. *J. Am. Chem. Soc.* **2004**, *126*, 15046-15047.

(225) Ning, X. H.; Guo, J.; Wolfert, M. A.; Boons, G. J. *Angew. Chem. Int. Ed.* **2008**, *47*, 2253-2255.

(226) Ben Slimane, A.; Chehimi, M. M.; Vaulay, M. J. *Colloid Polym. Sci.* **2004**, *282*, 314-323.

(227) Yoshimoto, K.; Nozawa, M.; Matsumoto, S.; Echigo, T.; Nemoto, S.; Hatta, T.; Nagasaki, Y. *Langmuir* **2009**, *25*, 12243-12249.

(228) Gohy, J. F. *Adv. Poly. Sci.* **2005**, *190*, 65-163.

(229) Renaud, G.; Lazzari, R.; Leroy, F. *Surf. Sci. Rep.* **2009**, *64*, 255-380.

(230) Korstgens, V.; Wiedersich, J.; Meier, R.; Perlich, J.; Roth, S. V.; Gehrke, R.; Muller-Buschbaum, P. *Anal. Bioanal. Chem.* **2010**, *396*, 139-149.

(231) Han, W.; Lindsay, S. M.; Jing, T. *Appl. Phys. Lett.* **1996**, *69*, 4111-4113.

(232) Allison, D. P.; Hinterdorfer, P.; Han, W. *Curr. Opin. Biotechnol.* **2002**, *13*, 47-51.

(233) Artelsmair, H.; Kienberger, F.; Tinazli, A.; Schlapak, R.; Zhu, R.; Preiner, J.; Wruss, J.; Kastner, M.; Saucedo-Zeni, N.; Hoelzl, M.; Rankl, C.; Baumgartner, W.; Howorka, S.; Blaas, D.; Gruber, H. J.; Tampe, R.; Hinterdorfer, P. *Small* **2008**, *4*, 847-854.

(234) Baumgartner, W.; Hinterdorfer, P.; Ness, W.; Raab, A.; Vestweber, D.; Schindler, H.; Drenckhahn, D. *Biophys. J.* **1999**, *76*, A351-A351.

(235) Lee, S.; Mandic, J.; Van Vliet, K. J. *Proc. Natl. Acad. Sci. U.S.A.* **2007**, *104*, 9609-9614.

(236) Kim, M. S.; Hyun, H.; Cho, Y. H.; Seo, K. S.; Jang, W. Y.; Kim, S. K.; Khang, G.; Lee, H. B. *Polym. Bull.* **2005**, *55*, 149-156.

(237) Lu, C. F.; Guo, S. R.; Liu, L.; Zhang, Y. Q.; Li, Z. H.; Gu, J. R. *J Polym. Sci. Pol. Phys.* **2006**, *44*, 3406-3417.

(238) Fuss, C.; Palmaz, J. C.; Sprague, E. A. *J. .Vasc. Interv. Radiol.* **2001**, *12*, 677-682.

(239) Agnihotri, A.; Siedlecki, C. A. *Langmuir* **2004**, *20*, 8846-8852.

(240) Sit, P. S.; Marchant, R. E. *Thromb. Haemost.* **1999**, *82*, 1053-1060.

(241) Sit, P. S.; Marchant, R. E. *Surf. Sci.* **2001**, *491*, 421-432.

(242) Ta, T. C.; Sykes, M. T.; McDermott, M. T. *Langmuir* **1998**, *14*, 2435-2443.

(243) Tunc, S.; Maitz, M. F.; Steiner, G.; Vázquez, L.; Pham, M. T.; Salzer, R. *Colloids Surf., B* **2005**, *42*, 219-225.

(244) Toscano, A.; Santore, M. M. *Langmuir* **2006**, *22*, 2588-2597.

(245) Ortega-Vinuesa, J. L.; Tengvall, P.; Lundström, I. *J. Colloid Interface Sci.* **1998**, *207*, 228-239.

(246) Green, R. J.; Davies, J.; Davies, M. C.; Roberts, C. J.; Tendler, S. J. B. *Biomaterials* **1997**, *18*, 405-413.

(247) Lewis, K. B.; Ratner, B. D. *Colloids Surf., B* **1996**, *7*, 259-269.

(248) Cacciafesta, P.; Humphris, A. D. L.; Jandt, K. D.; Miles, M. J. *Langmuir* **2000**, *16*, 8167-8175.

(249) Xu, L.-C.; Siedlecki, C. A. *Langmuir* **2009**, *25*, 3675-3681.

(250) Vroman, L.; Adams, A. L. *Thromb. Diath. Haemost.* **1967**, *18*, 510-&.

(251) Hansma, H. G.; Hoh, J. H. *Annu. Rev. Bioph. Biom.* **1994**, *23*, 115-140.

(252) Lewinski, N.; Colvin, V.; Drezek, R. *Small* **2008**, *4*, 26-49.

(253) Chidsey, C. E. D.; Loiacono, D. N.; Sleator, T.; Nakahara, S. *Surf. Sci.* **1988**, *200*, 45-66.

(254) Kollman, J. M.; Pandi, L.; Sawaya, M. R.; Riley, M.; Doolittle, R. F. *Biochemistry* **2009**, *48*, 3877-3886.

(255) Guex, N.; Peitsch, M. C. *Electrophoresis* **1997**, *18*, 2714-2723.

(256) Blombäck, B.; Hessel, B.; Hogg, D. *Thromb. Res.* **1976**, *8*, 639-658.

(257) Hoeprich, P. D.; Doolittle, R. F. *Biochemistry* **1983**, *22*, 2049-2055.

(258) Huang, S. M.; Cao, Z. Y.; Davie, E. W. *Biochem. Biophys. Res. Commun.* **1993**, *190*, 488-495.

(259) Hall, C. E.; Slayter, H. S. *J. Cell Biol.* **1959**, *5*, 11-27.

(260) Geer, C. B.; Rus, I. A.; Lord, S. T.; Schoenfisch, M. H. *Acta Biomater.* **2007**, *3*, 663-668.

(261) Giesbers, M.; Kleijn, J. M.; Cohen Stuart, M. A. *J. Colloid Interface Sci.* **2002**, *248*, 88-95.

(262) Reichert, J.; Wei, G.; Jandt, K. D. *Adv. Eng. Mater.* **2009**, *9999*, NA.

(263) Doolittle, R. F.; Goldbaum, D. M.; Doolittle, L. R. *J. Mol. Biol.* **1978**, *120*, 311-325.

(264) Zhang, J.; Redman, C. *J. Biol. Chem.* **1994**, *269*, 652-658.

(265) Gorkun, O. V.; Veklich, Y. I.; Medved, L. V.; Henschen, A. H.; Weisel, J. W. *Biochemistry* **2002**, *33*, 6986-6997.

(266) Mosesson, M. W.; Siebenlist, K. R.; Hainfeld, J. F.; Wall, J. S. *J. Struct. Biol.* **1995**, *115*, 88-101.

(267) Mosesson, M. W.; Siebenlist, K. R.; DiOrio, J. P.; Matsuda, M.; Hainfeld, J. F.; Wall, J. S. *J. Clin. Invest.* **1995**, *96*, 1053-1058.

(268) Veklich, Y. I.; Gorkun, O. V.; Medved, L. V.; Nieuwenhuizen, W.; Weisel, J. W. *J. Biol. Chem.* **1993**, *268*, 13577-13585.

(269) Chen, G. J.; Ni, N. T.; Zhou, J. F.; Chuang, Y. J.; Wang, B. H.; Pan, Z. W.; Xu, B. Q. *J. Nanosci. Nanotechnol.* 2011, 11, 74-81.

(270) Elghanian, R.; Storhoff, J. J.; Mucic, R. C.; Letsinger, R. L.; Mirkin, C. A. *Science* **1997**, *277*, 1078-1081.

(271) El-Sayed, I. H.; Huang, X.; El-Sayed, M. A. *Nano Lett.* **2005**, *5*, 829-834.

(272) Huang, X.; El-Sayed, I. H.; Qian, W.; El-Sayed, M. A. *J. Am. Chem. Soc.* **2006**, *128*, 2115-2120.

(273) Lazarides, A. A.; Schatz, G. C. *J. Phys. Chem. B* **1999**, *104*, 460-467.

(274) Link, S.; El-Sayed, M. A. *J. Phys. Chem. B* **1999**, *103*, 4212-4217.

(275) Zharov, V. P.; Mercer, K. E.; Galitovskaya, E. N.; Smeltzer, M. S. *Biophys. J.* **2006**, *90*, 619-627.

(276) Chen, W. *J. Nanosci. Nanotechnol.* **2008**, *8*, 1019-1051.

(277) Murphy, C. J.; Gole, A. M.; Stone, J. W.; Sisco, P. N.; Alkilany, A. M.; Goldsmith, E. C.; Baxter, S. C. *Acc. Chem. Res.* **2008**, *41*, 1721-1730.

(278) Jain, P.; Huang, X.; El-Sayed, I.; El-Sayed, M. *Plasmonics* **2007**, *2*, 107-118.

(279) Nel, A.; Xia, T.; Madler, L.; Li, N. *Science* **2006**, *311*, 622-627.

(280) Zhang, Y. B.; Chen, W.; Zhang, J.; Liu, J.; Chen, G. P.; Pope, C. *J. Nanosci. Nanotechnol.* **2007**, *7*, 497-503.

(281) Pernodet, N.; Fang, X.; Sun, Y.; Bakhtina, A.; Ramakrishnan, A.; Sokolov, J.; Ulman, A.; Rafailovich, M. *Small* **2006**, *2*, 766-773.

(282) Tkachenko, A. G.; Xie, H.; Coleman, D.; Glomm, W.; Ryan, J.; Anderson, M. F.; Franzen, S.; Feldheim, D. L. *J. Am. Chem. Soc.* **2003**, *125*, 4700-4701.

(283) Tkachenko, A. G.; Xie, H.; Liu, Y.; Coleman, D.; Ryan, J.; Glomm, W. R.; Shipton, M. K.; Franzen, S.; Feldheim, D. L. *Bioconjugate Chem.* **2004**, *15*, 482-490.

(284) Goodman, C. M.; McCusker, C. D.; Yilmaz, T.; Rotello, V. M. *Bioconjugate Chem.* **2004**, *15*, 897-900.

(285) Chithrani, B. D.; Ghazani, A. A.; Chan, W. C. W. *Nano Lett.* **2006**, *6*, 662-668.

(286) Shukla, R.; Bansal, V.; Chaudhary, M.; Basu, A.; Bhonde, R. R.; Sastry, M. *Langmuir* **2005**, *21*, 10644-10654.

(287) Cedervall, T.; Lynch, I.; Lindman, S.; Berggard, T.; Thulin, E.; Nilsson, H.; Dawson, K. A.; Linse, S. *Proc. Natl. Acad. Sci. U. S. A.* **2007**, *104*, 2050-2055.

(288) Lim, B. B. C.; Lee, E. H.; Sotomayor, M.; Schulten, K. *Structure* **2008**, *16*, 449-459.

(289) Hoet, P.; Bruske-Hohlfeld, I.; Salata, O. *J. Nanobiotechnol.* **2004**, *2*, 12.

(290) Li, J. J.; Zou, L.; Hartono, D.; Ong, C.-N.; Bay, B.-H.; Yung, L.-Y. L. *Adv. Mater.* **2008**, *20*, 138-142.

(291) Bakshi, M. S.; Zhao, L.; Smith, R.; Possmayer, F.; Petersen, N. O. *Biophys. J.* **2008**, *94*, 855-868.

(292) Jacobsen, N.; Moller, P.; Jensen, K.; Vogel, U.; Ladefoged, O.; Loft, S.; Wallin, H. *Part. Fibre Toxicol.* **2009**, *6*, 2.

(293) Peters, A. P.; Dockery, D. W. S.; Muller, J. E. M. D.; Mittleman, M. A. M. D. D. *Circulation* **2001**, *103*, 2810-2815.

(294) Chen, G. J.; Ni, N. T.; Wang, B. H.; Xu, B. Q. *ChemPhysChem* **2010**, *11*, 565-568.

(295) Chuang, Y.-J.; Zhou, X.; Pan, Z.; Turchi, C. *Biochem. Biophys. Res. Commun.* **2009**, *389*, 22-27.

(296) Liu, X.; Atwater, M.; Wang, J. H.; Dai, Q.; Zou, J. H.; Brennan, J. P.; Huo, Q. *J. Nanosci. Nanotechnol.* **2007**, *7*, 3126-3133.

(297) Alexis, F.; Pridgen, E.; Molnar, L. K.; Farokhzad, O. C. *Mol. Pharmaceutics* **2008**, *5*, 505-515.

(298) Sonavane, G.; Tomoda, K.; Makino, K. *Colloids Surf., B* **2008**, *66*, 274-280.

(299) Kim, J. H.; Kim, J. H.; Kim, K.-W.; Kim, M. H.; Yu, Y. S. *Nanotechnol.* **2009**, 505101.

(300) Haiss, W.; Thanh, N. T. K.; Aveyard, J.; Fernig, D. G. *Anal. Chem.* **2007**, *79*, 4215-4221.

(301) Liang, P.-H.; Wang, S.-K.; Wong, C.-H. *J. Am. Chem. Soc.* **2007**, *129*, 11177-11184.

(302) Schofield, C. L.; Haines, A. H.; Field, R. A.; Russell, D. A. *Langmuir* **2006**, *22*, 6707-6711.

(303) Roy, S.; Dasgupta, A. K. *FEBS Lett.* **2007**, *581*, 5533-5542.

(304) Wei, G.; Reichert, J.; Jandt, K. D. *Chem. Commun.* **2008**, 3903-3905.

(305) Stark, R. W. *Mater. Today* **2010**, *13*, 24-32.

(306) Webster, K. D.; Crow, A.; Fletcher, D. A. *PLoS One* **2011**, *6*, 7.

(307) Parlak, Z.; Hadizadeh, R.; Balantekin, M.; Degertekin, F. L. *Ultramicroscopy* **2009**, *109*, 1121-1125.

APPENDIX A

SUPPLEMENTS TO CHAPTER 2

In Appendix A, there is some supplement information for Chapter 2.

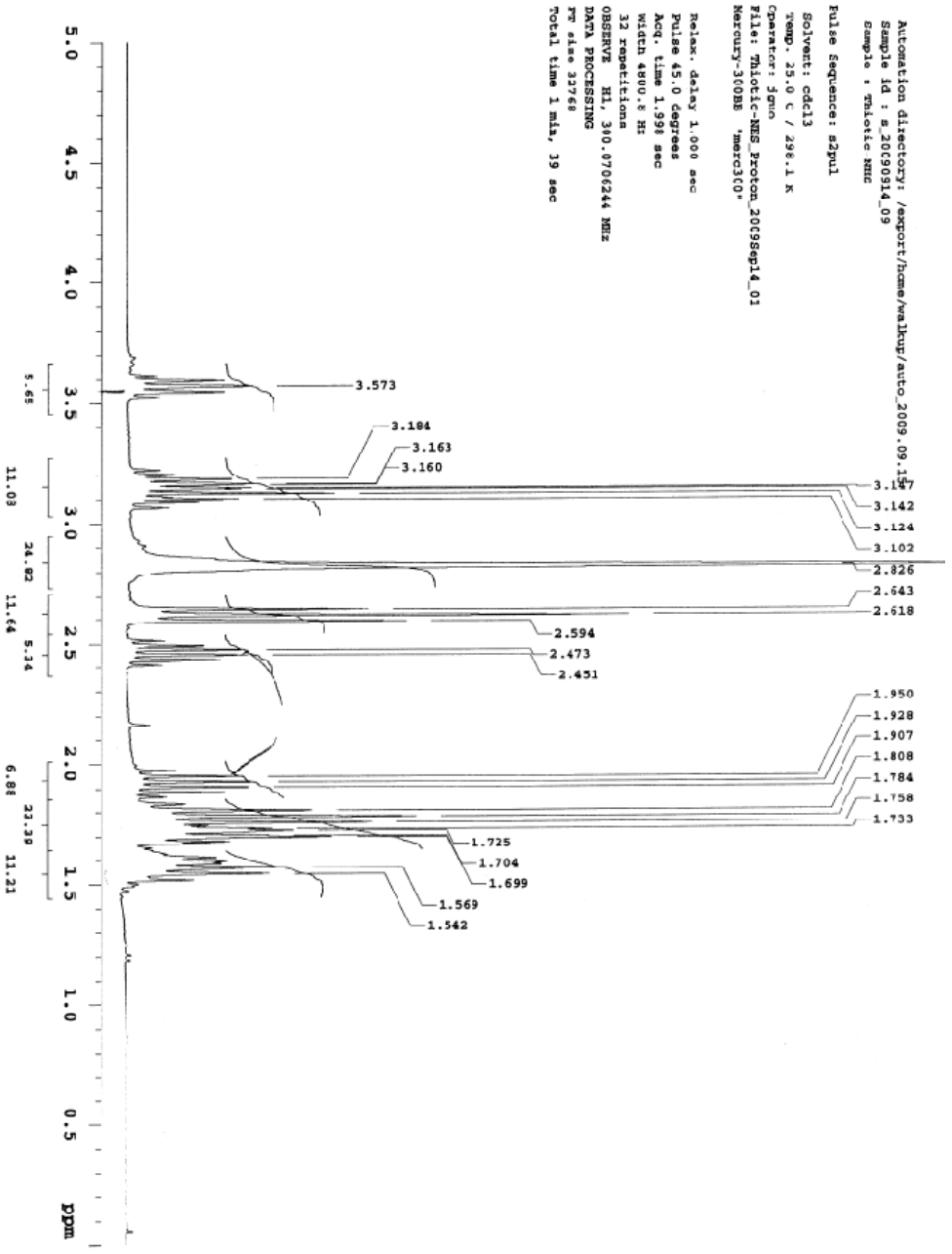

Figure A.1 ^{1}H-NMR spectrum of **Compound 1** in Deuterochloroform ($CDCl_3$)

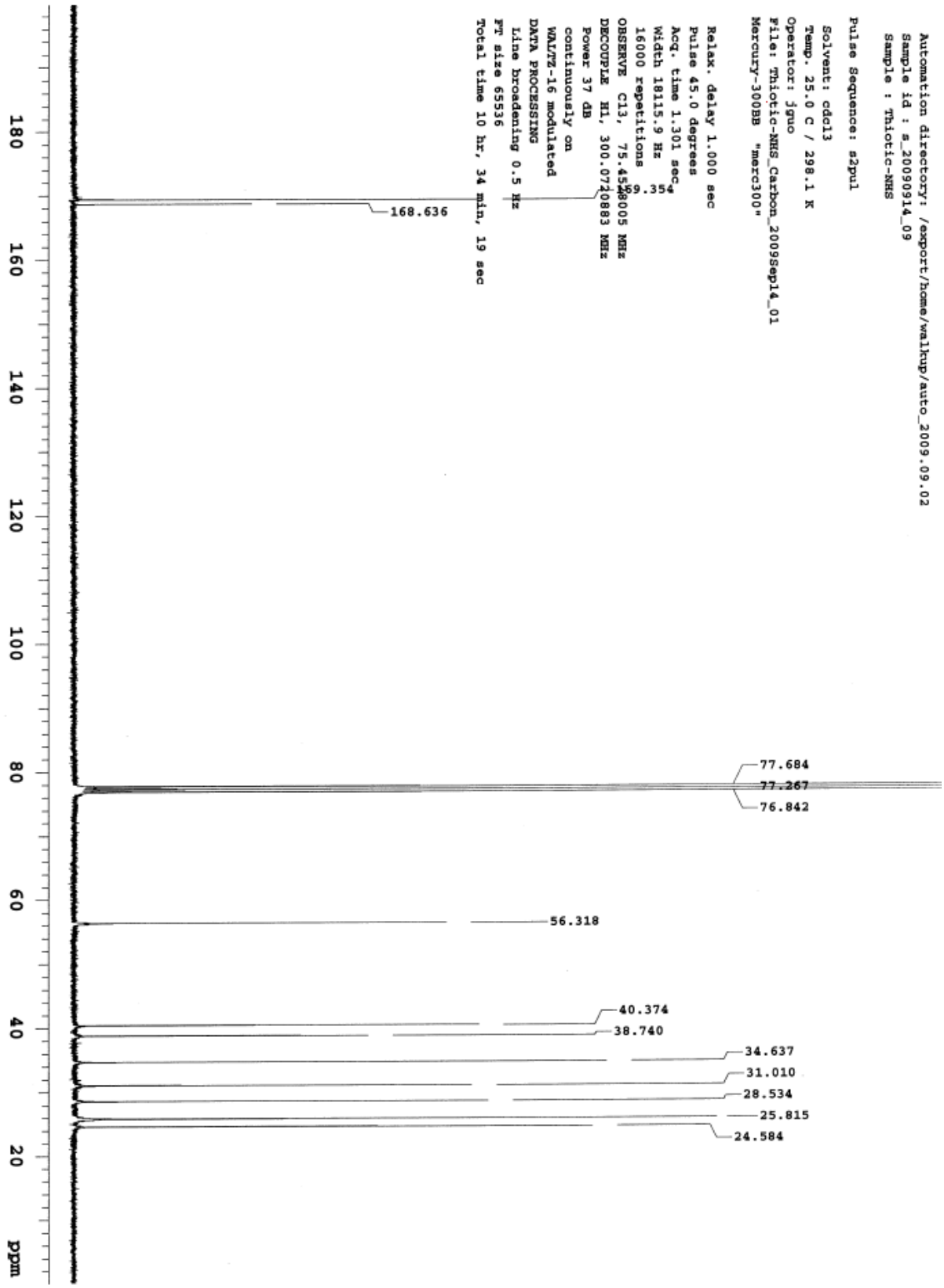

Figure A.2 ^{13}C-NMR spectrum of **Compound 1** in Deuterochloroform ($CDCl_3$)

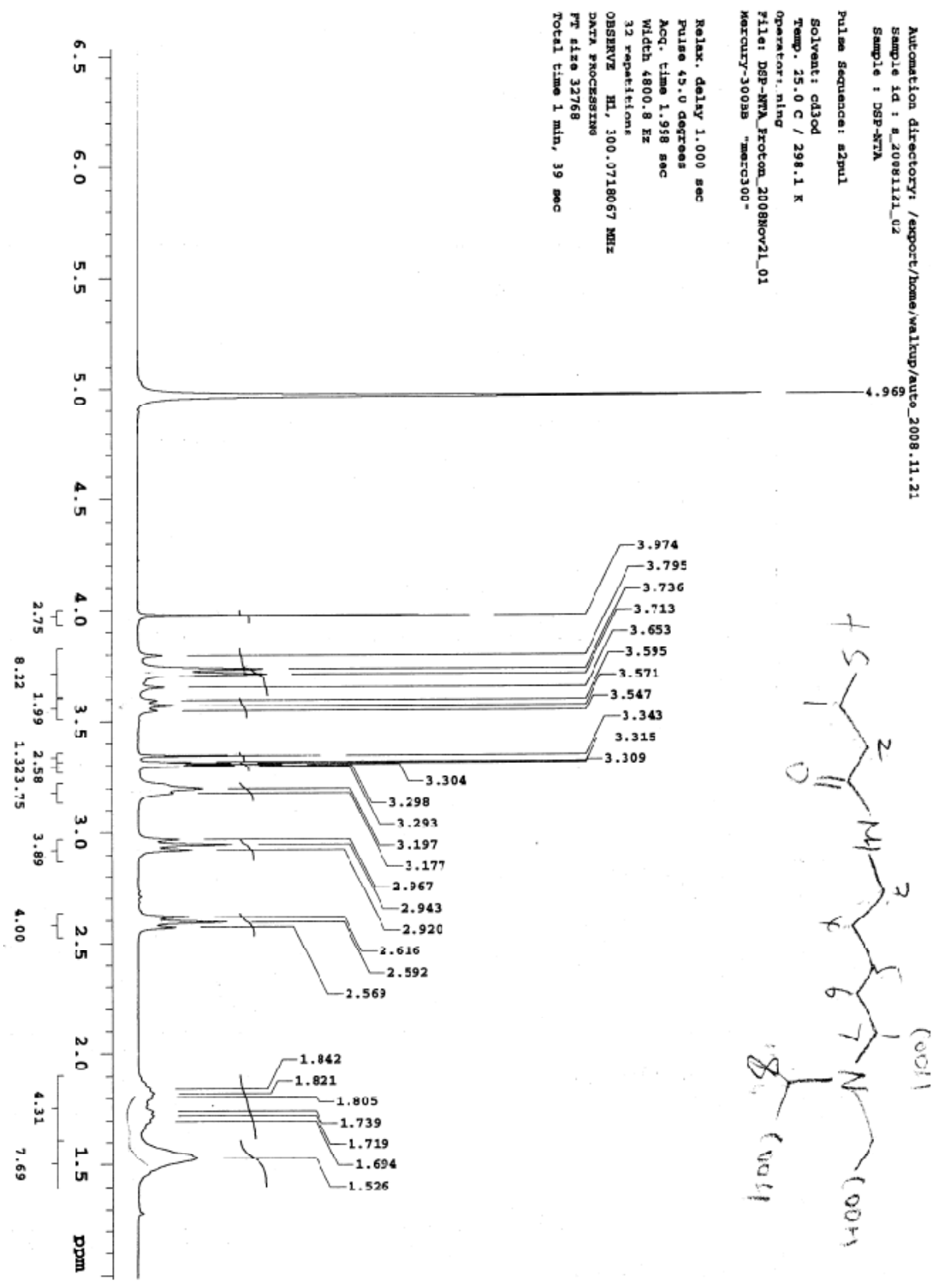

Figure A.3 ^{1}H-NMR spectrum of **Compound 2** in Deuteromethanol (CD_3OD)

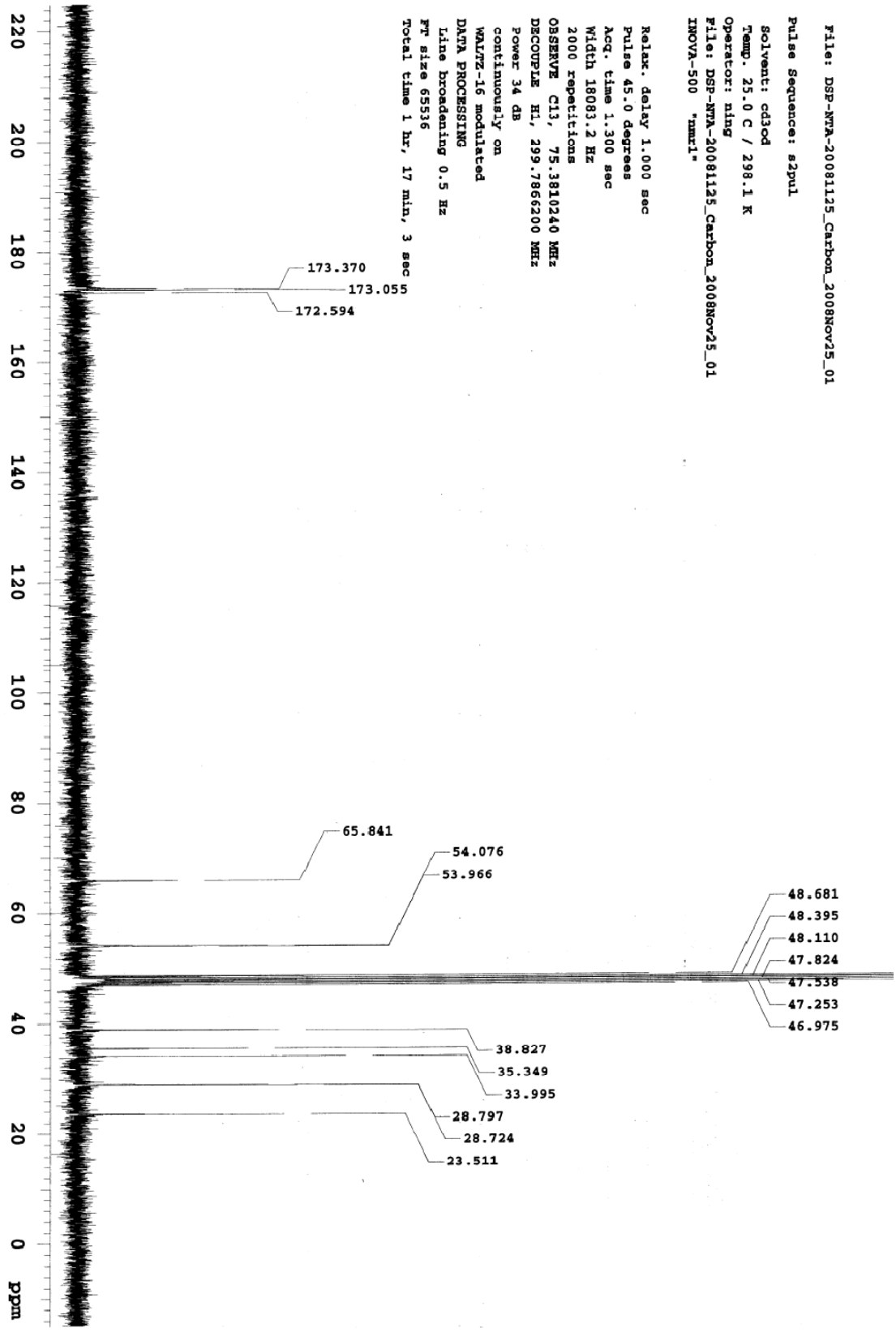

Figure A.4 ^{13}C-NMR spectrum of **Compound 2** in Deuteromethanol (CD_3OD)

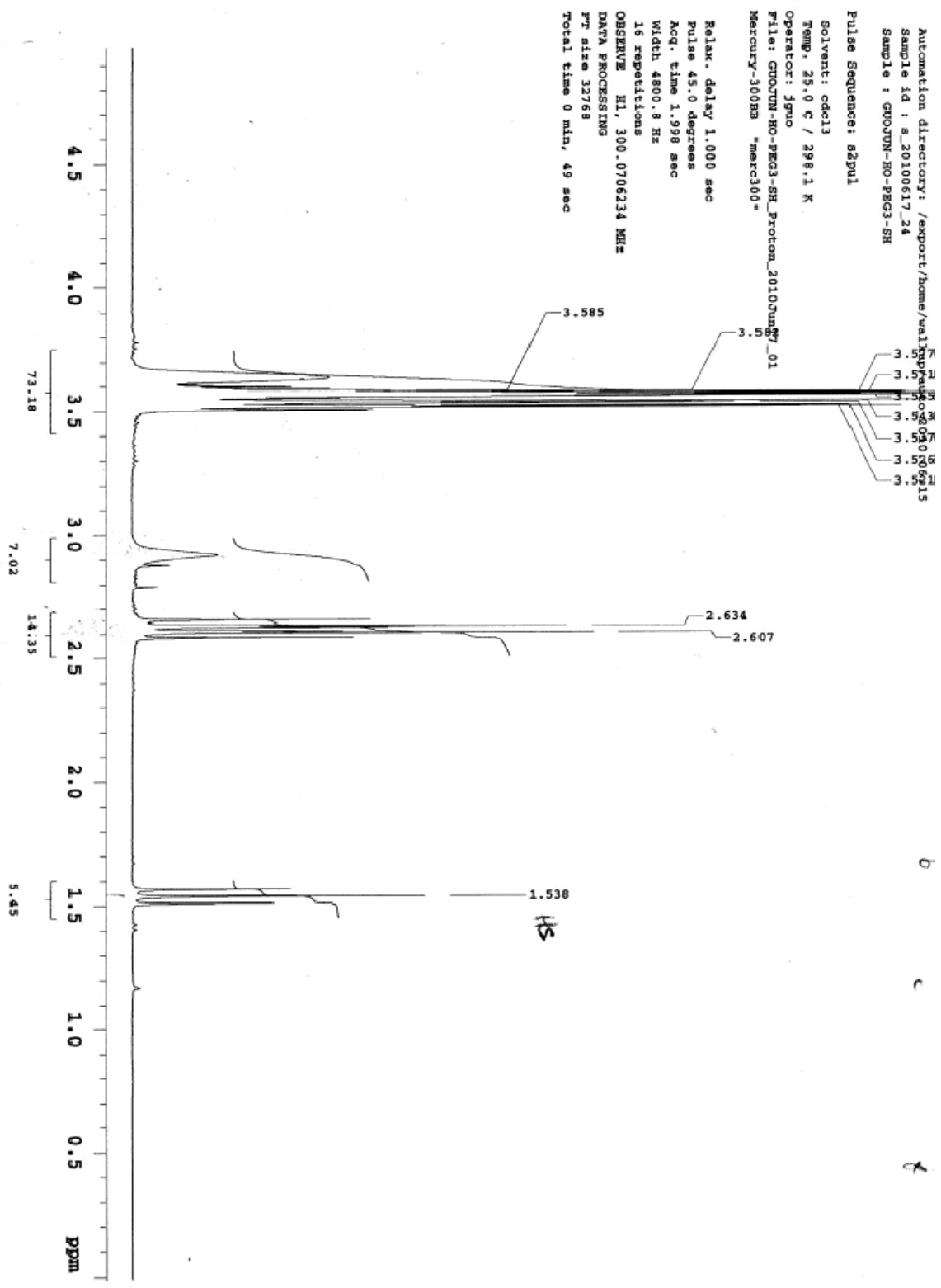

Figure A.5 ^{1}H-NMR spectrum of **2-(2-(2-mercaptoethoxy)ethoxy)ethanol** in Deuterochloroform ($CDCl_3$)

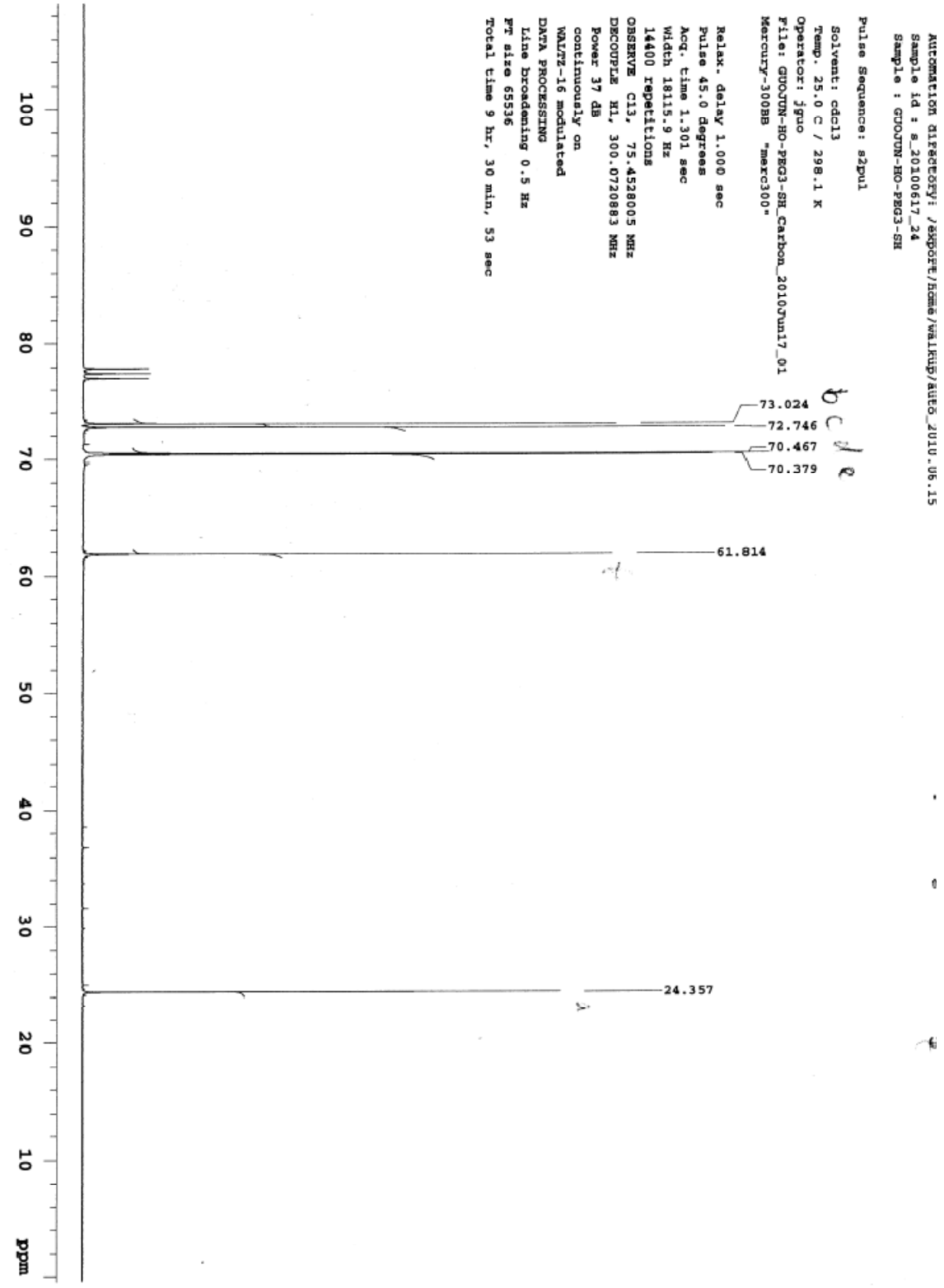

Figure A.6 ^{13}C-NMR spectrum of **2-(2-(2-mercaptoethoxy)ethoxy)ethanol** in Deuterochloroform ($CDCl_3$)

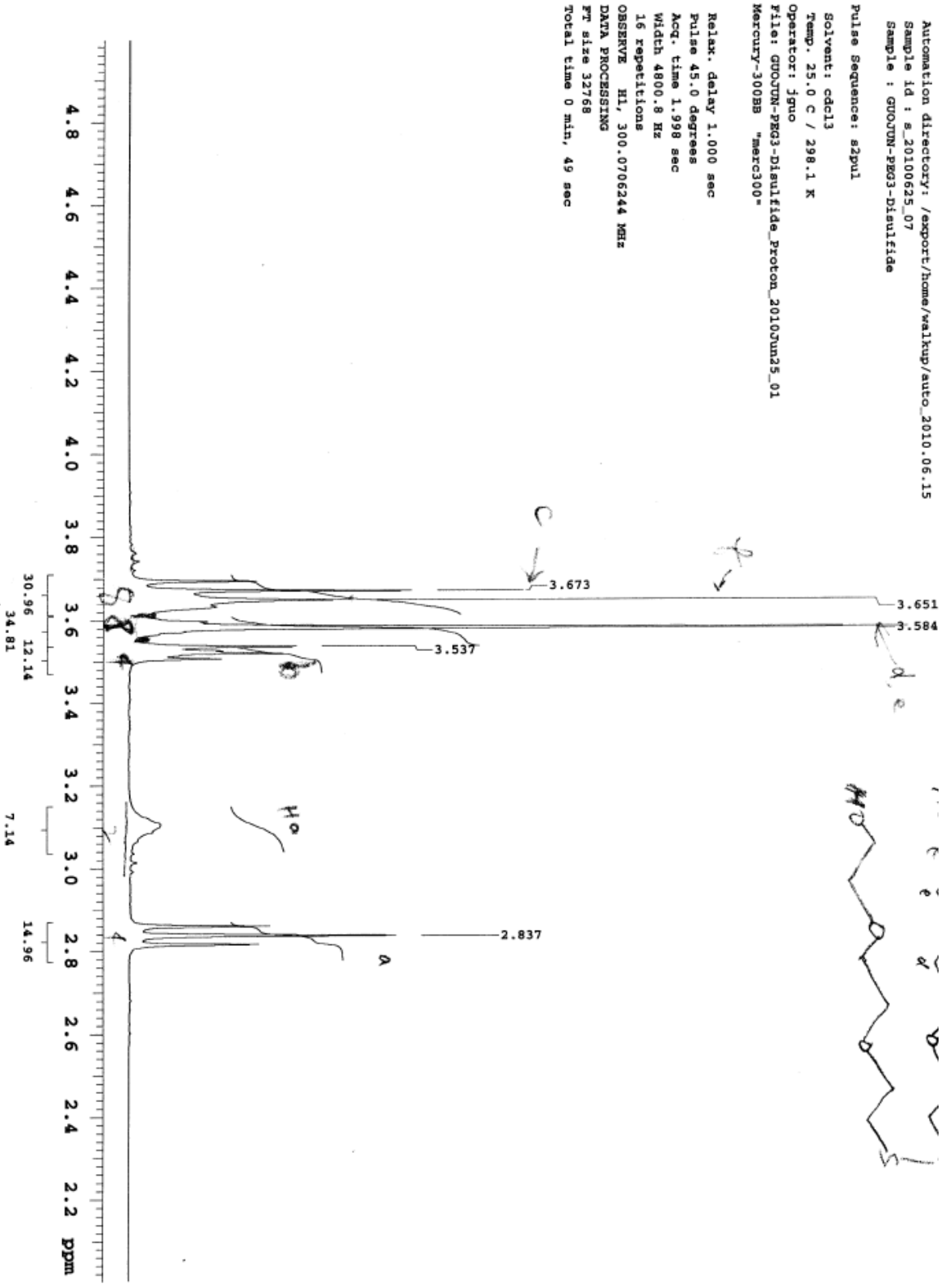

Figure A.7 ^{1}H-NMR spectrum of **Compound 3** in Deuterochloroform ($CDCl_3$)

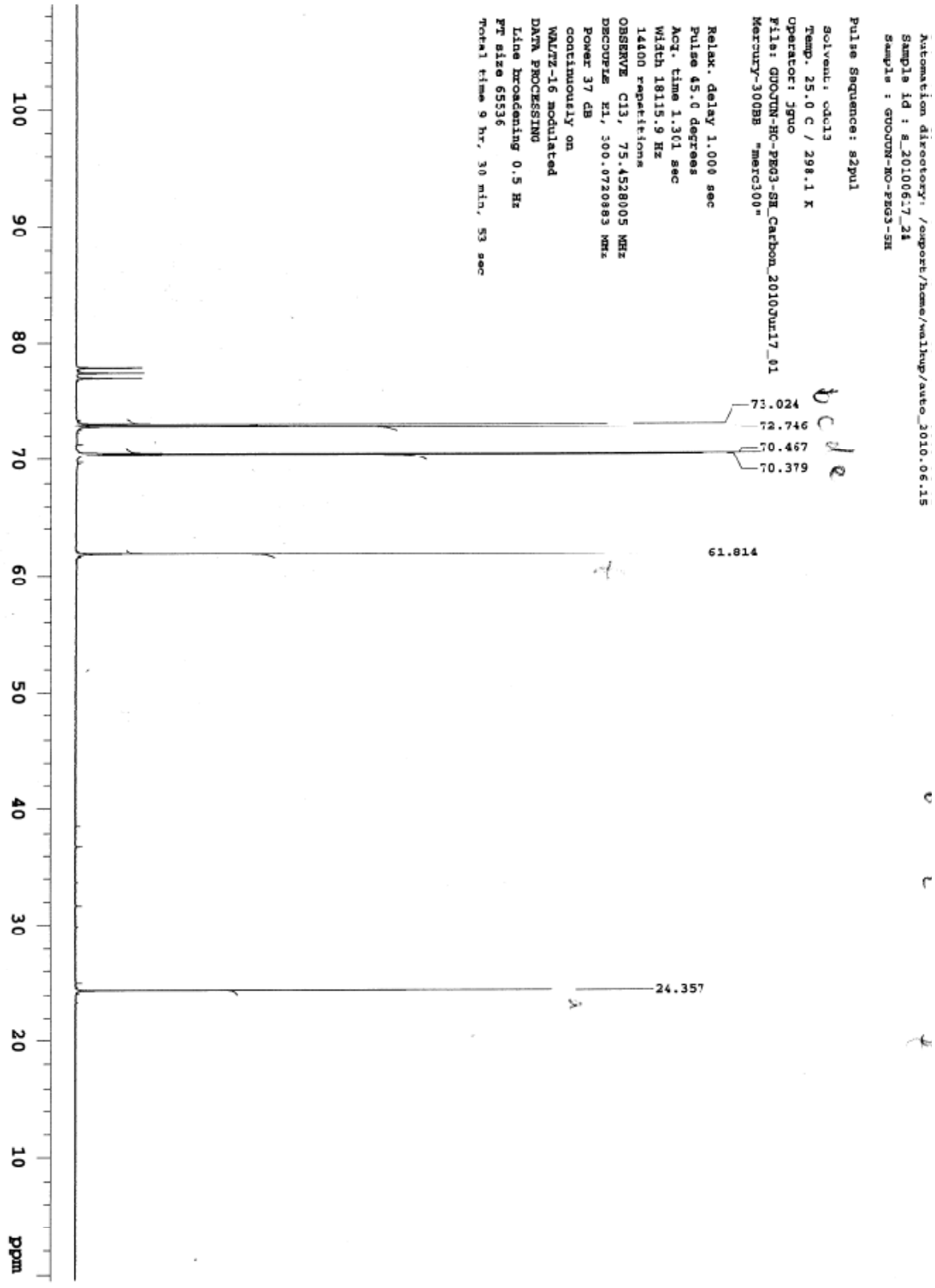

Figure A.8 ^{13}C-NMR spectrum of **Compound 3** in Deuterochloroform ($CDCl_3$)

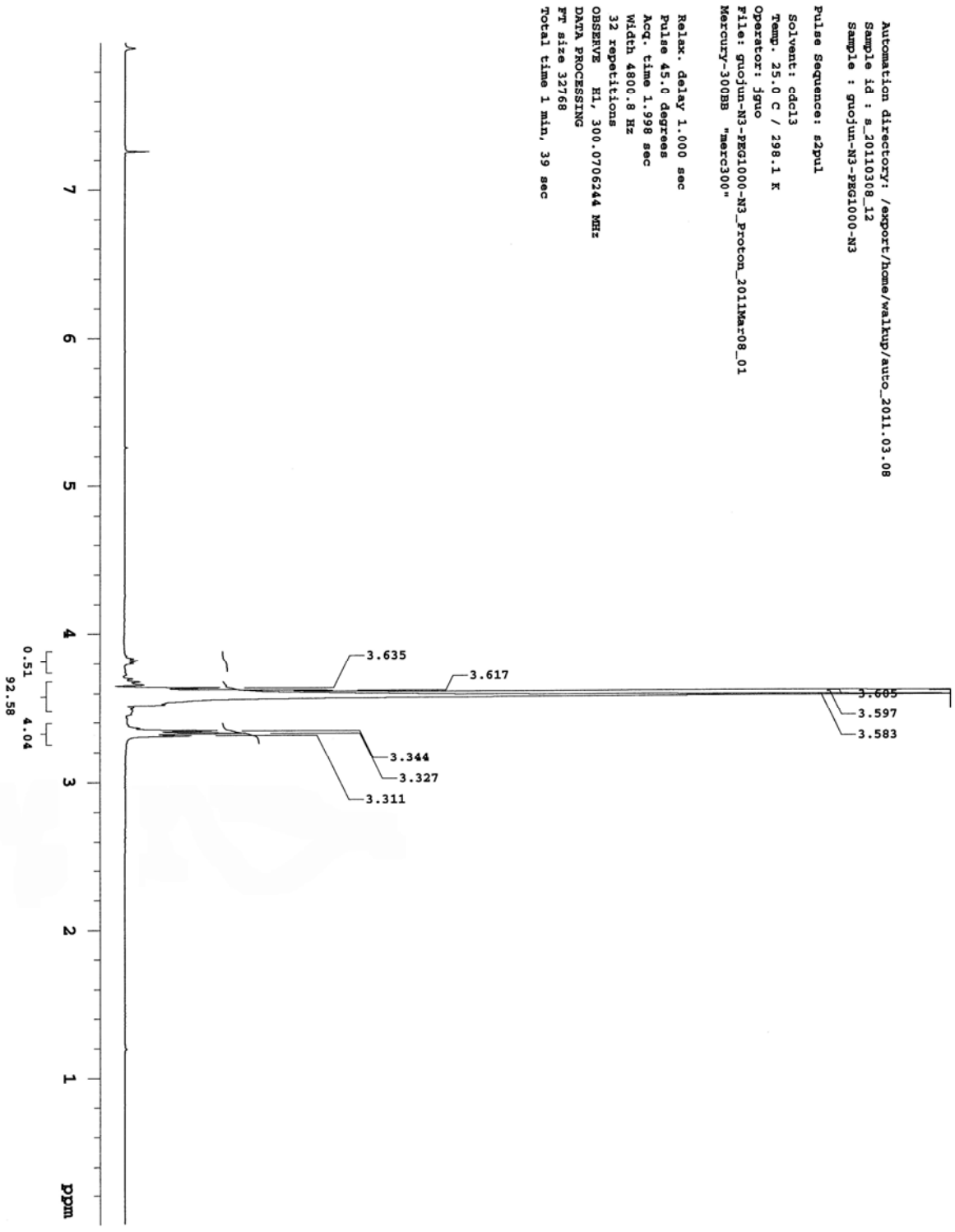

Figure A.9 ^{1}H-NMR spectrum of **Compound 9** in Deuterochloroform ($CDCl_3$)

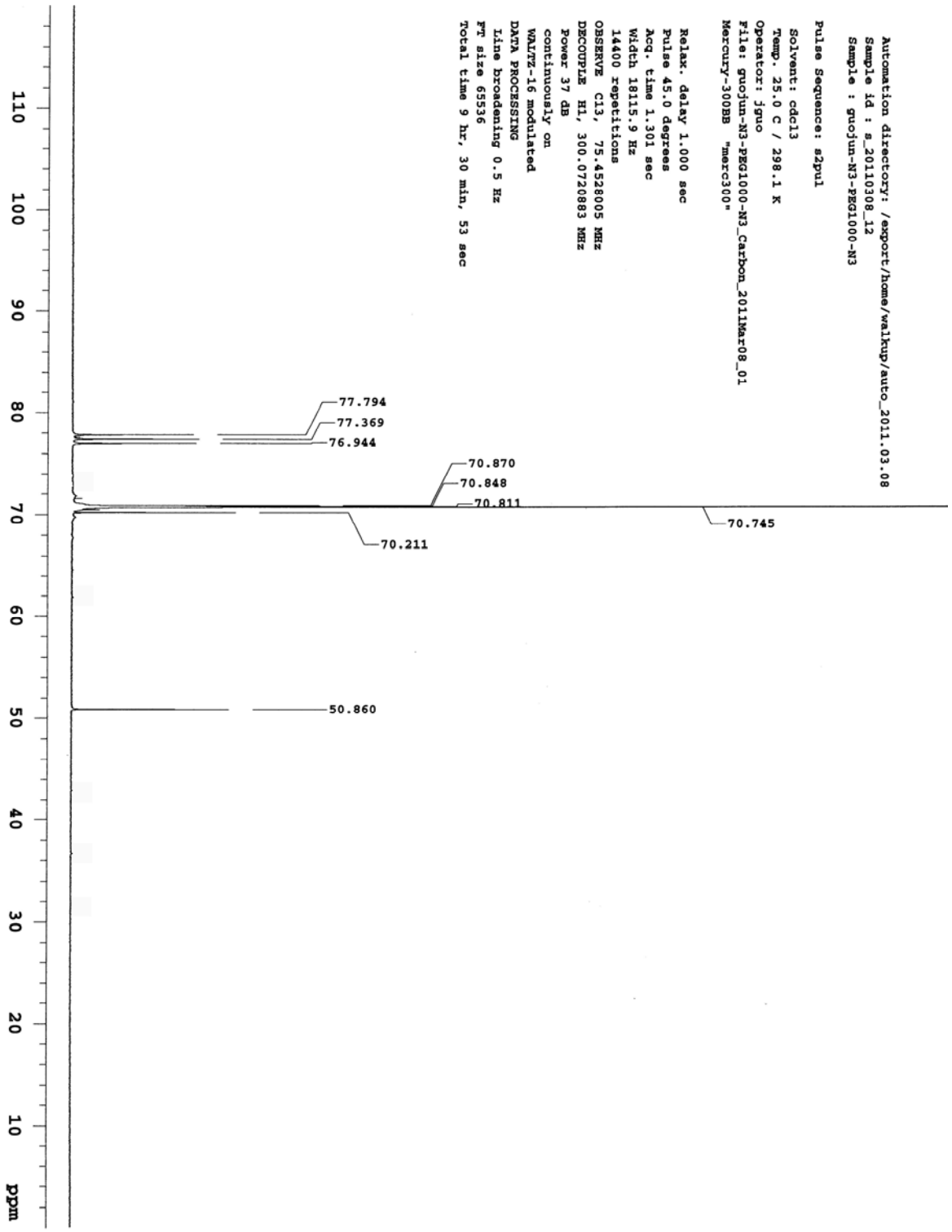

Figure A.10 ^{13}C-NMR spectrum of **Compound 9** in Deuterochloroform ($CDCl_3$)

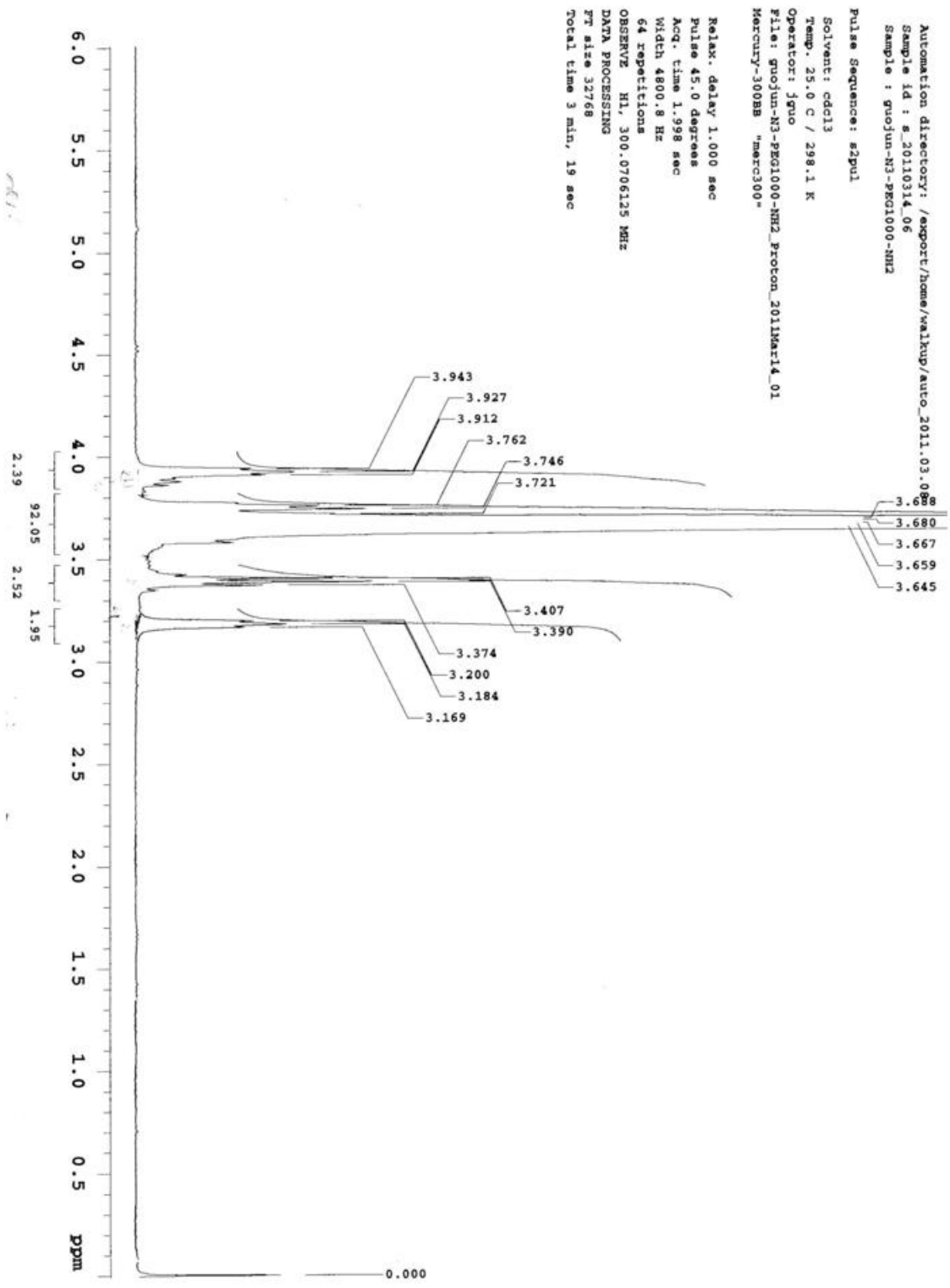

Figure A.11 ^{1}H-NMR spectrum of **Compound 10** in Deuterochloroform ($CDCl_3$)

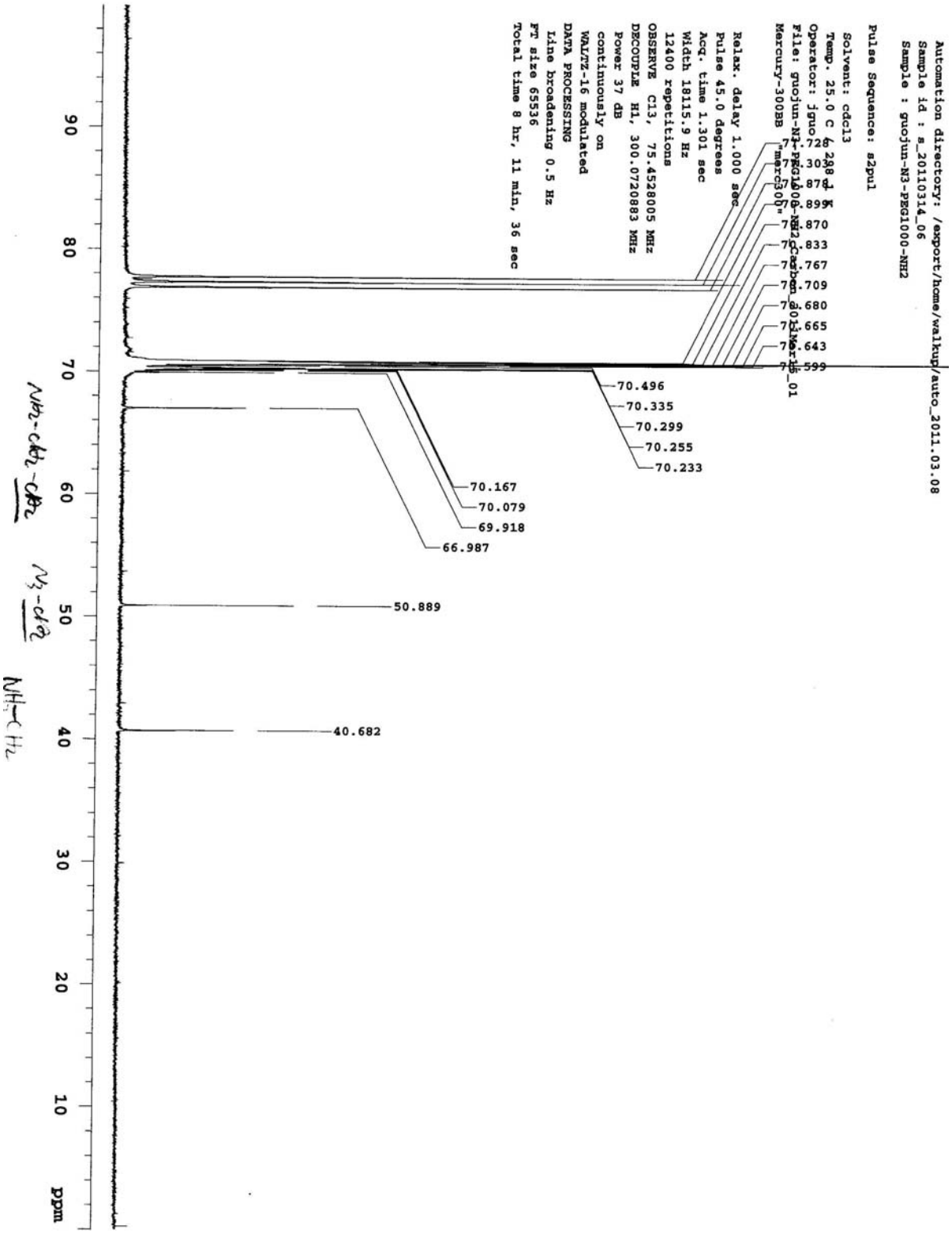

Figure A.12 ^{13}C-NMR spectrum of **Compound 10** in Deuterochloroform ($CDCl_3$)

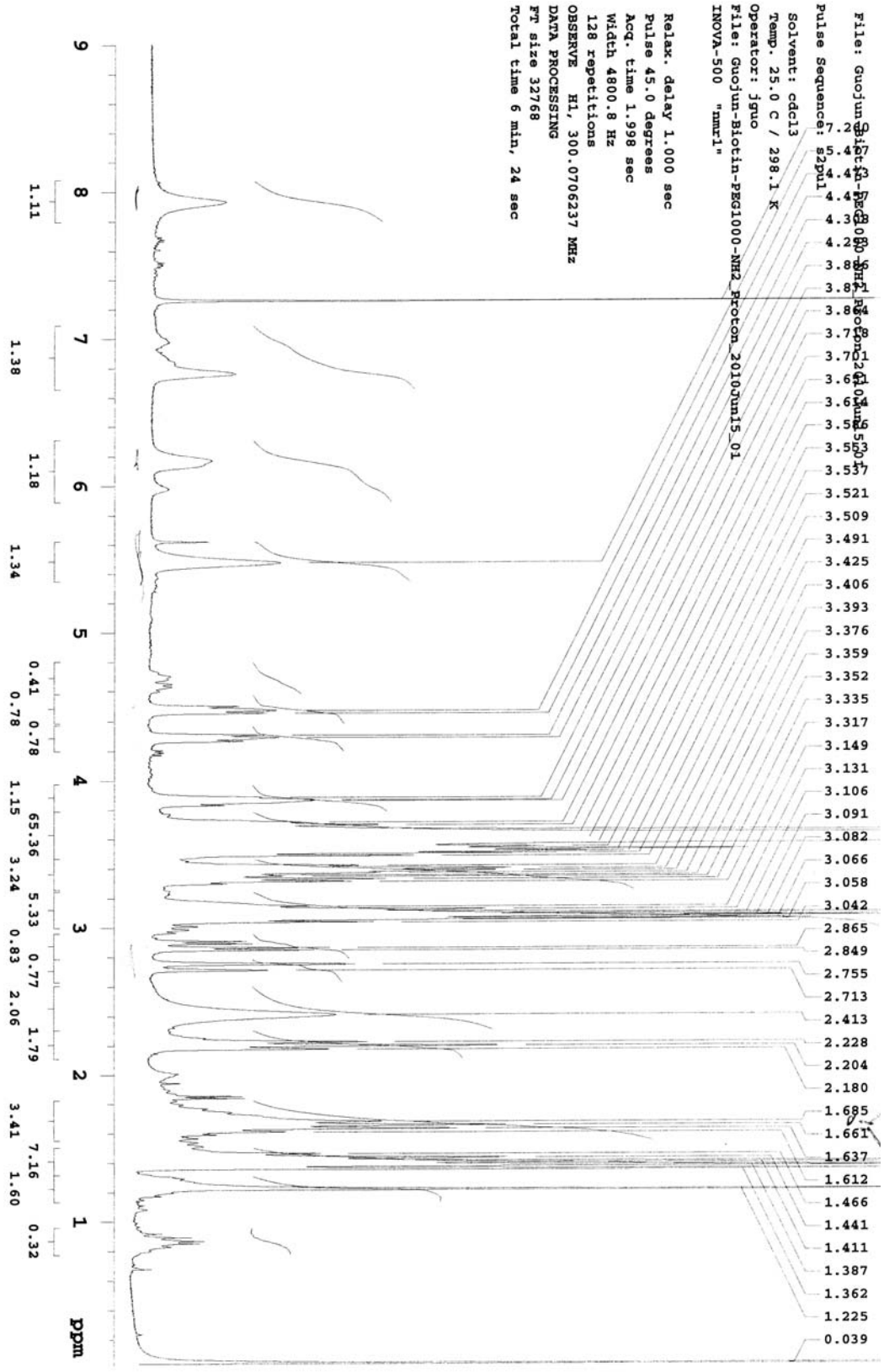

Figure A.13 ^{1}H-NMR spectrum of **Compound 12** in Deuterochloroform ($CDCl_3$)

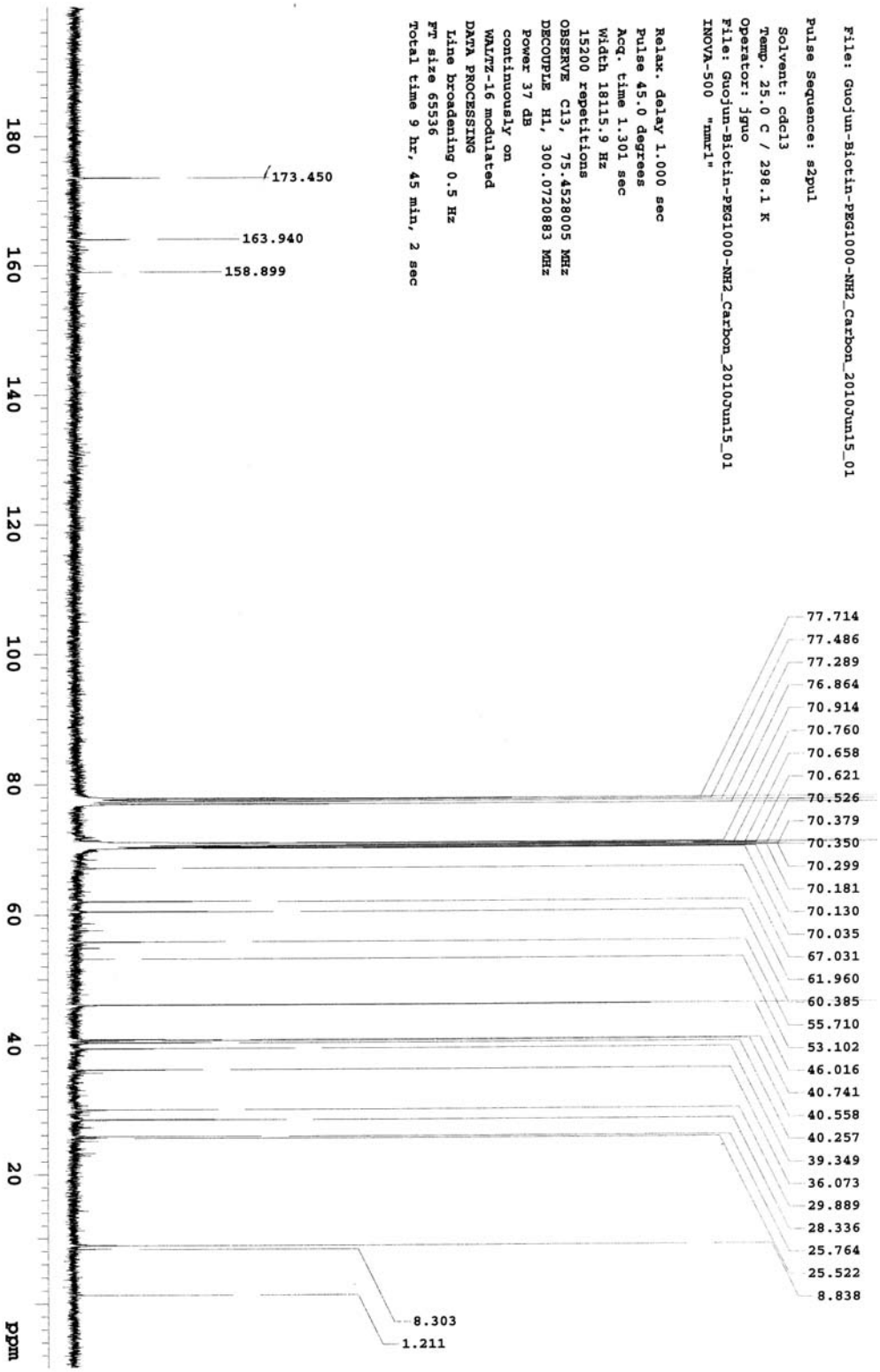

Figure A.14 ^{13}C-NMR spectrum of **Compound 12** in Deuterochloroform ($CDCl_3$)

APPENDIX B

SUPPLEMENTS TO CHAPTER 5

In Appendix B, there is some supplement information for Chapter 5.

B-1: Determination of shape and size of the organomicelle

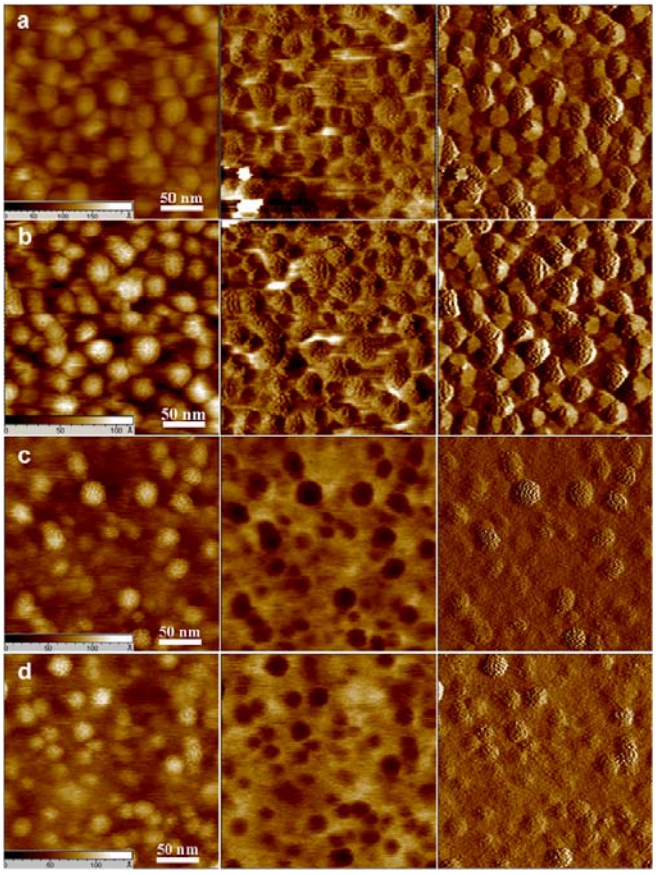

Figure B.1 The topographical (left column), phase (middle column) and amplitude (right column) images of a) micelles **B**, b) micelles **C**, c) micelles **D**, and d) micelles **E** using magnetic *AC* mode ***(***MAC mode***)*** AFM imaging. Nanometer features of the micelle surface are clearly resolved.

High Resolution Images: Ultrahigh resolution imaging obtained by TOPMAC mode AFM for micelles **B** (***Figure B.1*** a), Rd-loaded micelles **C** (***Figure B.1*** b), micelles **D** (***Figure B.1*** c) and micelles **E** (***Figure B.1*** d). The micelles are uniformly distributed throughout the underlying gold surface and have diameters ranging from 20~50 nm.

B-2: Estimation of functional group on AFM tip

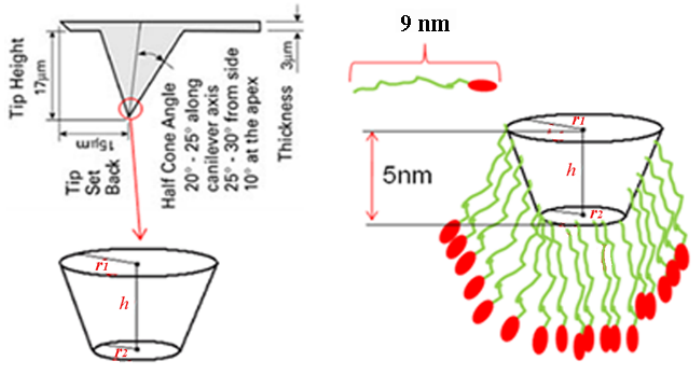

Figure B.2 The schematics used to estimate the available functional groups of dibenzylcyclooctyne for the chemical click reaction with the azide groups of macromolecules of a micelle.

To estimate the number of functional groups available on the AFM tip for reaction with azido groups on the micellar surface, we first determined the grafting density of compounds **7** (cross-linker), and multiply this data with the available area of the AFM tip (estimated from geometry data provided by the vendor).

Determination of the cross-linker (Compounds 7) grafting density using measured thickness data: First, a silicon wafer was cut into 5 mm^2 small pieces which were cleaned by

piranha solution (H_2SO_4/H_2O_2, 3:1, v/v) for 30 min. Next, the silicon wafer pieces were rinsed thoroughly with deionized water, dried under a flow of argon, following by activation and cleaning by UV for 30 min. Finally, the silicon wafer pieces were modified with dibenzylcyclooctynol following the procedure described for tip modification.

After the chemical functionalization with **7** (22 mer and 4 mer), the thickness of the cross-linker layer was measured by ellipsometer module of OPTREL multiskop. The average measured thickness *h* is 5.5±0.6 nm or 2.3±0.1 nm respectively for compound **7** (22 mer and 4 mer).

The cross-linker grafting density can be calculated by using $\sigma = (h\rho N_A)/M_n$. Where σ is polymer grafting density, *h* is the polymer thickness, ρ is bulk density of the polymer (1.1~1.2 g/cm^{-3}), N_A is Avogadro's number and M_n is the molecule weight (M_n=1307 Da for compound **7** (22 mer) and 559 for compound **7** (4 mer)). The cross-linker grafting density σ was determined to be 2.78 molecules/nm^2 or 2.71 molecules/nm^2.

Estimation of the available area of the AFM tip: The geometry parameters of AFM tip (CS-10 silicon AFM probe, Nanoscience Instruments) are shown in Figure SI-5. The tip radius r_2 is smaller than 10 nm and thus for the calculation we have employed two extremes in which the radius is 2 or 10 nm. The area available for useful functionalization is: $S = \pi(r_1 + r_2)\sqrt{(r_1 - r_2)^2 + h^2} + \pi r_2^2$, where $\pi(r_1 + r_2)\sqrt{(r_1 - r_2)^2 + h^2}$ is the area of the body side S_{body} (cone of the tip) and πr_2^2 is the area of the top of the tip S_{r2}.

Estimation of available functional groups on AFM tip: Based on the available area of a functionalized AFM tip (*S*) and the cross-linker grafting density (σ), the number of available functional groups on the tip is the product of σS. The resulting calculations are summarized in Table SI-5. For a tip that has a radius of 2 and 10 nm, approximately 32 and 848 functional

groups, respectively will be present at the top of a tip. Due to the spacer of compounds **7** (22 mer or 4 mer), part of the body surface (cone of the tip) is also available for reaction. The estimated spacer length of the compounds is estimated to be 9 or 2 nm, respectively. Therefore, the total number of available functional groups for reaction ranges from 200 to 3,000 depending on tip size and length of the spacer.

Table B.1 Estimation of available functional groups on AFM tips with different sizes.

r_1 (nm)	r_2 (nm)	h (nm)	S_{body} (nm^2)[a]	S_{r2} (nm^2)[b]	S (nm^2)[c]	number of molecules[d]
5.64	2	5	148	12	161	435 (S)/32 (S_{r2})
13.64	10	5	459	314	774	2090 (S)/848 (S_{r2})
3.46	2	2	42	12	54	146 (S)/32 (S_{r2})
11.46	10	2	167	314	481	1299 (S)/848 (S_{r2})

a. S_{body} is the area of the body side;

b. S_{r2} is the area of the top of the tip;

c. S is equal to S_{body} plus S_{r2}, e.g. the sum of the area of the body side and the area of the top of the tip.

d. Amount of molecules is the product of σ and S for the place of the body side and the tip top (left number), or the product of σ and S_{r2} for the place of the tip top (right number).

B-3: Histograms for micelle-A, micelle-B, micelle-C under three force loading rate

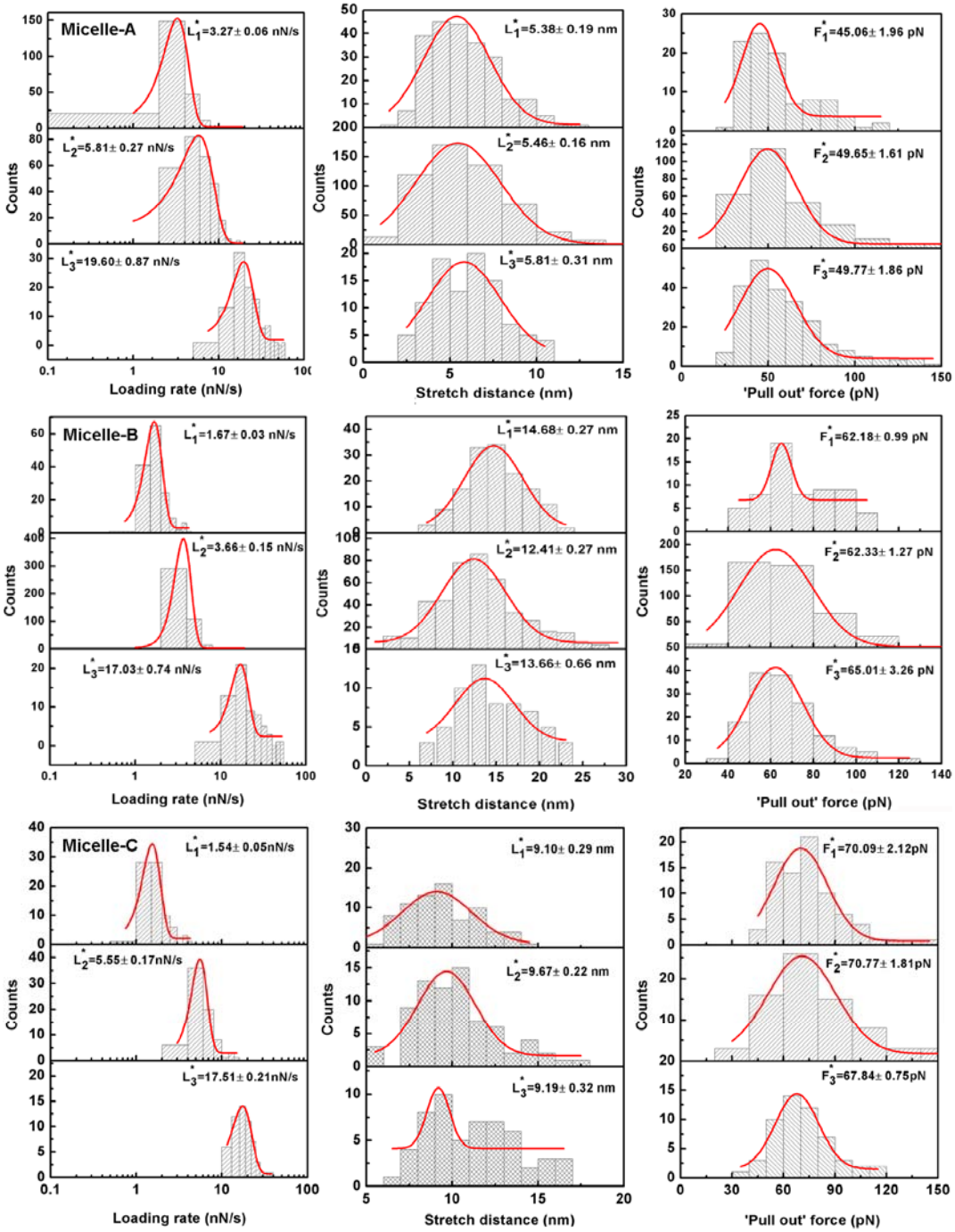

Figure B.3 Force loading rate, stretch distance, and 'Pull out' force histograms for micelle-A, micelle-B and micelle-C.

The average stretch distance and 'pull out' force for micelle-**A**, micelle-**B**, and micelle-**C** over the measured force loading rate range were calculated by averaging three most probable values under three different force loading rate, as shown in ***Figure B.3***. For example: The averaged stretch distance of micelle A was calculated by (5.38+5.46+5.81)/3=5.55 nm and its corresponding error was (0.31+0.18+0.19)/3=0.23 nm. The averaged 'pull out' force of micelle A was calculated by (45.06+49.65+49.77)/3=48.16 and its corresponding error was (1.96+1.61+1.86)/3=1.81.

B-4: Dynamic light scattering (DLS) measurements

Dynamic light scattering (DLS) measurement were performed on a Zeta Potential and Particle Size Analyzer (ZetaPALS, Brookhaven Instruments Corp., US). Dust-free vials were used for the aqueous solutions, and measurements were made at 25 ^{o}C at an angle 90 ^{o}C. Critical micelle concentrations (CMC) were determined by diluting the micelle solutions (two fold dilutions) until no particles were observed by DLS measurements, listed out in ***Table B.2***.

Table B.2 The size, polydispersity index and CMC of micelles.

Micelle	Mean diameter (nm)	Polydispersity	(CMC, mg/L)
A	42.1	0.129	1.2
B	57.3	0.197	0.2
C	47.9	0.281	0.2
D	46.1	0.113	1.2
E	41.4	0.335	1.2
F	40.2	0.311	1.2